UNIKASSEL VERSITÄT
MATHEMATICS AND NATURAL SCIENCES

Master thesis

Infrared spectroscopy of linear dialuminum monoxide, Al_2O

Submitted by: Eileen Döring

January 2020

1. Referee: Prof. Dr. Thomas Giesen

2. Referee: Prof. Dr. Arno Ehresmann

University of Kassel
Faculty 10 of Mathematics and Sciences
Institute of Physics

Abstract

In this master thesis the ro-vibrational infrared spectrum of the linear dialuminum monoxide (Al_2O) of $D_{\infty h}$ symmetry has been measured and analyzed. Al_2O was produced by laser ablation of an aluminum sample seeded in a N_2O/He carrier gas. The molecules were cooled down to rotational temperatures of 119 K via adiabatic expansion of the gas into a vacuum chamber where a supersonic jet was formed. A quantum cascade laser which covers a frequency range from $970\,cm^{-1}$ to $1074\,cm^{-1}$ was used, to measure the Al_2O spectrum. Six different vibrational bands, containing 874 rotational lines, were assigned to the Al_2O molecule. In addition the vibrational band $(12^01) \leftarrow (12^00)$ was tentatively assigned. For the first time alternating intensity fluctuations were seen in a spectrum, that are due to the spin-statistical weights of two identical aluminum atoms ($I = 5/2$) within a molecule. In total, molecular parameters for 13 vibrational levels were derived, including the l-type doubling constant for the vibrational energy levels (01^11) and (01^10) and the perturbation parameter for the vibrational energy levels (02^0v_3) and (02^2v_3) with $v_3 = 0, 1$.

Kurzzusammenfassung

In dieser Masterarbeit wurde das Rotations-Schwinungsspektrum von linearem Dialuminiummonoxid (Al_2O) mit $D_{\infty h}$ Symmetrie gemessen und analysiert. Al_2O wurde durch Laserablation einer Aluminiumprobe, die in der Umgebung eines N_2O/He Gasgemisches platziert wurde, hergestellt. Ein Überschalldüsenstrahl entstand durch adiabatische Expansion der Moleküle in einer Vakuumkammer. Die Moleküle wurden dabei auf Rotationstemperaturen von 119 K abgekühlt. Zur Messung des Al_2O-Spektrums wurde ein Quantenkaskadenlaser verwendet, der den Frequenzbereich von 970 cm^{-1} bis 1074 cm^{-1} abdeckt. Sechs verschiedene Schwingungsbänder, die 874 Rotationslinien enthalten, wurden dem Al_2O-Molekül zugeordnet. Zusätzlich wurde vorläufig die Schwingungsbande $(12^01) \leftarrow (12^00)$ zugeordnet. Zum ersten Mal konnten wechselnde Intensitätsfluktuationen in einem Spektrum beobachtet werden, die auf die spinstatistischen Gewichte zweier identischer Aluminiumatome ($I = 5/2$) innerhalb eines Moleküls zurückzuführen sind. Insgesamt wurden molekulare Parameter für 13 Vibrationsniveaus bestimmt. Darunter auch die l-Typ-Verdopplungskonstanten (l-type doubling constant) für die Vibrationsenergieniveaus (01^11) und (01^10) und die Störungsparameter der Störung zwischen den Vibrationsenergieniveaus (02^0v_3) und (02^2v_3) jeweils für $v_3 = 0, 1$.

Contents

List of Figures

List of Tables

1 Introduction

The process of cosmic dust formation has not yet been fully understood. The majority part of the interstellar medium, including dust, is ejected by late-type stars and supergiant stars at the end of their life time. Depending on whether late-type stars contain more oxygen or more carbon, they belong either to the class of oxygen rich M-type stars or to the C-type stars (carbon rich). Dust grain formation in C-type stars is already better understood, while the process in M-type stars is not as clear[1,2].

It is believed that the transition from atomic to molecular content happens via the formation of diatomic molecules. The most stable diatomic molecule, which can form at very high temperatures due to its strong binding energy, is CO. This means that in M-type stars in which oxygen is present in abundance, most of the carbon is locked in CO and thus cannot be involved in the dust formation. For the same reason in C-type stars oxygen is less involved in the dust formation. Thus the spectral class of a star determines the type of chemistry in its vicinity e.g. in stellar outflows.[2]

The work of Sharp and Hübner[3], as well as Lattimer *et al.*[4], showed that the first condensates present in a cooling atomic gas with standard cosmic element abundances are aluminum, titanium and zirconium containing species. However, in this case only aluminum and titanium bearing molecules are present in sufficiently large amounts to act as seed nuclei for dust formation. In 2017, Kamiński[5] concluded that the amounts of gaseous titanium oxides are too large to provide initial seeds for dust formation, based on his observations at Mira. Similar results were obtained by Decin *et al.*[6], from their observations of RDor and IKTau. Kamiński *et al.*[7] were also able to show for VY Canis Majoris that the titanium oxides cannot perform a main role in dust nucleation. What remains are aluminum bearing molecules that could assume an important role in dust nucleation.

Specifically aluminum is one of the twelve most common elements in space and the most refractive of the 20 leading elements in the periodic table.[8,9] Refractory elements

form molecules at temperatures well above one thousand Kelvin, thus aluminum is a good candidate to be involved in the first molecule formations. Through equilibrium calculations for oxygen-rich element mixtures[3,10], it is known that aluminum and aluminum-calcium compounds such as corundum (Al_2O_3), melilite, spinel, diopside and anorthite can be formed in thermodynamic equilibrium at temperatures around 1000 K. Not surprising, these temperatures occur in the condensation zones of circumstellar shells. The most stable of the aluminum compounds is corundum as it has a high bonding energy. Interestingly, it is a relatively common mineral on earth. According to Gail and Sedlmayer[2], a possible formation of corundum in the gas phase could result from the following reaction:

$$Al_2O + 2H_2O \longrightarrow Al_2O_{3\,(s)} + 2H_2$$

Due to the low pressure in circumstellar dust shells, corundum becomes the most stable aluminum compound at temperatures well below 1400 K. Beside corundum, the next abundant aluminum compounds in the gas phase are dialuminum monoxide (Al_2O), aluminum oxide (AlO) and aluminum hydroxide (AlOH)[2,11].

In 2009, Tenenbaum and Ziurys[11] detected AlO in the circumstellar shell of the red super giant VY Canis Majoris for the first time, using the Arizona Radio Observatory (ARO). They used a model of Tsuji[12] with cosmic abundances of Lodders[9] to calculate LTE (local thermodynamic equilibrium) abundances of aluminum bearing molecules, see Figure 1.1.

Both in C-type stars and in O-rich stars, the model calculation predicts a high excess of Al_2O, compared to other aluminum compounds, at distances from the stars with a temperature range of 1000-1500 K. This temperature range is within the dust forming region.

Still, Al_2O has not yet been detected in a stellar environment. Tenenbaum and Ziurys[11] were not able to look for this molecule, as it has no permanent dipole moment and thus cannot be observed with radio telescopes. With optical telescopes it will be difficult to detect, because Al_2O is formed close to the star and is most likely shielded by dust from the outside, when looking at visual wavelengths.

However, infrared telescopes provide a possible solution for these problems because IR radiation can pass through dust. Al_2O could be detected by a new generation of

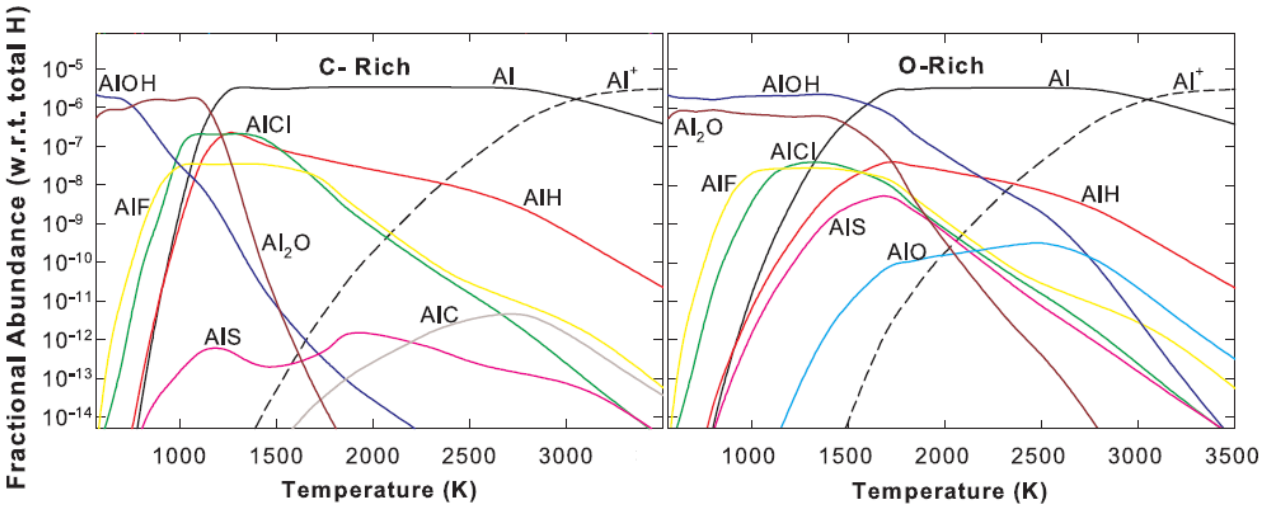

Figure 1.1: Abundances of aluminum-containing molecules from LTE model calculations, in relation to total hydrogen (H_2+H+H^+) plotted as a function of temperature. Left: Data were calculated for a carbon-rich gas with C/O $\sim$ 1.5. Right: Data represent oxygen-rich situation with C/O $\sim$ 0.5.[11]

high-resolution infrared instruments like EXES[13] on board the SOFIA[1] or TEXES[14] at the IRTF[2] or the Gemini North telescope. Infrared radiation has the ability to penetrate deeper into the dust zone than optical radiation does and in addition, linear Al_2O is an infrared active molecule.

Already in 1963 Büchler *et al.*[15], suggested in their electron deflection experiments that Al_2O is a linear molecule with a $D_{\infty h}$ symmetry. However, in early infrared studies using matrix isolation experiments by Linevsky *et al.*[16], a binding angle of about 145(5)° was found for Al_2O suggesting C_{2v} symmetry, which was not confirmed or refined at that time without measuring further data. In 1971, the results of Makowiecki *et al.*[17] even led to the assumption that there was a metal-metal bonding in Al_2O, suggesting a ring-type structure. Douglas *et al.*[18] was able to deduce from their results of a matrix measurement that Al_2O must be a molecule with a $D_{\infty h}$ symmetry considering the former work of Marino and White[19] in 1982. In 1988, the first *ab initio* calculations were performed by Masip *et al.*[20] and resulted in the first determination of the structure and vibrational frequencies of the Al_2O molecule. They concluded for the Al_2O molecule a linear structure.

Further *ab initio* calculations of the molecular structure follow in 1992 and came to the same conclusion, Al_2O must be a linear molecule[21,22]. Cai *et al.*[23] were able

[1] Stratospheric Observatory For Infrared Astronomy
[2] InfraRed Telescope Facility

to detect Al_2O by laser induced fluorescence measurements and confirmed a linear structure for Al_2O with a rotational constant of $0.1087\,cm^{-1}$. The antisymmetric stretching vibration ν_3 was determined at a frequency of $992\,cm^{-1}$, in the gas phase measurements by Cai *et al.*[23] 1991 and in the matrix measurements by Andrews *et al.*[24] 1992. Cai *et al.*[23] also experimentally determined the bending frequency ν_2 to a frequency of $99\,cm^{-1}$, as well as the symmetrical stretching oscillation ν_1 at a frequency of $525\,cm^{-1}$.

Almost 10 years later, Deutsch *et al.*[25] calculated the absolute electron-impact ionization cross sections for metal oxide molecules. In 2004, Koput and Gertych[26] published a prediction of the potential energy surface and vibrational-rotational energy levels of Al_2O with a rotational constant of $0.1082\,cm^{-1}$. One year later, calculations were published for the singlet electronic ground state of Al_2O by Turney *et al.*[27].

In this work, for the first time a ro-vibrationally resolved infrared spectrum of Al_2O has been measured. The Al_2O molecules were generated by laser ablation on the surface of an aluminum rod seeded in a N_2O/He carrier gas. The atoms generated by the plasma reacted in a short reaction channel at high temperatures, before they were expelled into a vacuum chamber. Here, a supersonic jet was formed and the adiabatic expansion caused the molecules to be cooled to a rotational temperature of less than 120 K. The cooled molecules were measured with a tunable quantum cascade laser (QCL) resulting in a molecular spectrum.

This work begins with an introduction of the theoretical basis of molecular spectroscopy. The next chapter deals with the experimental setup and the used instruments, before explaining the concept of the molecular production using laser ablation. After this, the measuring method and the data reduction are explained. In the following chapter, the obtained spectrum is analyzed and discussed. Finally, a summary of the results obtained is given.

2 Fundamentals of Spectroscopy

Molecules always show a vibrational motion of their own. Even if no excitation energy is added, a certain zero point energy (ZPE) exists. The motion energy E of a molecule can be determined by solving the Schrödinger equation:

$$\hat{H}\Psi = E\Psi \tag{2.1}$$

whereby $\hat{H}$ represents the Hamilton operator and Ψ reflects the wave function. By applying the Born-Oppenheimer approximation, where the movement of the heavy atomic nucleus can be neglected compared to the movement of the light electrons, the energy E can be separated as follows:

$$E_{\text{total}} = E_{\text{el}} + E_{\text{vib}} + E_{\text{rot}} + E_{\text{spin}}. \tag{2.2}$$

The total energy of the molecule consists at least of the sum of the four energy components, i.e. the electronic (E_{el}), vibrational (E_{vib}) and rotational (E_{rot}) motion, as well as the nuclear spin state (E_{spin}).

Molecular energy levels are excitable through resonant transition energies ($h\nu_{E',E''}$), supplied by external radiation field i.e. an electromagnetic wave. $E'' + h\nu_{E',E''} = E'$, with E'' lower level, E' upper level and $\nu_{E',E''}$ settled in the frequency range of 300 MHz - 300 GHz (microwave radiation) excite rotational transitions. Vibrational transitions are excited with frequencies of 300 GHz - 430 THz (infrared radiation) and electronic transitions are induced with frequencies of 400 nm - 780 nm (optical radiation).

In the following chapter, mainly rotational and vibrational transitions will be discussed, so called ro-vibrational transitions. For a more detailed description of molecular spectroscopy and the quantum mechanical background, the following literature is recommended: Bernath[28]; Haken, Wolf[29]; Demtröder[30,31] and Gordy, Cook[32].

2.1 Rotational Spectroscopy

This work focuses on the molecule Al_2O, a linear molecule. Thus, only the rotation around an axis perpendicular to the molecular axis and passing through the center of mass of the molecule is possible.

In a first approximation, the rotational energy E_{rot} for a rigid linear molecule depends on its moment of inertia I. The square of the angular momentum operator $\hat{J}^2$ is identified from scaling the spherical harmonic part of the Schrödinger equation:

$$\frac{\hat{J}^2}{2I}\Psi = \frac{\hbar^2}{2I}J(J+1)\Psi \tag{2.3}$$

with the rotational quantum number J. By introducing the rotational constant B:

$$B = \frac{\hbar^2}{2I}\,[\text{joules}] = \frac{h^2}{8\pi^2 I}\,[\text{joules}] = \frac{h}{8\pi^2 I}\,[\text{Hz}] \tag{2.4}$$

with

$$I = \sum m_i r_i^2 \tag{2.5}$$

and considering the equation 2.3 follows for the rotational energy:

$$E_{\text{rot}}(J) = \frac{J(J+1)\hbar^2}{2I} = BJ(J+1). \tag{2.6}$$

Pure rotational transitions only take place if a molecule has a permanent dipole moment. In this case, only certain transitions are allowed and other transitions are forbidden, being determined by specific selection rules. In general the lower state quantum number is marked with a double prime (J'') and the upper state quantum number with a single prime (J'). An arrow between them indicates whether it is absorption ($J' \leftarrow J''$) or emission ($J' \rightarrow J''$) of a photon. The rotational transition frequencies are then be determined by:

$$\begin{aligned} h\nu_{J+1\leftarrow J} &= E_{\text{rot}}(J') - E_{\text{rot}}(J'') \\ &= B(J+1)(J+2) - BJ(J+1) \\ &= 2B(J+1). \end{aligned} \tag{2.7}$$

Evaluating Equation 2.7, the first possible transition ($J = 0$) occurs at a frequency of

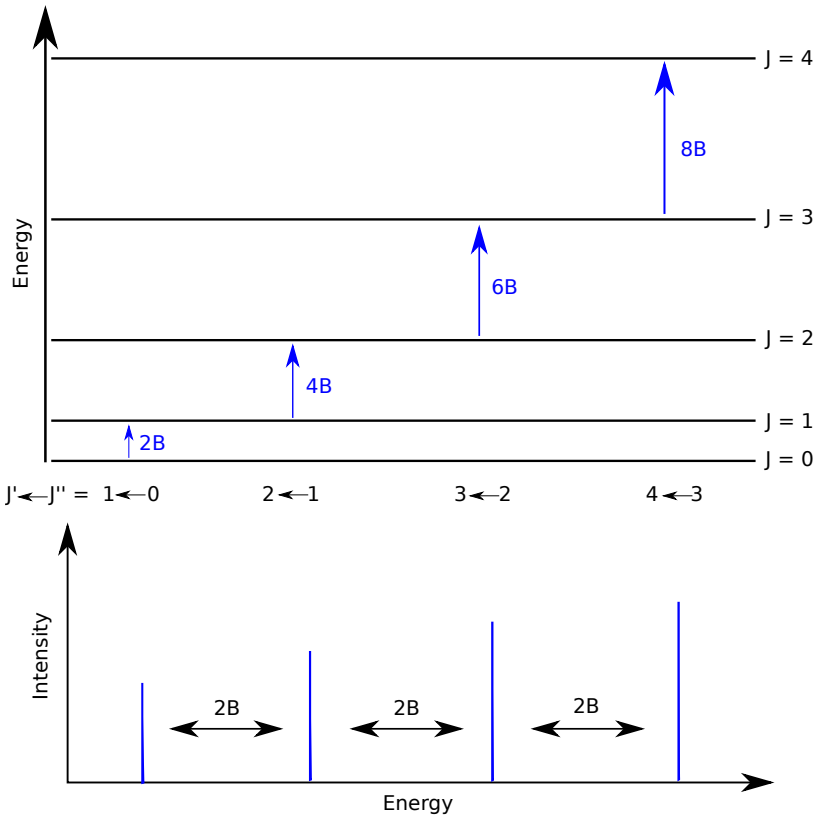

Figure 2.1: Schematic sketch of the rigid molecular energies ladder (upper figure) and the resonant transition frequencies at distance of $2B$ (lower figure) for four rotational transitions.

$2B$, while each further transition occurs by a multiple of $2B$. Regarding the rotational spectrum this leads to transition peaks with equidistant frequency separation of $2B$. These two properties of the rotational spectrum are illustrated in Figure 2.1.

Since a real molecule is not rigid centrifugal distortion must be taken into account. Due to centrifugal distortion, the moment of inertia increases and the rotational energy decreases with increasing angular momentum. As a consequence, the absorption lines in the spectrum no longer appear with equidistant frequencies.

In order to take these effects into account when calculating a spectrum, correction terms needed to be introduced. The following equation is used to determine the rotational energy:

$$E_{\mathrm{rot}}(J) = BJ(J+1) - D[J(J+1)]^2 + ... \tag{2.8}$$

where the centrifugal distortion constant D is given by $D = 4B^3 \left(\frac{\varsigma_{21}^2}{\omega_3^2} + \frac{\varsigma_{23}^2}{\omega_1^2} \right)$. Here ω_i represents the individual normal vibrations and ς_i represents the Coriolis coupling constants, which are a coupling between the vibrational modes and the rotation.

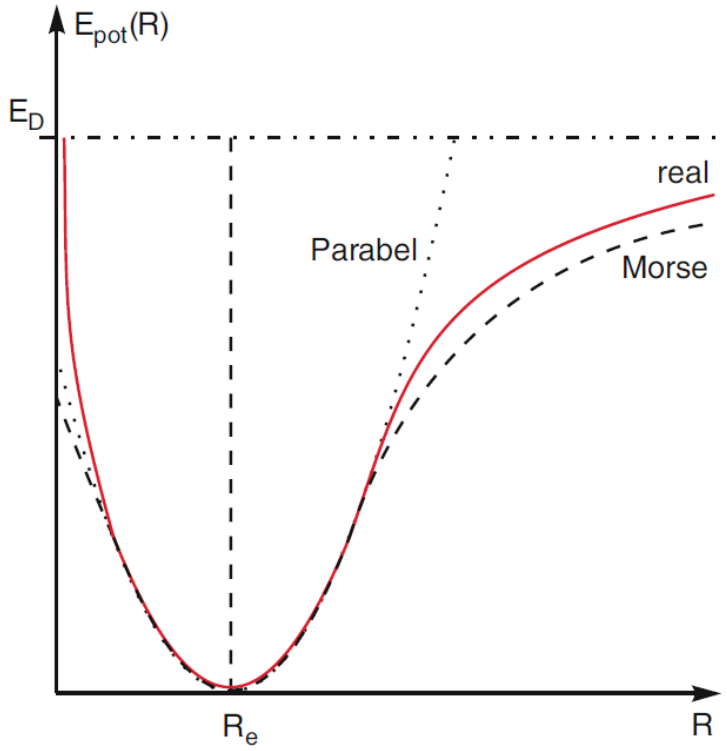

Figure 2.2: Comparison of the potential of a harmonic oscillator with the Morse potential and a real molecular potential of the ground state of the Na_2 molecule.[30]

2.2 Vibrational Spectroscopy of Linear Molecules

In addition to the molecular rotational motion, a molecule underlies also a vibrational motion. Separating the molecular rotational motion from the vibrational motion, the vibrational energy depends only on the potential energy E_{pot}. Near the potential minimum, the potential is described by a harmonic oscillator, where the bond length r of the molecule is the equilibrium bond length r_e ($r = r_e$) for low lying energy levels. However, since this does not apply to higher energy levels, the Morse potential (Equation 2.9, Figure 2.2) is used to describe the potential curve:

$$E_{\text{pot}}(r) = E_D \cdot [1 - e^{-a(r-r_e)}]^2, \tag{2.9}$$

with the dissociation energy $E_D = \frac{\omega_2^2}{4B_e}$ and the constant $a = \sqrt{\frac{k}{2E_D}}$ with $k = \frac{2E_D}{r_e}$. In the repulsive part of the potential for $r << r_e$, the approximation by Morse potential is no longer ideal. The Morse potential, as an approximation of the real potential, is a reasonable solution, since it allows an exact solution of the Schrödinger equation. Thus, the energy levels of the vibration of diatomic molecules can be calculated as

follows:

$$E_{\text{vib}}(v) = \hbar\omega\left(v + \frac{1}{2}\right) - \frac{\hbar^2\omega^2}{4E_D}\left(v + \frac{1}{2}\right)^2. \tag{2.10}$$

This means that the energy levels do not occur at equidistant energies. As the vibrational quantum number v increases, the distances between the energy levels $E_{\text{vib}}(v)$ decrease.

A molecule has $3N$ degrees of freedom, where N stands for the number of atoms in the molecule. Three of them are translations in each spatial direction and another three are identified by the rotation around the three main axes of inertia. For a linear molecule, the moment of inertia around the molecular axis is very small, so this rotation can be neglected. Thus, the number of vibrational degrees of freedom N_{vib}, also called normal modes, are given by:

$$\begin{aligned} N_{\text{vib}} &= 3N - 6 \quad \text{non-linear molecules} \\ N_{\text{vib}} &= 3N - 5 \quad \text{linear molecules,} \end{aligned} \tag{2.11}$$

A triatomic molecule, like Al_2O has four independent normal modes. These four normal modes includes a symmetric vibration (ν_1), the double degenerated bending vibration (ν_2^l) and the antisymmetric stretching vibration (ν_3).

The double degenerated bending vibration leads to an angular momentum of the nuclear motion. This total vibrational angular momentum is by its projection the upper index l (ν_2^l). The vibrational states of linear polyatomic molecules are labeled as in the case of diatomic molecules. This means that $\mid l \mid$ replaces the diatomic angular momentum Λ, resulting in Σ for $l = 0$, Π for $l = 1$, Δ for $l = 2$, and so on.

As seen before the potential is not harmonic (see Figure 2.2), thus, for triatomic molecules Equation 2.10 needs to be extended:

$$\frac{E_{\text{vib}}(v_1, v_2, ..., v_{3N-5}, l_i)}{\hbar} = \sum_i \omega_i\left(v_i + \frac{d_i}{2}\right) + \sum_{i \leq s} \chi_{is}\left(v_i + \frac{d_i}{2}\right)\left(v_s + \frac{d_s}{2}\right) + gl^2, \tag{2.12}$$

where g is the energy shift, due to the vibrational angular momentum and χ_{is} describes the anharmonicity of the potential.

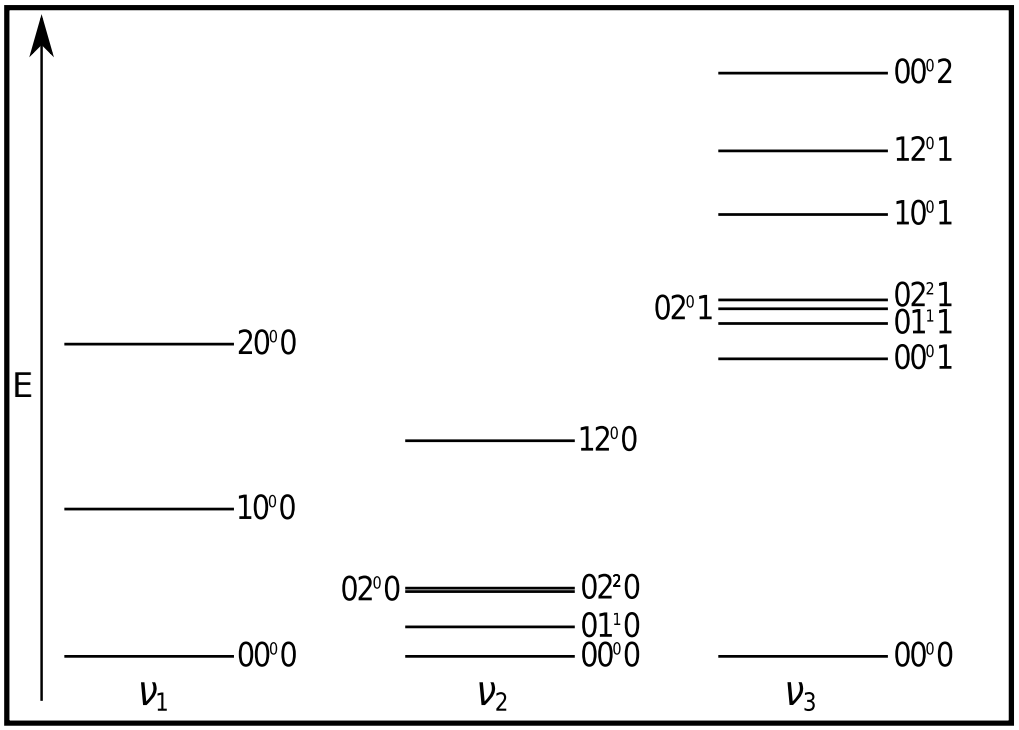

Figure 2.3: Schematic representation of a term diagram with three vibrational modes of a linear triatomic molecule, like Al_2O . The low lying ν_2 mode is doubly degenerated.

2.2.1 Rotation in Exited Vibrational States

Excitation of molecules leads to increasing bond lengths in excited parallel modes due to the asymmetry of the vibrational potential. Due to the larger distances between the atoms, the rotational constant B shrinks. Excitations in the bending vibration lead exactly to the opposite. Here, the bond lengths are getting shorter in comparison to the ground state and therefore, a slightly larger rotational constant B is obtained. Neglecting higher orders, the following equation results for the rotational constant B_v:

$$B_v = B_e - \sum_i \alpha_i \left(v_i + \frac{d_i}{2} \right) + \gamma l^2, \tag{2.13}$$

where B_e is the rotational equilibrium constant, α_i is the interaction constant representing the first order correction for B_v for the i-th vibrational mode, v_i is the vibrational quantum number for the i-th vibrational mode, d_i is the degeneration of this mode and γl^2 corrects the small shift in energy levels caused by the vibrational angular momentum.

The vibrations also affect the centrifugal distortion constant. The centrifugal distortion

constant D_v is therefore described by the following equation:

$$D_v = D_e + \sum_i \beta_i \left(v_i + \frac{d_i}{2} \right). \tag{2.14}$$

Furthermore, based on the double degenerated bending vibration (ν_2^l) Equation 2.8 needs to be modified, because the vibrational angular momentum causes a shift of the energy levels:

$$E_{\text{rot}}(J) = B_v[J(J+1) - l^2] - D_v[J(J+1) - l^2]^2. \tag{2.15}$$

In a degenerated bending vibrational mode ν_2^l with a vibrational angular momentum, a small splitting of the rotational lines occurs. In the case of a Π state such as (01^11) and (01^10) the resulting energy shift ΔE_{rot} of this splitting is given by the following equation:

$$\Delta E_{\text{rot}} = \pm \frac{q_l}{2} J(J+1), \tag{2.16}$$

where $\pm$ depends on the parity of the state (e, f) and q_l is the l-type doubling constant between vibrational and rotational motion. For linear symmetric molecules XY_2, q_l is given as follows:

$$q_l = 2\frac{B_e^2}{\omega_2} \left(1 + \frac{4\omega_2^2}{\omega_3^2 - \omega_2^2} \right), \tag{2.17}$$

where ω_2 and ω_3 are the harmonic frequencies of the vibrational modes. Neglecting the vibrations, the transition energy is calculated as follows:

$$\begin{aligned} \nu_{J+1 \leftarrow J} &= E_{\text{rot}}(J+1) - E_{\text{rot}}(J) \\ &= 2B_v(J+1) \pm \frac{1}{2} q_l (v_i + 1)(J+1) - 4D_v(J+1)[(J+1)^2 - l^2], \end{aligned} \tag{2.18}$$

with l as quantum number for vibrational angular momentum.

In addition, it should be noted that if two vibration-rotational energy levels of the ν_2 mode are too close together, as is the case of Al_2O (e.g. (02^00) and (02^20)), perturbations between the energy levels occur, which are noticeable in the spectrum. This perturbations are found in the literature under different names such as l-type interaction, l-type resonance effect or '$\Sigma - \Delta$' interaction splitting. This interaction is described by adding the off-diagonal matrix elements to the Hamiltonian using the following equation:

$$\left\langle l = 2, J | \hat{H} | l = 0, J \right\rangle = \frac{q_t + q_{tJ} J(J+1)}{2} \sqrt{2J(J+1)(J(J+1) - 2)}, \tag{2.19}$$

where the perturbation parameters q_t and q_{tJ}, which handles distortion effects, are scaling parameters of the resonance strength. For detailed descriptions of this effect see the work of Yamada *et al.* [33,34].

2.2.2 Selection Rules

While high energies are needed to excite a vibrational transition, rotational transitions are always excited, too. This means that rotational transitions always occur within a vibrational band and are visible in the spectrum in high-resolution infrared spectroscopy. These transitions always follow certain selection rules:

$$\Delta J = (0), \pm 1 \quad \text{and} \quad \Delta v = 0, 1, (2, 3, ..). \tag{2.20}$$

The transition $\Delta J = 0$ occurs whenever electronic angular momentum L, spin orbital momentum S or vibrational momentum l is unequal to 0. The transitions corresponding to the three different selection rules are divided into three different branches. This is illustrated in Figure 2.4. Transitions that correspond to the selection rule $\Delta J = +1$ are called R branch. Transitions corresponding to selection rule $\Delta J = -1$ are called P branch. And if the transition $\Delta J = 0$ is allowed, these transitions are named Q branch. The energy of a ro-vibrational energy level is given by the following equation:

$$E_{vJ} = E_{\text{vib}}(v_1, v_2^l, v_3) + E_{\text{rot}}(J), \tag{2.21}$$

where $E_{\text{vib}}(v_1, v_2^l, v_3)$ is the vibrational part and $E_{\text{rot}}(J)$ is the rotational part.

Within a molecular spectrum the vibrational bands are divided into the following groups: fundamental transitions, overtone transitions, hot band transitions and combination band transitions.

Fundamental transitions are transitions originated from the ground state. Transitions excited from higher energy levels, i.e. $v'' \neq 0$, obeying the selection rule $\Delta\nu = 1$, are so-called hot band transitions. The overtone transitions include transitions like : $v = 2 \leftarrow 0, v = 3 \leftarrow 0, ...$ All transitions where the quantum numbers change for two or more modes, such as $v = (011) \leftarrow (000)$ are called combination band transitions.

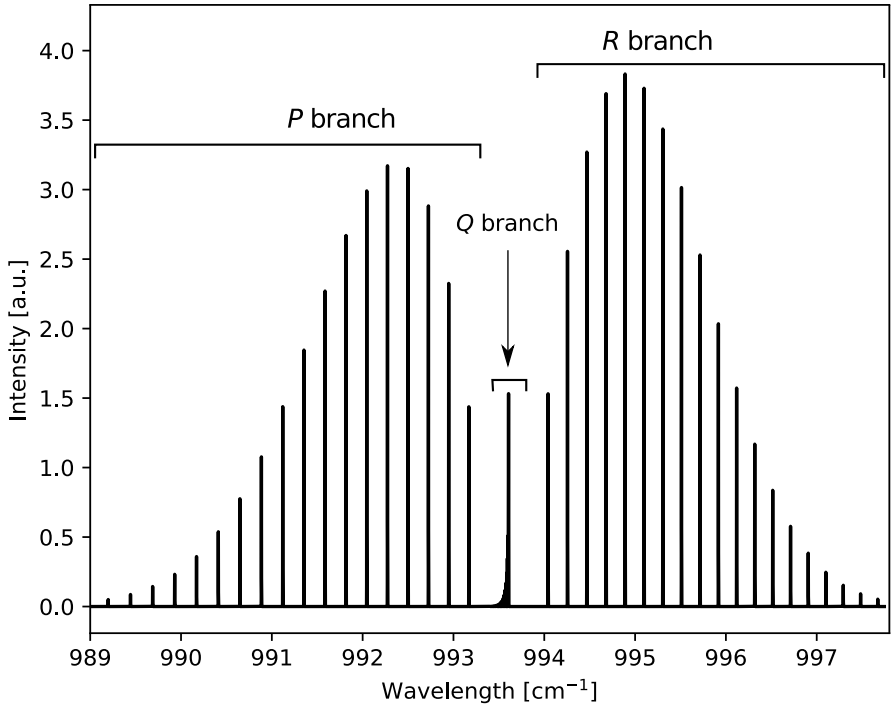

Figure 2.4: Simulation of the rotational resolved vibrational transition $(01^11) \leftarrow (01^10)$ of the Al_2O molecule in a frequency range from $989\,\mathrm{cm}^{-1}$ to $998\,\mathrm{cm}^{-1}$. The P branch, the Q branch and the R branch are indicated.

2.2.3 Nuclear Spin Statistics

If a molecule contains two or more identical atoms, they can be exchanged using the permutation operator $\hat{P}_{12}$. This changes the the number of possible rotational states to be occupied and thus also changes the intensity of the rotational lines. The exchanging also has an effect on the total wave function ψ_{total}, which is composed as follows using the Born-Oppenheimer approximation:

$$\psi_{\mathrm{total}} = \psi_{\mathrm{el}}\psi_{\mathrm{vib}}\psi_{\mathrm{rot}}\psi_{\mathrm{spin}}. \tag{2.22}$$

By applying the permutation operator to a wave function, the following equation must be satisfied:

$$\hat{P}\psi_{\mathrm{total}} = \pm\psi_{\mathrm{total}}, \tag{2.23}$$

where $+$ here stands for symmetrical states and $-$ for antisymmetrical states.

If two particles with integer nuclear spin (bosons) are exchanged, the total wave function has to be symmetric. This means that the sign of the total wave function has to

be positive. If the exchangeable particles have a half-integer spin (fermions), the total wave function is antisymmetric. This results in the sign of the total wave function becoming negative.

The parts ψ_{el} and ψ_{vib} of the total wave function are both symmetrical in the ground state compared to an exchange of two identical atomic nuclei. This means that the product $\psi_{\text{rot}}\psi_{\text{spin}}$ has to be symmetric or antisymmetric, depending on whether bosons or fermions are exchanged.

The molecule studied in this work consists of two aluminum atoms with a nuclear spin of $I = \frac{5}{2}$ and a central oxygen atom with a nuclear spin of $I = 0$. For the two aluminum atoms A and B, the following notations are introduced for the projection m_I:

$$\begin{aligned} \alpha &=\mid m_I = +\frac{1}{2} > & \beta &=\mid m_I = -\frac{1}{2} > \\ \gamma &=\mid m_I = +\frac{3}{2} > & \delta &=\mid m_I = -\frac{3}{2} > \\ \varepsilon &=\mid m_I = +\frac{5}{2} > & \zeta &=\mid m_I = -\frac{5}{2} > . \end{aligned}$$

The symmetric and the antisymmetric spin wave function ψ_{spin} can now be formed, considering that Equation 2.23 is fulfilled. Thus, Atom A and Atom B each can have 6 configurations, which leads to 36 combinations in total. As a result, 21 symmetric and 15 antisymmetric spin wave functions are formed. Three possible combinations are demonstrated in the following example:

$$\psi_{\text{spin}} = \begin{cases} \alpha(A)\alpha(B) \\ \dfrac{\alpha(A)\beta(B) + \beta(A)\alpha(B)}{\sqrt{2}} \end{cases} \quad \text{symmetric,} \tag{2.24}$$

$$\psi_{\text{spin}} = \quad \frac{\alpha(A)\beta(B) - \beta(A)\alpha(B)}{\sqrt{2}} \quad \text{antisymmetric.} \tag{2.25}$$

Based on their spin statistical weight, the successive rotational transitions occur with an alternating intensity with a ratio of $\frac{7}{5}$.

In general for two exchangeable atoms in a molecule with a nuclear spin I, $(2I+1)(I+1)$ symmetric and $(2I+1)I$ antisymmetric nuclear spin wave functions are possible. Thus

the spin statistical weight follows the rule:

$$g_{\mathrm{n}} = \frac{g_{\mathrm{spin}}(\mathrm{sym})}{g_{\mathrm{spin}}(\mathrm{antisym})} = \frac{(I+1)}{I} = \frac{\frac{5}{2}+1}{\frac{5}{2}} = \frac{7}{5}. \tag{2.26}$$

2.2.4 Boltzmann Plot

Using Boltzmann plot analysis (also called rotation diagram), information of the rotational temperature within a vibrational band of the measured molecule are determined.

In a thermodynamic equilibrium the relative occupation of the energy levels N_{J_l}/N, with the lower quantum number J_l, within an ensemble of molecules follows a Boltzmann distribution with the temperature T:

$$\frac{N_{J_l}}{N} = \frac{2J_l+1}{Q_{\mathrm{rv}}} \cdot \exp\left(\frac{-E_{\mathrm{rot}}(J_l)}{k_B T}\right), \tag{2.27}$$

where E_{rot} describes the rotational energy level and Q_{rv} represents the partition function. N_{J_l} in Equation 2.27 is the state-specific population for the lower state J_l, which is obtained from line intensities $\int \tau d\nu$ as[35]:

$$N_{J_l} = \frac{8\pi\nu^3}{c^3}\frac{g_l}{A_{ul}g_u g_n}\left[1-\exp\left(-\frac{h\nu}{k_B T_{\mathrm{ex}}}\right)\right]^{-1}\int \tau d\nu, \tag{2.28}$$

where A_{ul} is the Einstein coefficient and g_l and g_u are the rotational degeneracy factors $g_{l/u} = 2J_{l/u}+1$ of the J_l lower and J_u upper rotational level.

From Equation 2.27 and Equation 2.28 a linear correlation between the logarithmic line intensity and the energy level is obtained:

$$\underbrace{\log\left(\frac{8\pi\nu^3\int\tau d\nu}{c^3 A_{ul}g_u g_n}\right)}_{\tilde{I}=\log I(J)} = \underbrace{\log(N)-\log(Q_{\mathrm{rv}}(T))\cdot\left(1-\exp^{-\frac{h\nu}{k_B T}}\right)}_{x(T)} - \underbrace{\frac{E_{\mathrm{rot}}(J_l)}{k_B T}}_{m(T)\cdot E_{\mathrm{rot}}(J)}. \tag{2.29}$$

As a result, the temperature is derived from either $m(T)$ or $x(T)$, where both parameters are obtained from a linear fit of the form: $\tilde{I} = x - m \cdot E$.

3 The Experiment

The following chapter describes the experimental setup used to measure the rotationally resolved vibrational spectrum of Al_2O. First, an overview of the setup is given and the properties of the experimental parts are discussed. Then the laser ablation technique is described, as well as how the supersonic jet effects the molecular infrared signal. Thereon, the optical setup including the quantum cascade laser (QCL) will be introduced, followed by the measuring method. Next a step-by-step manual is given how to process and calibrate the measured data to gain a frequency calibrated spectrum. In the final section line broadening effects are briefly discussed.

3.1 Experimental Setup

The setup of the experiment is shown in Figure 3.1. The radiation source used in this experiment is a tunable external-cavity Quantum Cascade Laser (ec-QCL) operating in a continuous wave (CW) mode between 9.28 µm and 10.31 µm. The frequency of the radiation is modulated with 200 kHz to measure frequency intervals of $0.025\,\mathrm{cm}^{-1}$. The radiation is divided into 3 beams using beamsplitters. One beam passes through a Herriott-type multipass cell filled with a reference gas, one beam passes through an etalon and the third beam, containing 90% of the main beam intensity, passes through a vacuum chamber, where Al_2O is produced via laser ablation. Each beam is focused onto an mercury cadmium telluride (MCT) detector.

The etalon and the reference gas are required for a precise frequency calibration of the measured spectrum. For the here used frequency range methanol (CH_3OH) has been chosen as reference gas. The gas is filled in a 1 m long Herriott-type multipass cell wherein 24 reflections per mirror are adjusted which leads to a total absorption path length of ~ 50 m. The spectrum which was measured using an internally coupled ('ic') etalon has an free spectral range (FSR) of $0.006\,\mathrm{cm}^{-1}$ leading to four etalon peaks per

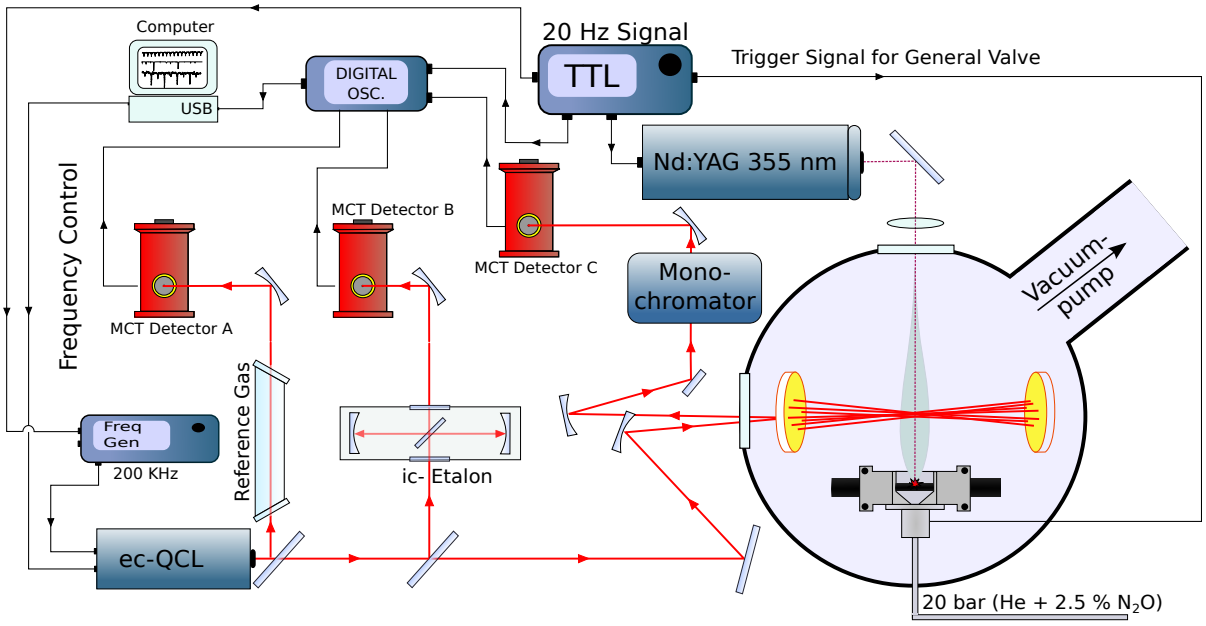

Figure 3.1: Schematic representation of the experimental setup for the detection of Al_2O including an absorption spectrometer and the a laser ablation source. (Adapted from[36].)

sweep.

The main beam of the ec-QCL passes through a multipass cell in a vacuum chamber, where also the molecules under investigation are produced, via laser ablation. After the beam leaves the vacuum chamber, it first passes through a grating monochromator before it is detected by a liquid nitrogen-cooled fast IR-detector from Vigo-Systems with a build in preamplifier from Neoplas Control.

In a preliminary work an Al_2O spectrum was scanned with a similar setup in a frequency range form $984.1\,\mathrm{cm}^{-1}$ to $992.2\,\mathrm{cm}^{-1}$. The difference was to the described setup that instead of an ec-QCL a distributed feedback QCL (DFB-QCL) was used at that time. Since the Al_2O spectrum exceeds the spectral range of the DFB-QCL further measurements with the ec-QCL were necessary.

3.2 Laser Ablation

The production of the Al_2O molecules was done by laser ablation. The geometry of the ablation source is illustrated in Figure 3.2. A high-energy laser pulse was focused on a rotating solid aluminum rod and creates a plasma. The pulsed Nd:YAG ablation laser

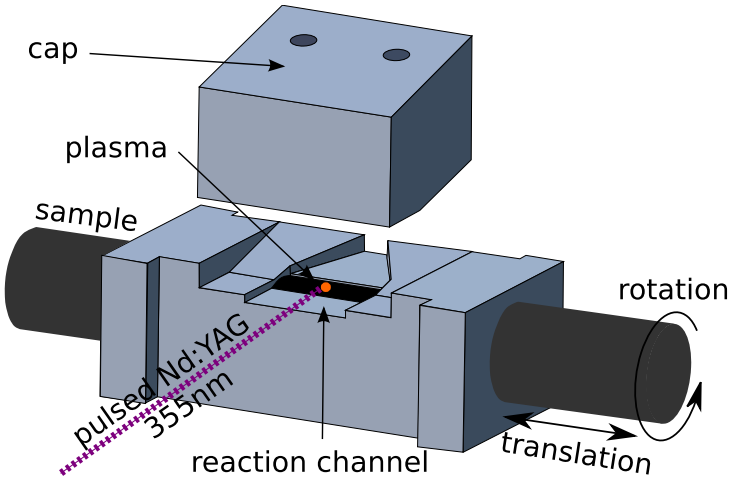

Figure 3.2: Setup of the ablation source used to produce Al_2O. Inside the source is a movable sample rod on which a plasma is formed using a focused Nd:YAG laser beam. A buffer gas mixture of a buffer and a donor gas passed over the plasma and molecules can form in the subsequent reaction channel. When the molecules leave the source and enters the vacuum region an adiabatic expansion and jet formation occurs.

(Continuum Inlite II) used in this work, has an output wavelength of 355 nm and an output power of up to 33.5 mJ at a repetition rate of 30 Hz with a pulse width of 5 - 7 ns. A laser intensity in the order of 0.5 - 1.0 $\frac{\mathrm{GW}}{\mathrm{cm}^2}$ [37] is required, to form a plasma. The laser beam was focused on the sample using a lens with a focal length of 50 cm. The focused area on the sample had a diameter of 20 µm. This resulted in a radiation intensity of 10^{11} $\frac{\mathrm{W}}{\mathrm{cm}^2}$, which satisfied the condition for plasma formation. This formation took place due to the interaction of laser photons with the solid surface, so that the in-atomic bonds in the solid matter were broken and atoms could be released. Especially ions, atoms and small diatomic to triatomic molecules could be formed within the plasma cloud [38].

In order to produce reactive molecules, an inert buffer gas (in this case helium (He)), was mixed with a donor gas (in this case nitrous oxide (N_2O)) and passed over the ablation plasma. The gas mixture used contained 2.5% N_2O in helium. The laser ablation source is shown in Figure 3.2. To produce the molecules a solid aluminum rod inside the source was rotating and translating, while a Nd:YAG-laser beam was focused onto it. A plasma was generated on the target, which reached temperatures of several thousand Kelvin. In the rear of the ablation source a pulsed Parker General Valve (Series 9) with a 0.5 mm opening was placed. The gas mixture with a backing pressure of 20 bar was flowing above the plasma and subsequently through a reaction channel of 8 mm length. By means of collision processes in the reaction channel of the

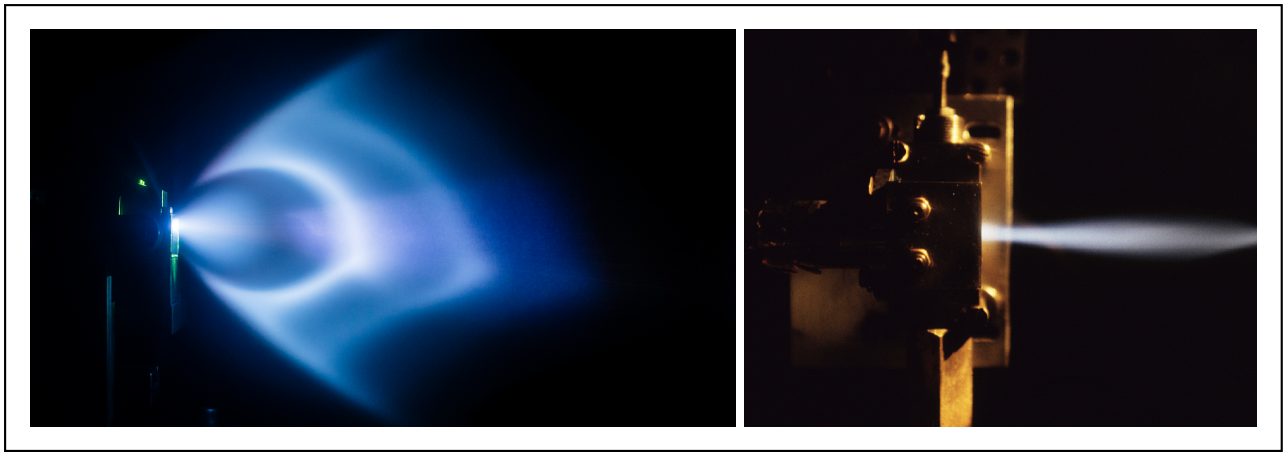

Figure 3.3: Image of a supersonic jet expanding into the vacuum chamber. Left: Side view of a titanium jet with argon as buffer gas. Right: Top view of a carbon jet with helium as buffer gas.

source, molecules and atoms from the plasma reacted with the donor gas, whereby new molecules were formed. The reaction channel used has a height of 1 mm, a width of 12 mm and a length of 8 mm. Leaving the reaction channel trough a rectangular slit the gaseous mixture expanded adiabatically into a vacuum chamber with $1.2 \cdot 10^{-2}$ mbar. Due to the slit exit of the reaction channel the adiabatic expansion reduced the particle density and cooled the gas down to temperatures of around 120 K to 20 K depending on the molecules and the buffer gas. A supersonic jet formed in the vacuum chamber, in which the gas expanded predominantly in the vertical direction. Figure 3.3 shows the expanding mixture forming in a supersonic jet (a 2D-mach disk). The particles in the jet moved at a higher speed than their local acoustic velocity. Shock fronts formed at the edge of the expanding jet, due to the interaction of the background gas in the chamber with the jet. The region in front of the shock front is a specific zone, the so called -zone of silence[39]- of the 2D-mach disk. In this zone of silence the molecules flow almost with no collisions until the pressure drops to the ambient value.

The zone of silence is the optimal area to observe the produced molecules spectroscopically. The IR laser beam of the QCL intersects the zone of silence several times. A Herriott-type multipass cell is located in the vacuum chamber, to extend the absorption path of the laser beam. Such a multipass cell consists of two spherical mirrors with the same focal length, which are facing each other. One of these two mirrors has a hole enabling the IR laser beam to enter the multipass cell. After n passes, the laser beam leaves the cell through the entrance hole. Depending on the selected focal length and the distance between the two mirrors, a different number of reflections is possible.

The mirrors used in this work have a focal length of $f = 65\,\text{mm}$ and were positioned at a distance of 189.8 mm so that 42 passes could take place. The entrance hole with a diameter of 3.5 mm is placed 5 mm next to the center of the mirror.

3.3 Quntum Cascade Laser (QCL)

In order to measure a rotationally resolved molecular spectrum, a radiation source with a line width being smaller than the expected molecular line width was required. Continuous wave laser systems are particularly suitable for fulfilling this condition. Furthermore, it was important that the laser covers a range of several wave numbers in order to be able to record sufficient lines in the absorption spectrum. In this work, in the frequency range at 10 µm, quantum cascade lasers (QCL) were particularly well suited.

A QCL is build up of a periodic arrangement of unit cells (see Figure 3.4). Each cell can be split into an injector zone and an active zone. The active zone of a QCL consists of several periodically arranged layers of different semiconductor materials such as GaAs/AlGaAs. The layers are produced by vapor deposition. Due to band gaps of different sizes in the evaporated layers, potential wells are formed. The width of the potential wells is determined by the semiconductor layer thickness. Application of a voltage through the layer plane creates a step-like arrangement of energy levels. Figure 3.4 schematically shows the energy levels in the conduction band of a QCL. The two different zones of the unit cells, the active zone and the injector zone, are illustrated. The actual laser transitions take place within the active zone. It consists of two potential wells. Within these potential wells discrete energy levels are formed. The radiation transition takes place between the higher lying energy level (3) and the lower energy level (2). Since the energy level (3) is populated from the nearby injection zone, this level (3) is more populated than level (2), thus, resulting in a population inversion situation. A further energy level (1), which has the same energy as the energy level (2), when the voltage is applied, enables the depopulation of the lower laser level. Due to the tunnel effect, the electrons are transported into the next adjacent injection zone.

Within the injector zone, a superposition of multiple electronic states occur, resulting in the formation of the so-called miniband. This miniband serves as an electron reservoir for the upper energy level (3) of the next period. A minigap is formed above the

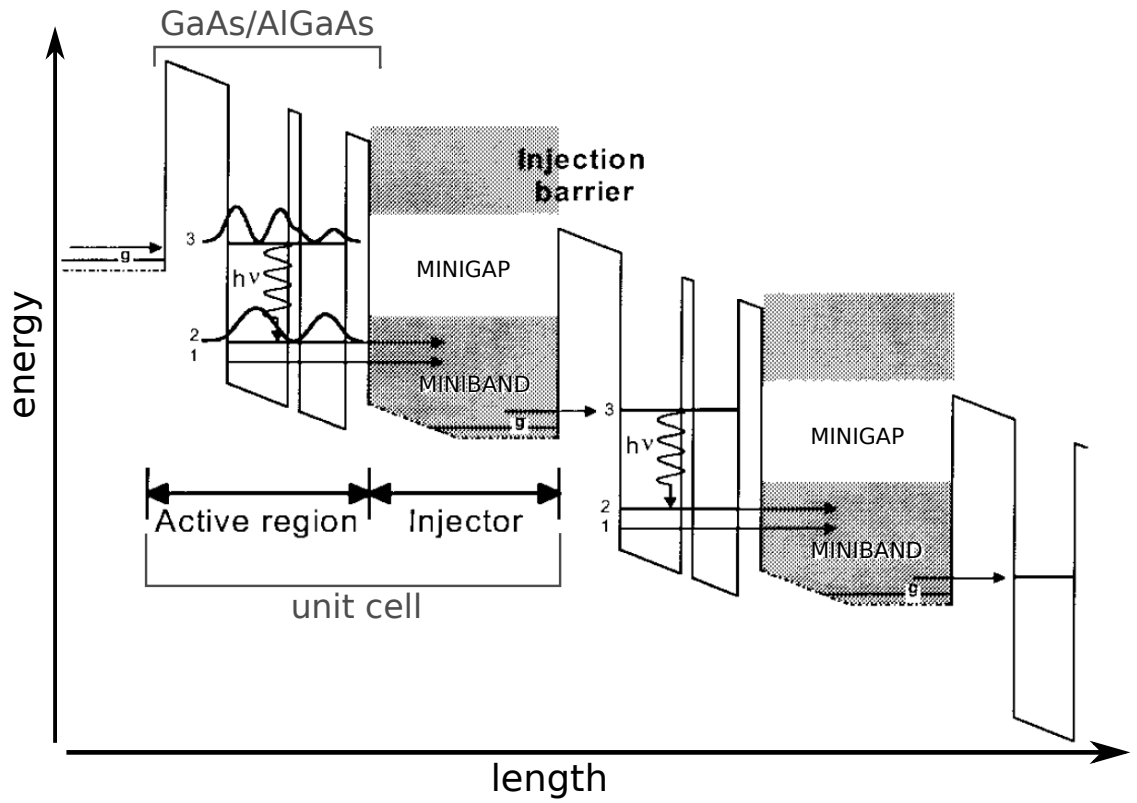

Figure 3.4: Energy scheme of the conduction band of QCL. (Analogously to[41].)

miniband, which prevents the direct electron flow from the upper energy level into the miniband. By resonant tunneling, an active transport of the electrons into the adjacent active zone takes place.

A QCL typically contains 10 to 100 consecutive periods. A more detailed description of how a QCL works can be found in the book by Faist[42].

In this work a mode-hop-free external cavity quantum cascade laser (ec-QCL) from Daylight Solutions was used. This laser covers a frequency range from 970 cm^{-1} to 1074 cm^{-1} with an output power of 100 mW. A current around 700 mA is used to operate this laser. To tune the frequencies, a sinusoidal modulation of 200 kHz is used, resulting in a frequency sweep of 0.025 cm^{-1} width. The current modulation is done with the help of a programmable Function Generator HM8130 from Hameg.

3.4 Measuring Method

In this work a molecular spectrum was measured by using the so-called InfraRed Frequency Alternating Sweep Technique (IR-FAST)[43]. The aim was to record a small

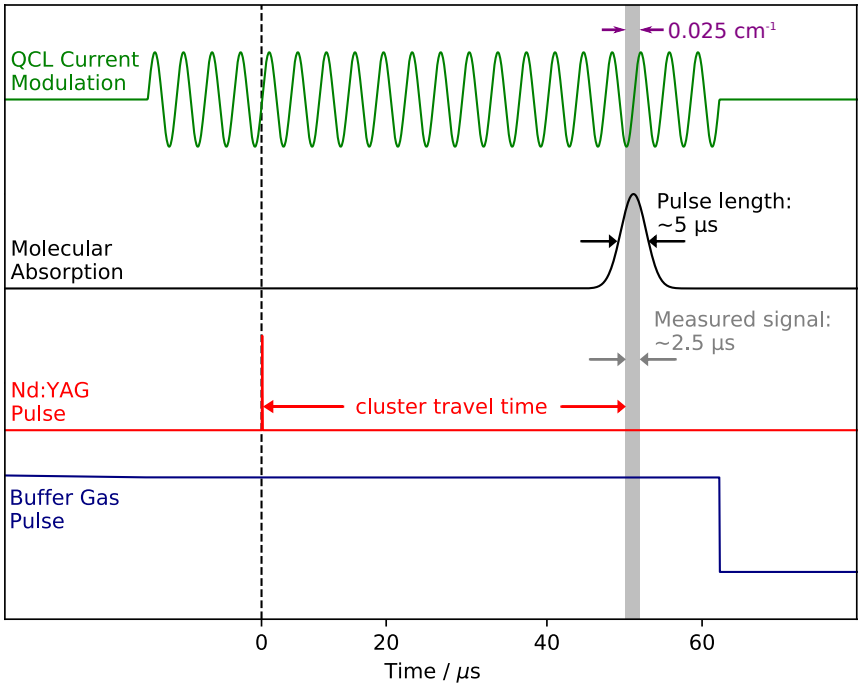

Figure 3.5: Schematic representation of the timings used in the IR-FAST technique. The QCL current modulation (green), the Nd:YAG pulse (red), the buffer gas pulse (blue) and the time at which the absorption peak appears (black).(Adapted from[43].)

spectral interval of the molecules generated by a single laser ablation process using a fast frequency sweep of the IR radiation.

A timing scheme used for IR-FAST is illustrated in Figure 3.5. Due to the different timings to be considered, 4-channel TTL pulse generator (9300 Series), from quantum composers, was used to synchronized several devices involved in the detection process. In order to probe the molecules using IR radiation, it was necessary to match the molecular flight time with the infrared sweep pulse time. The speed of the molecules in the supersonic jet depended on their mass and the buffer gas was used.

Within a gas pulse of the general valve, of about 500 µs, a 5 ns pulse from the Nd:YAG laser was focused on the sample. Approximately 45-55 µs later the molecules passed through the multipass cell in the zone of silence of the jet, which allowed the detection of an absorption signal, lasting 5 µs.

In order to record the spectra, a fast IR detector (1 GHz) from Vigo-Systems in combination with a preamplifier, from Neoplas Control, cooled by liquid nitrogen temperatures to reduce noise effects, was used. For the here described detection scheme to work, a minimum response time of the detector of a few nanoseconds, corresponding

to 300 MHz, was required. To reduce additional noise due to thermal background a grating monochromator was used in front of the detector, which serves as an infrared bandpass filter with a bandwidth of about $1\,\mathrm{cm}^{-1}$. The data measured by the detector were transferred to a computer and stored using a PicoTech 4-channel oscilloscope (PicoScope5444B) with 14-bit resolution and a sampling rate of 125 MS/s per channel.

With a repetition rate of 20 Hz a 30 seconds measurement resulted in 600 spectra that were taken, each covering the same $0.025\,\mathrm{cm}^{-1}$ frequency range. After 30 seconds, the ec-QCL stepped forward by $0.01\,\mathrm{cm}^{-1}$. This guaranteed a sufficiently large overlap range of the measured sweeps. With this measuring technique, a wave number was scanned within 50 minutes.

As already mentioned a small part of the spectrum, which comprises $8.1\,\mathrm{cm}^{-1}$, had been measured using a step-scan technique. These data were also used in the Al_2O analysis of this work. Thus, a brief description of the measuring procedure is given. A DFB-QCL was used and the way the data was acquired differed from the way it has been done for this work. A distributed feedback cw-QCL, from Alpes laser, was used covering a frequency range from $984\,\mathrm{cm}^{-1}$ to $992\,\mathrm{cm}^{-1}$, with an output power of 50 mW. By slowly stepping through the QCL frequencies with a step width of $1.62{\cdot}10^{-4}\,\mathrm{cm}^{-1}$ per second, i.e. 3 MHz/s, the spectrum was recorded. Each data point was averaged over 40 jet pulses before the laser stepped further to the next frequency. As soon as the laser excited a molecule, an absorption signal appeared for a few tens of a microsecond, which was recorded by a MCT detector (1 MHz). A baseline subtraction was done by means of a boxcar integrator and time frame subtraction. For this two 10 µs long time frames were used, with one covering the time where the molecules interact with the IR beam (A) and the other one at a later time (B). These two time frames were then subtracted from each other (A-B).

3.5 Data Processing and Calibration

To obtain a precise frequency calibration, an internally coupled ('ic') interferometer (etalon) and a reference gas cell were used for both above mentioned measurement techniques to calibrate the spectra. For this purpose, 5 % of the infrared radiation was guided into the etalon. The used 'ic' interferometer has an FSR of $0.006\,\mathrm{cm}^{-1}$, and thus, four etalon fringes were present in a spectral range of $0.025\,\mathrm{cm}^{-1}$. In order to determine the absolute frequency of the spectrum, a reference gas was used and

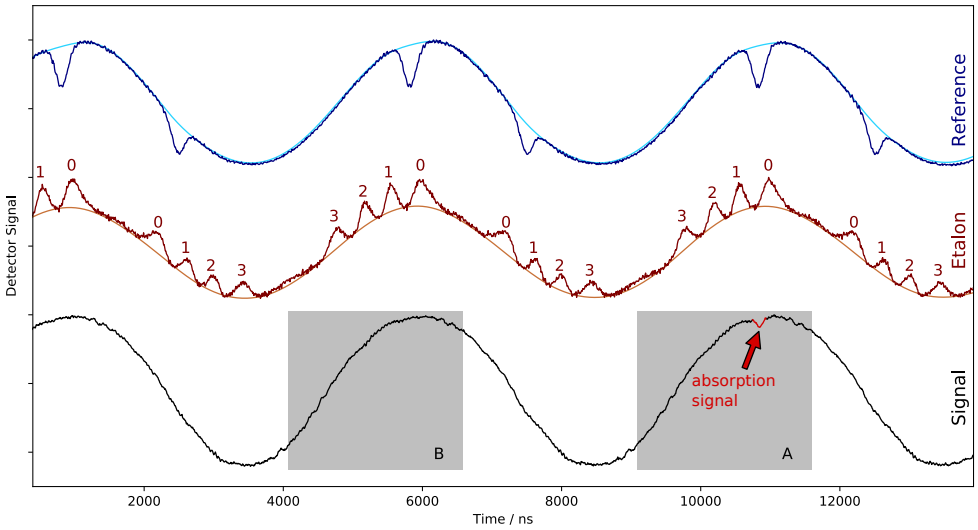

Figure 3.6: Representation of the raw data of a measurement. The measurements of the reference gas (blue), the etalon (brown) and the measurement signal (black) is shown. In the grey box A, the measuring signal is observable. The baseline correction of the reference gas and the etalon is shown in light blue and light brown. For the baseline correction of the measurement signal, the grey box B is subtracted from the box A. (Adapted from[43].)

measured simultaneously to the main measurement. In this case methanol (CH_3OH) was used and filled in a 1 m long Herriott-type multipass cell with 24 reflections per mirror and at a pressure of ~ 0.1 mbar. To record the calibration spectra, two four-stage thermoelectrically cooled detectors, form Vigo systems, were used. Each of these detectors had a time constant of better than a few nanoseconds.

In order to evaluate the molecular spectrum recorded by IR-FAST, several data reduction steps were required. First, there are three different spectra, the Al_2O signal spectrum, the etalon spectrum and the reference gas spectrum, as is seen in Figure 3.6. It has to be noted that the path length referring to the signal spectrum and the reference gas spectrum was longer due to the used multipass cells compared to the path length of the etalon beam path. This was remedied by neglecting a few data points of the two spectra with the longer absorption path.

Due to the used modulation technique all measured spectra showed a strong sinusoidal baseline. Thus, a baseline correction needed to be performed. For the measurement signal, a baseline correction was performed by subtracting one time frame with the absorption peak (gray Box A, Figure 3.6) from the time frame of a previous sinusoidal modulation cycle without peak (gray Box B, Figure 3.6). The baseline correction of the etalon spectrum and the reference gas spectrum was done using an algorithm by

Oller-Moreno *et al.*[44] called Peaked Signal's Asymmetric Least Squares Algorithm (psalsa). The baselines are shown in Figure 3.6 as a light blue and light brown line.

In the etalon spectrum four fringes appeared in each sweep i.e. in the time frame corresponding to the gray box A in Figure 3.6, and were numbered consecutively. By a sinusoidal fit to the numbered etalon fringes, the time axis of the measurement was converted into a linear frequency axis. The spectra with the calibrated frequency axis could then be averaged, i.e. 600 recorded spectra per frequency interval where reduced to one averaged spectrum. Thereafter, spectra covering different frequency regions were joined together. This was possible due to an overlap range of $0.015\,\mathrm{cm}^{-1}$ between each sweep. Once all the sweeps were connected, the spectrum was completed, but still in a linearized frequency axis in units of etalon fringes. In order to assign the spectrum to the correct frequencies, the peaks of the reference gas were calibrated on the basis of literature data. Finally, the calibration was applied to the signal spectrum and a finished absolutely calibrated spectrum of the measured molecule with an accuracy of $4 \cdot 10^{-4}\,\mathrm{cm}^{-1}$ was available.

3.6 Line Broadening

Looking closely at an absorption spectrum, it can be seen that the lines of the transitions are undergoing a certain broadening. This broadening of the lines is mainly caused by three different effects. The first of these three effects is the natural lifetime broadening. This effect is always present because it is caused by the limited lifetime of the excited states. The limited lifetime of excited states is caused by spontaneous decay.

The so-called pressure broadening is the second effect that causes a line broadening. The decisive factor of this effect is the time between the collisions, or the collision rate $\Delta\nu_{\mathrm{collision}}$, which can be calculated as follows:

$$\Delta\nu_{\mathrm{collision}} = b \cdot p, \tag{3.1}$$

where p is the pressure and b is the pressure broadening coefficient representing the line broadening at a given pressure. In Equation 3.1 and in all following equation, $\Delta\nu$ represents the full width at half maximum (FWHM).

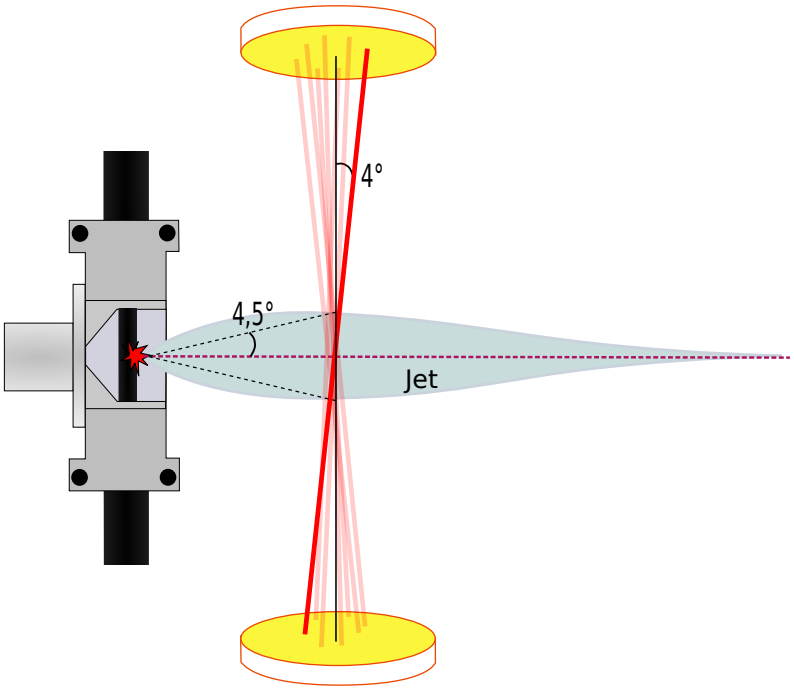

Figure 3.7: Sketch of an expanding jet and a multipass configuration. An angle $\alpha = 4°$ is obtained which causes geometric Doppler broadening.

The third effect is the Doppler broadening. The Doppler broadening is caused by thermal movement of the molecules. This thermal movement causes the molecules to absorb at different frequencies due to the Maxwell-Boltzmann distribution velocity. The resulting line broadening $\Delta\nu_{\mathrm{D,temp}}$ is calculated using the following formula:

$$\Delta\nu_{\mathrm{D,\,temp}} = 2\nu_0\sqrt{\frac{2k_BT\ln(2)}{mc^2}} = 7.1\cdot10^{-7}\nu_0\sqrt{\frac{T}{M}}, \tag{3.2}$$

where m is the mass of the molecules, M is the molar mass of the molecules, T is the kinetic temperature of the molecules, ν_0 is the transition frequency, c is the speed of light and k_B is the Boltzmann constant.

In addition to the thermal Doppler broadening, a geometric Doppler broadening also occurs due to the shape of the jet. The molecules can expand in the jet in a horizontal direction with an angle of $\pm53\,°$ and in a vertical direction with an angle of $\pm4.5\,°$. Also the laser beam of the QCL does not reach the expanding jet exactly perpendicularly due to the reflections in the multipass cell (see Figure 3.7). Thus an angle α is formed in which the QCL beam passes through the jet, which leads to the geometrical Doppler broadening. With the aid of the frequency ν and the resulting angle α the geometric

Doppler broadening is calculated as follows:

$$\Delta\nu_{\mathrm{D,\,geom}} = 2 \cdot \nu_0 \cdot \frac{\Delta v}{c} = 2 \cdot \nu_0 \cdot \frac{v \cdot \sin(4°)}{c}. \tag{3.3}$$

The velocity v of the molecules is obtained from the time of flight of $15 \pm 1\,\mu\mathrm{m}$ which they need to reach the probing area at 2.5 cm distance. If a constant velocity is assumed, a velocity of $v = 1666\,\frac{\mathrm{m}}{\mathrm{s}}$ results for the molecules. For the angle α the result is an angular interval of $-4\,° < \alpha < 4\,°$.[36] The evaluation of the broadening will follow in Chapter 4.1

4 Analysis and Discussion of the Experimental Results

4.1 Analysis of the Al_2O Spectrum

During master thesis, a rotational-resolved infrared spectrum of dialuminum monoxide (Al_2O) was measured. An infrared spectrometer was used, covering a frequency range from $970\,cm^{-1}$ to $1074\,cm^{-1}$. Al_2O is a linear triatomic molecule (see Figure 4.1) of $D_{\infty h}$ symmetry.

An overview of the measured frequency range of $976.5\,cm^{-1}$ to $1010\,cm^{-1}$ is shown in Figure 4.2. The structure of the measured spectrum corresponds to the expectations of a linear molecular spectrum, yet, showing several vibrational bands.

The program 'Pgopher'[45] was used, to analyze the spectrum. First, the measured molecular spectrum is processed, so that it is usable for the program. The 'LoomisWood Plot' function of 'Pgopher' is used to assign vibrational bands and associated rotational transitions. To assign vibrational bands, the measured spectrum is first plotted several times on top of each other (Figure 4.3). If now peaks are selected which could belong to one vibrational band, they are shifted horizontally by an amount, given by a function

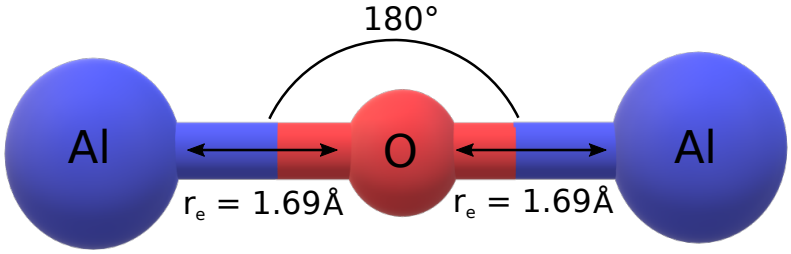

Figure 4.1: Sketch of a linear dialuminum monoxide molecule of $D_{\infty h}$ symmetry with an equilibrium bond distance of $r_e = 1.69$.

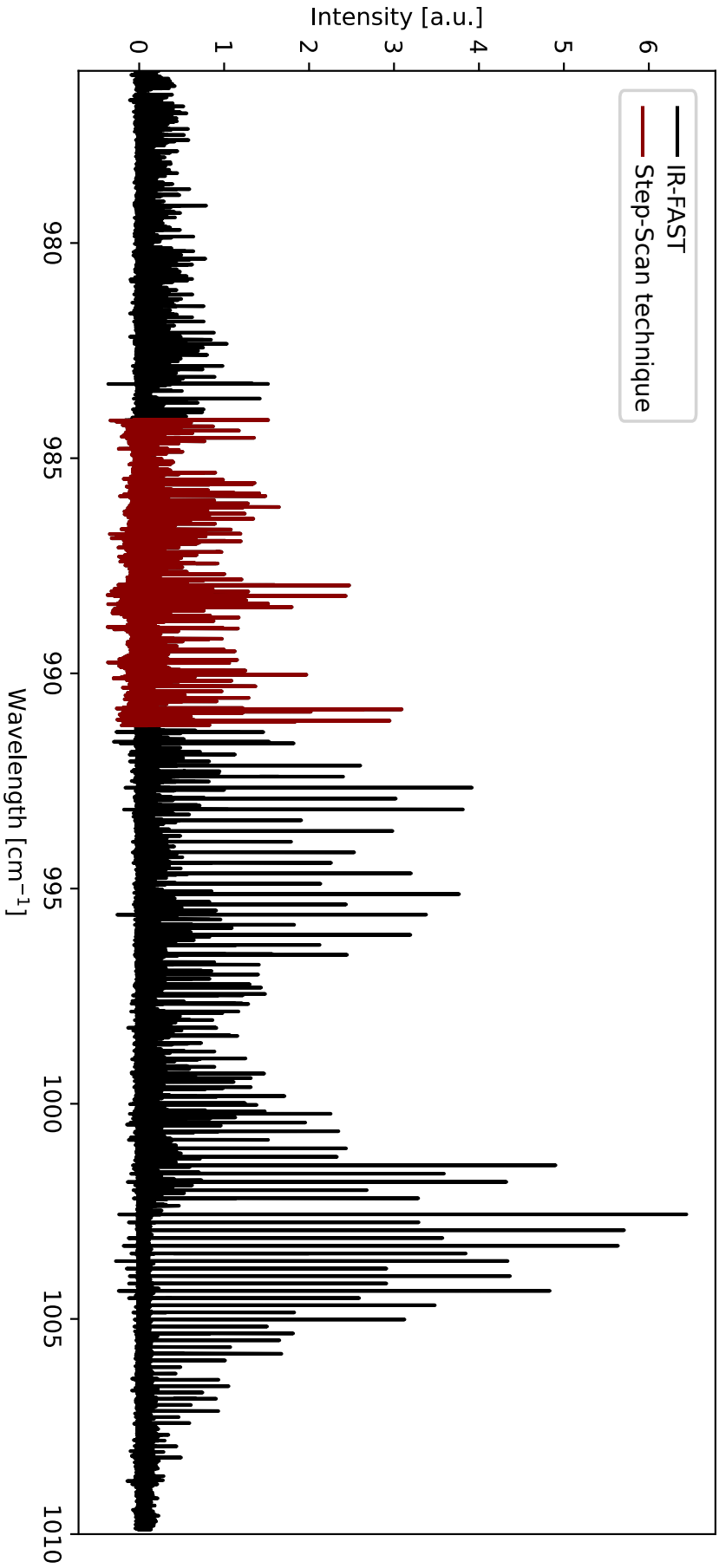

Figure 4.2: The measured Al_2O spectrum from 976.5 cm^{-1} to 1010 cm^{-1}. In black the spectrum measured with an ec-QCL (IR-FAST) is shown. In red the spectrum obtained with the DFB-QCL (step-scan technique) is presented.

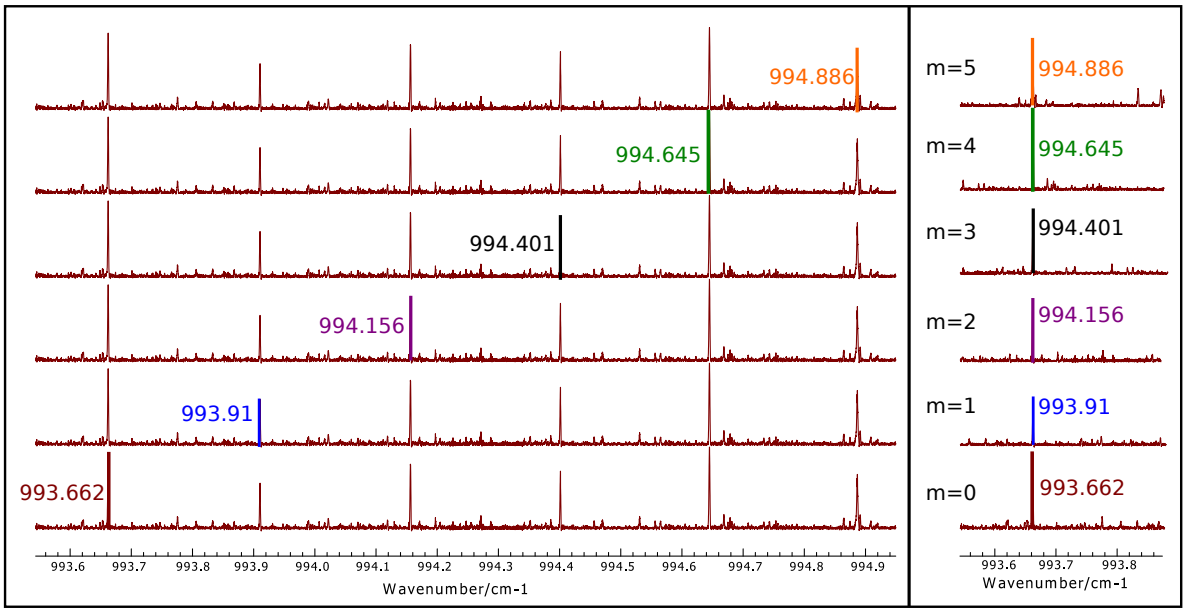

Figure 4.3: 'LoomisWood Plot' of the measured spectrum. The transitions from $P(16)$ to $P(21)$ of the vibrational band $(00^01) \leftarrow (00^00)$ are plotted with the following Fit parameters: $b = 0.2469(1)$ and $d = -0.0007(1)$. All values are given in cm^{-1}. Left: The measured spectrum plotted several times on top of each other. Right: Transitions within a vibrational band above each other, shifted horizontally by an amount, given by a function in the form of the running plot number m.

in the form of the running plot number m. The default polynomial in this case is :

$$b \cdot (m - m_{\text{lowest}}) + d \cdot (m - m_{\text{lowest}})^2. \tag{4.1}$$

If the peaks are correctly assigned, transitions within a vibrational band appear one above each other.

With the 'LoomisWood Plot' function seven different vibrational bands are associated to the molecule Al_2O. Figure 4.4 shows the measured vibrational transitions.

Figure 4.4 clearly reveals that only vibrational transitions including the antisymmetric stretching vibration of $\Delta\nu_3 = 1$ are observed. The reason only these vibrational transitions are visible in the spectra is due to the change of the dipole moment. Only transitions with a transition dipole moment unequal to zero are infrared active. Thus, the symmetric $\Delta\nu_1 = 1$ transition could not be observed.

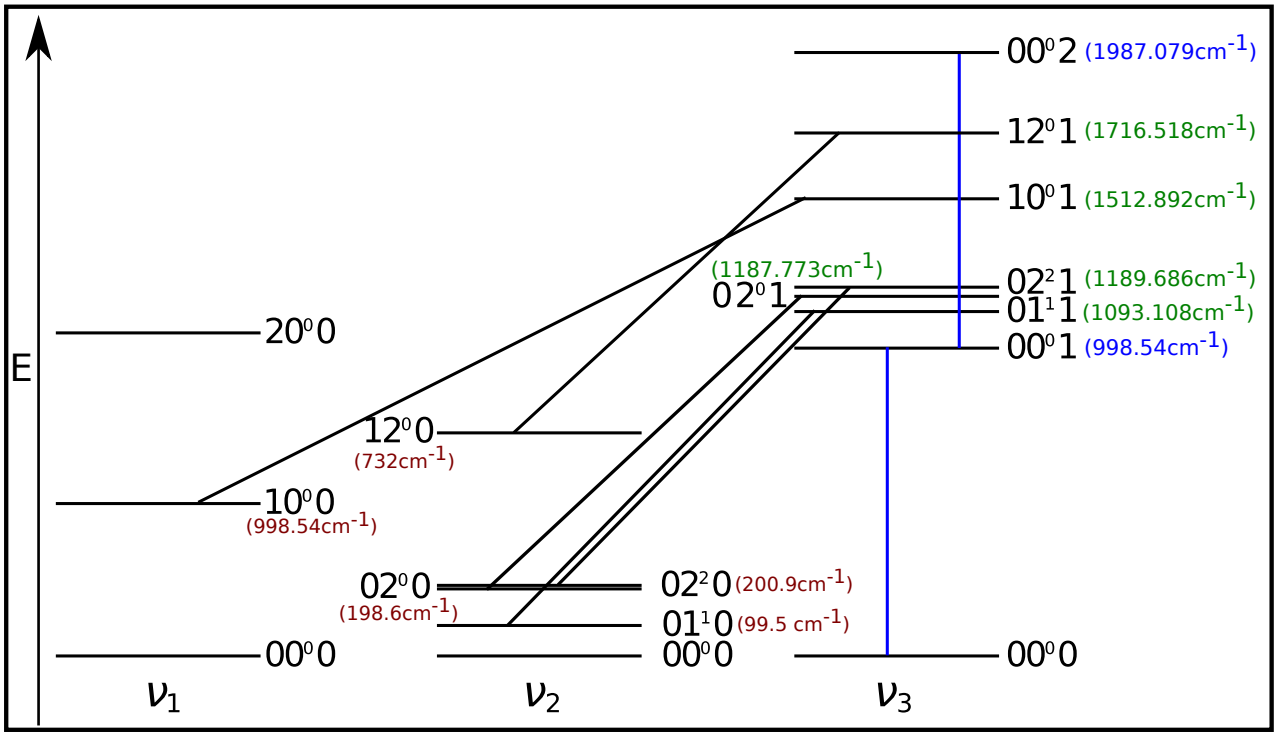

Figure 4.4: Schematic representation of the Al_2O term scheme. The three normal modes of the molecule are shown, where the ν_2 mode is doubly degenerated. Additionally, the transitions are drawn which are assigned in this work. Blue: Experimentally obtained vibrational energy levels. Green: Obtained energy level are based on the theoretical work of Koput and Gertych[26]. Red: Energy levels correspond to the calculated values of Koput and Gertych[26].

4.1.1 The Fundamental Band

The first assigned vibrational band belongs to the transition from the ground state to the first excited ν_3 state, $(00^01) \leftarrow (00^00)$. A total of 130 rotational transitions are assigned to this band. These are separated in, 62 transitions corresponding to P-branch transitions and 68 transitions corresponding to R-branch transitions. Information about the ground state (00^00) and the excited state (00^01) are obtained due to combination difference analysis by a fit of the rotational transitions. From the fit a rotational constant of $B = 0.1085977(9)\,\mathrm{cm}^{-1}$ is obtained. The centrifugal distortion constant D is also determined, due to the large number of observed rotational transitions. The fitted values of $D(00^00)$ results in $2.287(16)10^{-8}\,\mathrm{cm}^{-1}$. The band origin of the ν_3 fundamental band is located at $998.54729(7)\,\mathrm{cm}^{-1}$. The fit results to the rotational constant $B(00^01)$ values of $0.1078237(9)\,\mathrm{cm}^{-1}$ and also to the centrifugal distortion constant $D(00^01)$ with a value of $2.324(16) \cdot 10^{-8}\,\mathrm{cm}^{-1}$. The average error of the fit is $4 \cdot 10^{-4}\,\mathrm{cm}^{-1}$.

Figure 4.5 represents a comparison of the simulation of the transition $(00^01) \leftarrow (00^00)$ in gray and the observed data in black. It is noticeable in Figure 4.5, that the peak intensities of the measured spectrum deviate from the intensities of the simulation. The deviating peak intensities are caused by the production conditions. Since the production of the molecules in the jet is not constant, the peak intensities fluctuate strongly. This intensity fluctuation is provided because the surface of the laser ablation is not flawless, thus molecular yields vary from shot to shot.

The alternating intensity fluctuations that are observable both in the spectrum and also in the simulation (see Figure 4.6) are traced back to the spin statistics of the Al_2O molecule. As already mentioned in the Chapter 2.2.3, the 5/2 spin of the two identical aluminum atoms in the molecule Al_2O result in a spin statistical ratio of 7/5. Figure 4.6 shows a zoom into the spectrum around $1004\,\mathrm{cm}^{-1}$, which clearly reveals how the spin statistics affect the line intensities in the spectrum.

The assigned rotational transitions within this vibrational band, are evaluated by a Boltzmann plot analyses according to Equation 2.29.

The relative population of the energy levels is determined by the measured line intensities, the statistical spin weights and the degeneration. Thus, it is possible to plot the relative population against the lower state energy. A linear regression is performed

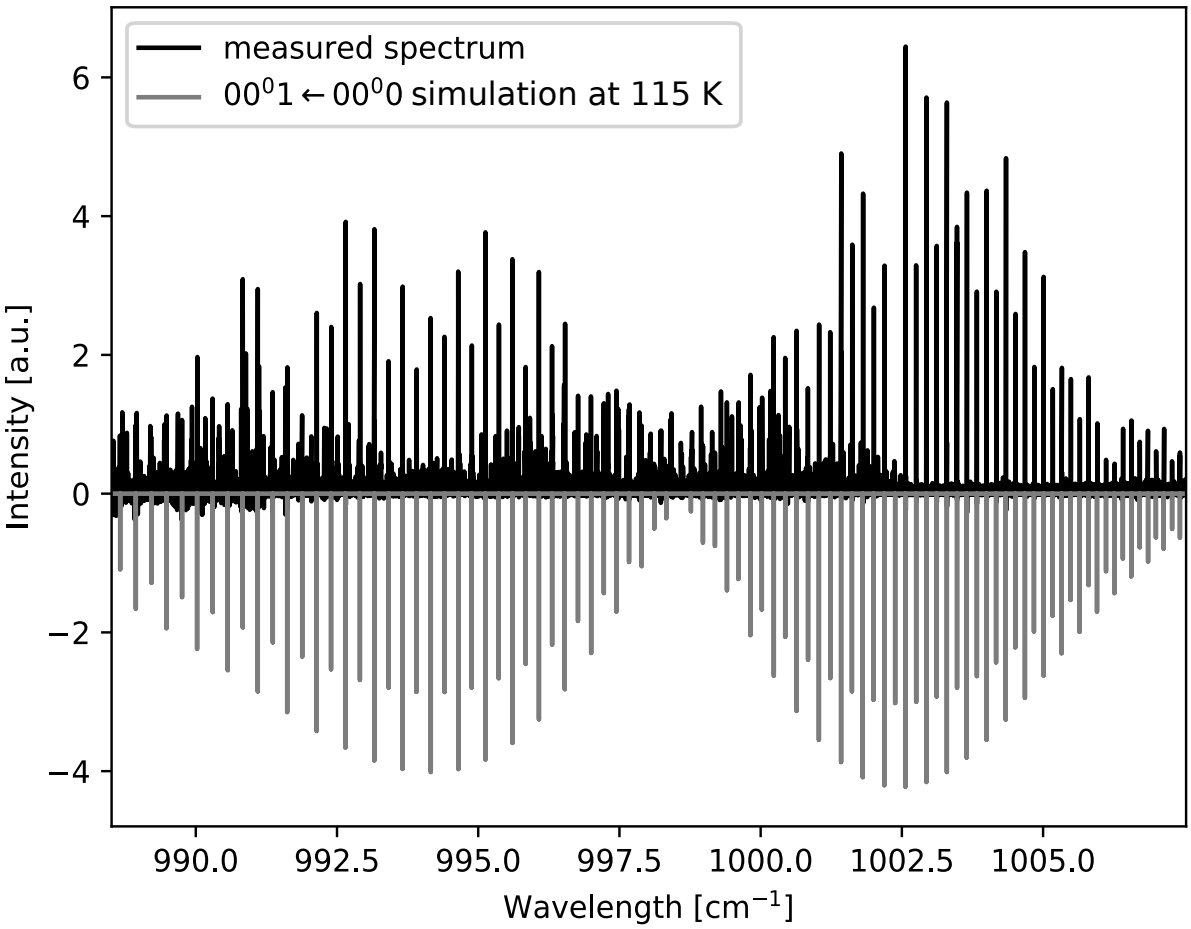

Figure 4.5: Comparison of the rotational resolved vibrational band $(00^01) \leftarrow (00^00)$ and the simulated spectrum. The measured spectrum is shown in black. In gray the transition $(00^01) \leftarrow (00^00)$ at 115 K is simulated.

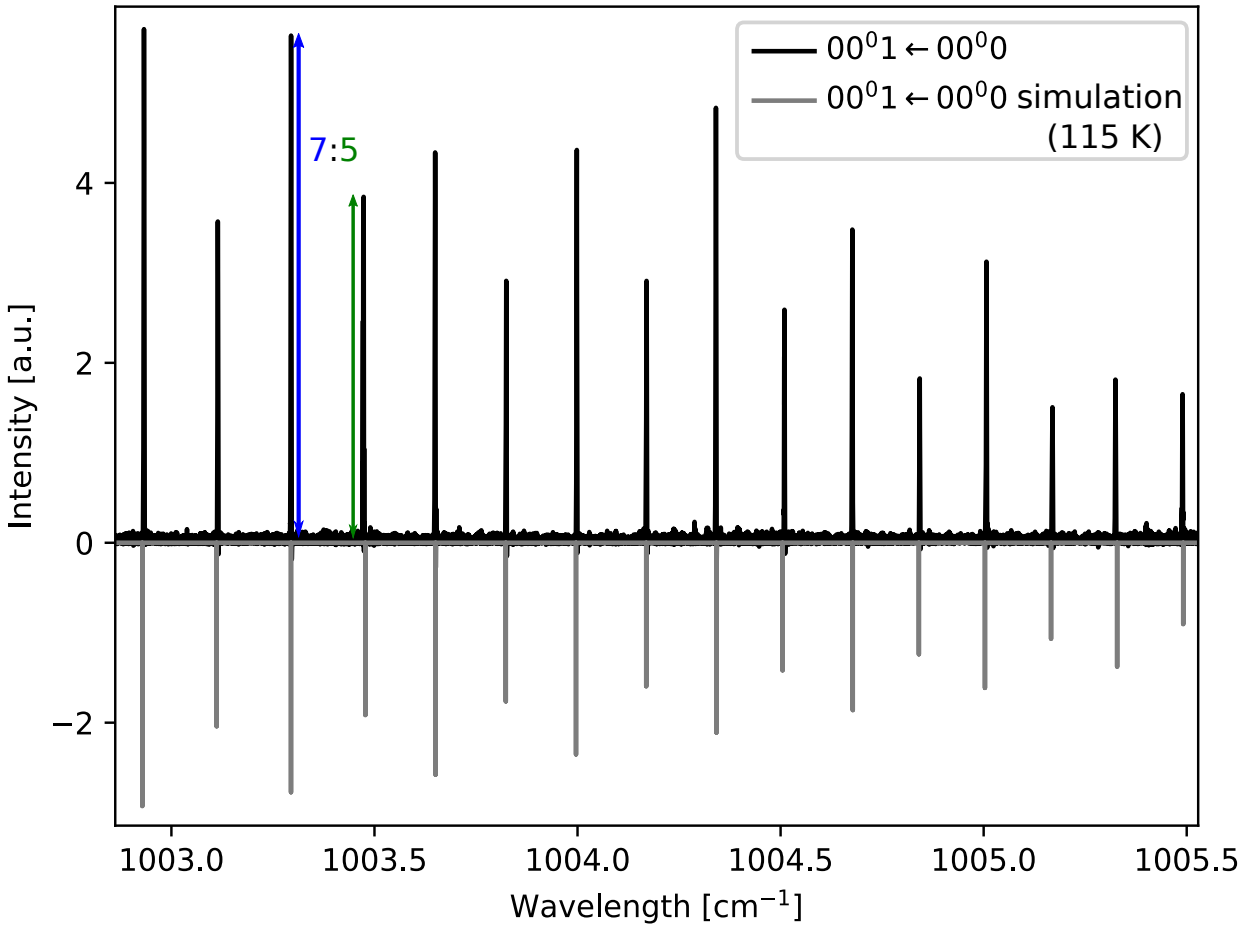

Figure 4.6: This figure shows the Al_2O spectrum in a frequency range of 2.5 cm^{-1}. The measured spectrum is shown in black and the simulated spectrum in gray. An alternating line intensity is clearly seen, which is due to the spin statistics in the ratio 7/5 of the Al_2O molecule.

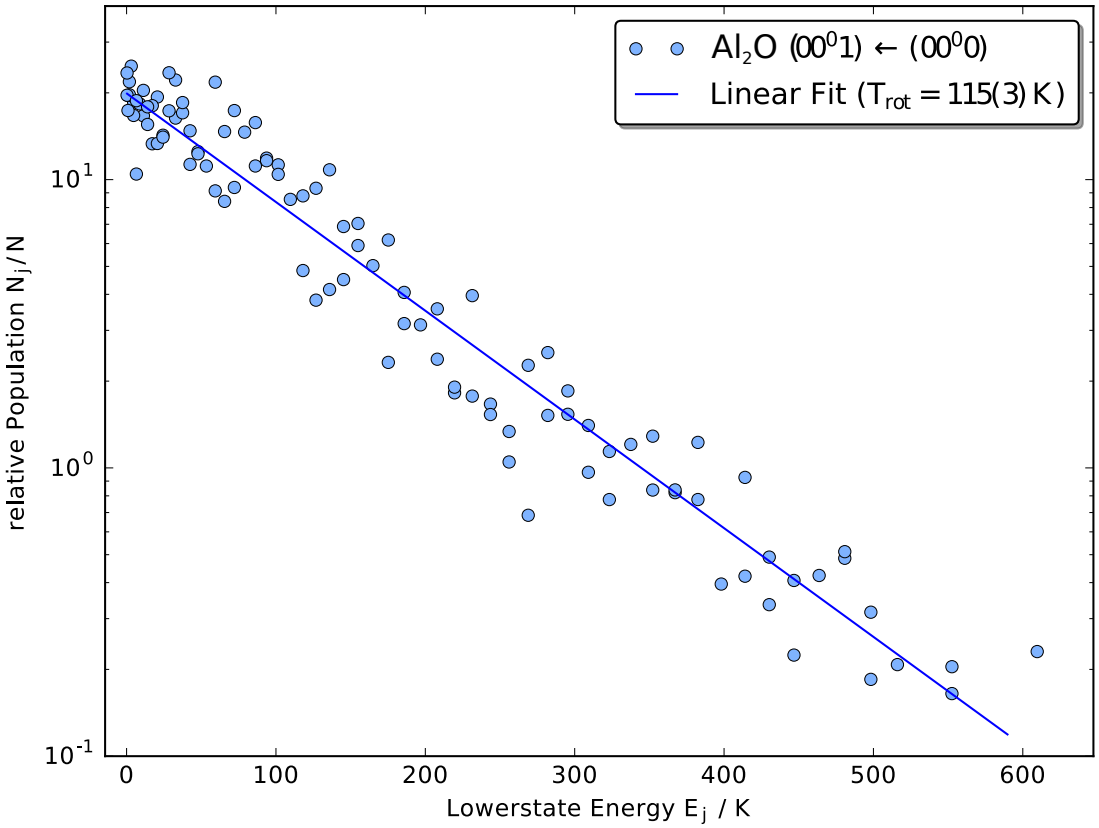

Figure 4.7: Boltzmann plot analysis of the vibrational band $(00^01) \leftarrow (00^00)$ of Al_2O. The relative population is plotted against the state energy. A linear regression is shown in blue, which was fitted to the data. From the slope of the fit a rotational temperature of 115(3) K is obtained for this band.

and results in a rotational temperature of 115(3) K for the transition $(00^01) \leftarrow (00^00)$. Figure 4.7 shows the Boltzmann plot analysis, each blue point represents a transition within the vibrational band $(00^01) \leftarrow (00^00)$.

Each line from the observed spectrum has a certain line width. Figure 4.8 clearly reveals this line broadening.

An average line width (FWHM, full width of half maximum) of $0.0016(2)\,\mathrm{cm}^{-1}$ is determined by fitting a Gauss function with the program 'Pgopher' to different lines. This line width is comparable to a theoretically expected value.

The dominant effect of line broadening is due to Doppler broadening (Equation 3.2) and the geometric Doppler effect (Equation 3.3). The expected line width is based on the temperature determined by the Boltzmann plot analysis. In the following, the line width is obtained as an example for the peak R(7) of $(00^01) \leftarrow (00^00)$ at a frequency

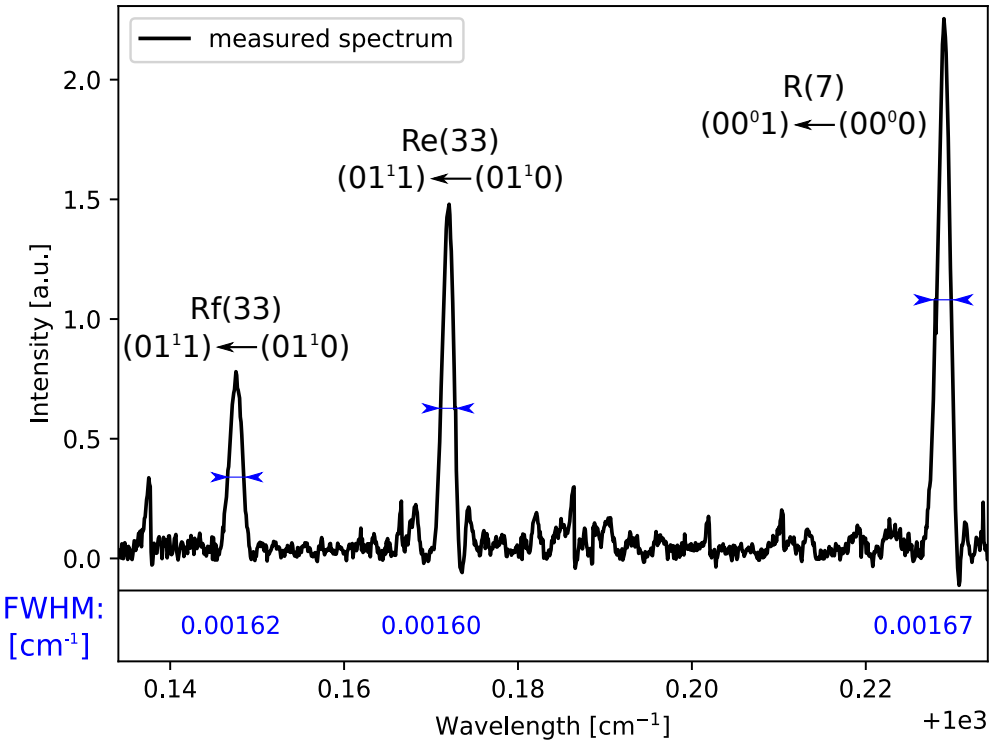

Figure 4.8: Zoom in of the measured Al_2O spectrum in a frequency range of 1000.12 to 1000.24 cm^{-1}. A certain line broadening is clearly visible. The FWHM, which was determined by a Gauss fit of the program 'Pgopher', is given for each of the three lines shown.

of 1000.229 cm^{-1} (see Figure 4.8, right peak):

$$\begin{aligned}\Delta\nu_D &= 1000.229\,\mathrm{cm}^{-1} \cdot \left(\sqrt{\frac{(c + 1666\,\frac{\mathrm{m}}{\mathrm{s}} \cdot \sin(4°))}{(c - 1666\,\frac{\mathrm{m}}{\mathrm{s}} \cdot \sin(4°))}} - 1 \right) \\ &\quad + 7.1 \cdot 10^{-7} \cdot 1000.229\,\mathrm{cm}^{-1} \cdot \sqrt{\frac{115}{69.961}} \\ &= 0.00169(6)\,\mathrm{cm}^{-1}.\end{aligned} \tag{4.2}$$

The determined fitted line width of 0.0016(2) cm^{-1} based on the measured spectrum agrees well with the theoretically expected value of 0.00169(6) cm^{-1}. This agreement of theoretically expected and experimentally observed is also found for all other fitted lines.

Table 4.1: Total number of lines assigned to the respective vibrational bands. Also, the number of lines assigned to the respective P, Q and R branches is given.

	P	Q	R	Sum
$(00^0 1) \leftarrow (00^0 0)$	62	0	68	130
$(00^0 2) \leftarrow (10^0 1)$	43	0	44	87
$(10^0 1) \leftarrow (10^0 0)$	50	0	47	97
$(01^1 1) \leftarrow (01^1 0)$	114	6	119	239
$(02^0 1) \leftarrow (02^0 0)$	43	0	54	97
$(02^2 1) \leftarrow (02^2 0)$	75	16	75	166
$(12^0 1) \leftarrow (12^0 0)^a$	24	0	34	58

[a] Tentatively assigned.

4.1.2 Assigned Vibrational Bands

In addition to the vibrational band of the $(00^0 1) \leftarrow (00^0 0)$ transition, six vibrational bands of the Al_2O molecule are assigned, which are shown in Figure 4.4. From the first excited state $(00^0 1)$, to the next higher state, the transition hot band $(00^0 2) \leftarrow (00^0 1)$ is observed. Also from the first excited state of the ν_1 mode $(10^0 0)$ transitions into the $(10^0 1)$ energy level are assigned. Three transitions took place from the ν_2^l mode to the vibrational band with the first excited state of the ν_3 mode: $(01^1 0) \leftarrow (01^1 1)$, $(02^0 0) \leftarrow (02^0 1)$, $(02^2 0) \leftarrow (02^2 1)$. Also a vibrational band between state $(12^0 0)$ and state $(12^0 1)$ is tentatively assigned.

Table 4.1 gives an overview of the assigned number of lines to the P, Q and R branches of the respective vibrational bands. A total of 874 rotational lines were assigned to the mentioned vibrational bands. Nevertheless, further lines remain in the spectrum which are not yet assigned to any vibrational band. These lines may belong to vibrational bands of the Al_2O molecule, but maybe they also originate from other molecules that have transitions in this particularly frequency range and have been produced by the laser ablation process.

Only the two vibrational energy level $(00^0 1)$ and $(00^0 2)$ are obtained completely experimentally. All further obtained vibrational energy level information are based on the theoretical work of Koput and Gertych[26].

In Figure 4.9 a closer look of the measured spectrum with lines from six assigned bands is shown. The transitions were marked in color and assigned to their vibrational

Table 4.2: Frequencies ν of the identified vibrational levels with associated vibrational constant B and the corresponding centrifugal distortion constant D.

	ν [cm^{-1}]	B [cm^{-1}]	$D \cdot 10^{-8}$ [cm^{-1}]
(00^00)	0	0.1085977(9)	2.287(16)
(10^00)	520.7 [a]	0.1082718(16)	2.27(4)
(01^10)	99.5 [a]	0.1093987(8)	2.720(17)
(02^00)	198.6 [a]	0.1094192(30)	2.93(13)
(02^20)	200.9 [a]	0.1101733(18)	2.96(7)
(12^00)	732 [a]	0.1095618(32)	1.92(19)
(00^01)	998.54729(7)	0.1094192(30)	2.324(16)
(00^02)	1987.07944(11)	0.1070606(9)	2.403(19)
(10^01)	1512.89158(8)	0.1074927(17)	2.31(4)
(01^11)	1093.10751(5)	0.1086574(7)	2.804(16)
(02^01)	1187.77342(9)	0.1087056(31)	3.24(13)
(02^21)	1189.68636(6)	0.1094605(18)	3.02(8)
(12^01)	1716.51760(10)	0.1088775(31)	2.01(17)

[a] These values were not determined experimentally and correspond to the calculated values of Koput and Gertych.[26]

bands. The assignment $(12^01) \leftarrow (12^00)$ needed to handle with caution, because for example the energetically lower vibrational band between state (11^11) and state (11^10) is not observed, although it should be populated. It is possible that the transitions of the $(11^11) \leftarrow (11^10)$ band are hidden in the not yet assigned peaks of the spectrum. Since no other pattern of a linear molecule is found in the unassigned transitions, this suggests that this transition is disturbed by other states.

Table 4.2 summarizes the parameters obtained by a fit to the rotational transitions of the individual vibrational bands. These include the band origin ν, the rotational constant B and the centrifugal distortion constant D.

Since different rotational temperatures may be present for each vibrational band, a Boltzmann plot analysis for further vibrational bands were performed similar as for the fundamental ν_3 band (see Figure 4.7). For the vibrational band $(00^02) \leftarrow (00^01)$ a rotational temperature of 107(9) K is determined. For the vibrational band $(01^11) \leftarrow (01^10)$ a rotational temperature of 135(4) K is obtained. Due to noise and low line intensities, no Boltzmann plot analysis is performed for all other vibrational bands and therefore no temperature could be determined for them. Altogether an average rotational temperature of 119(12) K can be assumed by the three determined temperature values.

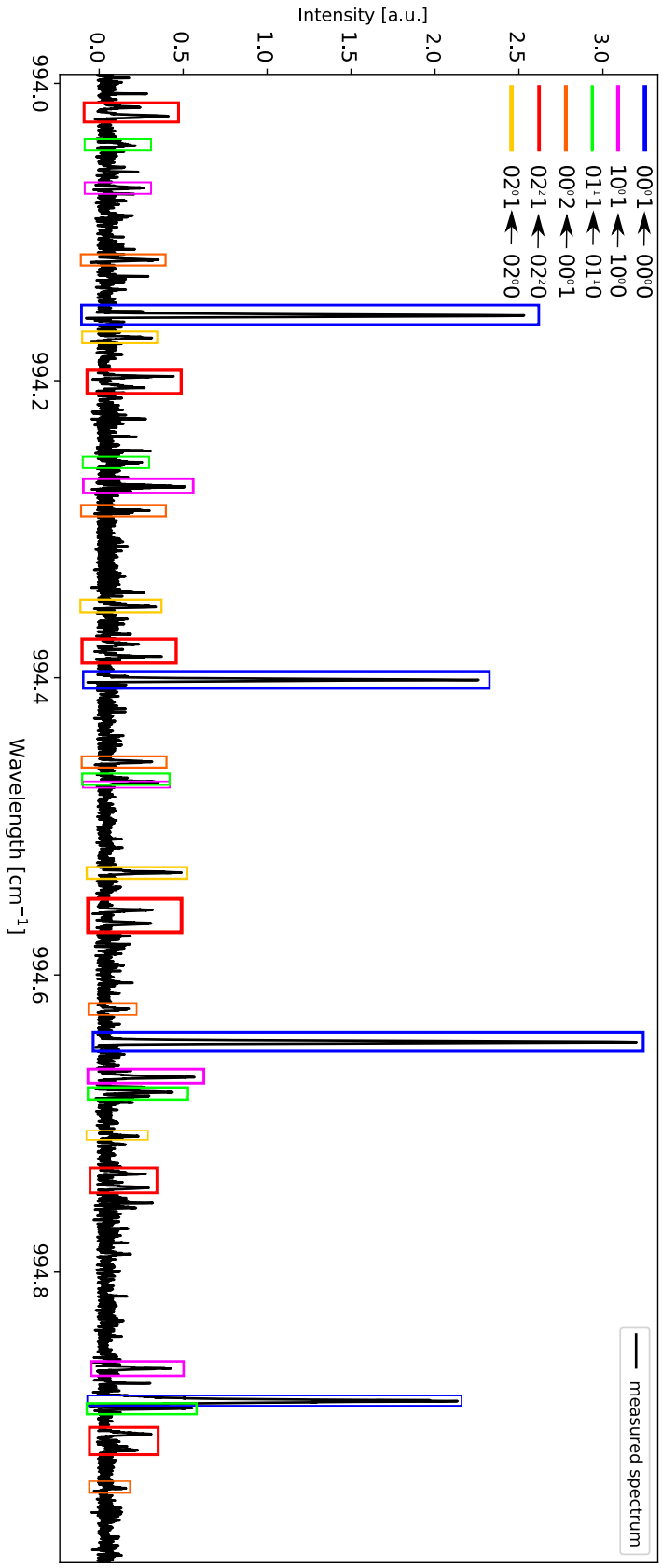

Figure 4.9: Closer look of the Al_2O spectrum in a frequency range from 994.0 cm^{-1} to 995.0 cm^{-1}. Rotational transitions of six of the seven associated vibrational bands are shown in this range and are color-coded. The seventh vibrational band $(12^{0}1) \leftarrow (12^{0}0)$ is due to the low line intensity of the rotational transitions not recognizable in this frequency range.

For the previously determined line broadening a temperature of 115(3) K was used. Applying the determined average temperature of 119(12) K does not result in a significant difference for the line width, whereby the theoretical expected line width still corresponds well with the experimental values.

Interestingly the rotational temperature in the jet in this experiment is significantly higher than the typical temperatures between 20 K and 40 K reached in similar experiments[40,46]. One reason for this may be the donor gas, which contains the buffer gas. In the work of Barners *et al.*[47] it could be shown that the rotational temperatures of the molecules with pure oxygen (O_2) in the buffer gas are about 50 K. If N_2O was used as donor gas, the authors determined a rotational temperatures of 90 K. In this experiment N_2O was also used, so that the determined temperatures seem to be reasonable.

4.2 Equilibrium Structure of the Al_2O Molecule and Vibrational Analysis

By assigning the ro-vibrational transitions, it is now possible to perform a rotational analysis. To solve the equation system needed for the rotational analysis, five different vibrational levels are required.

First the experimental equilibrium rotational structure B_e is calculated. The vibrational levels B_{00^00}, B_{00^01}, B_{10^00} and B_{02^00} (see Table 4.2) are used in Equation 2.13. By solving the equation system, α_1, α_2 and α_3 are calculated. In the following the calculation for α_2 is shown as an example:

$$B_{00^00} = B_e - \frac{\alpha_1}{2} - \alpha_2 - \frac{\alpha_3}{2}, \tag{4.3}$$

$$B_{02^00} = B_e - \frac{\alpha_1}{2} - 3\alpha_2 - \frac{\alpha_3}{2}. \tag{4.4}$$

If Equation 4.3 is now subtracted from Equation 4.4 and divided by two, α_2 is obtained:

$$(B_{00^00} - B_{02^00})/2 = \alpha_2. \tag{4.5}$$

α_1 and α_3 are calculated analogously.

By inserting B_{00^00} into Equation 2.13 and converting to B_e, the equilibrium rotational constant B_e of Al_2O can be determined as follows:

$$\begin{aligned} B_e &= B_{00^00} + \frac{\alpha_1}{2} + \alpha_2 + \frac{\alpha_3}{2} \\ &= B_{00^00} + \frac{(B_{00^00} - B_{10^00})}{2} + \frac{(B_{00^00} - B_{02^00})}{2} + \frac{(B_{00^00} - B_{00^01})}{2} \\ &= 0.1087369(29)\,\mathrm{cm}^{-1}. \end{aligned}$$

To calculate the rotational l-type shift γ_l, that is present in Equation 2.13, two vibrational levels are required, that depend on 'l'. In this case the vibrational levels B_{02^00} and B_{02^20} are selected. The calculation of γ_l is shown in the following example:

$$\begin{aligned} \gamma_l 2^2 = B_{02^20} - B_{02^00} \Longleftrightarrow\ & \gamma_l = B_{02^20} - B_{02^00}/4 \\ & \gamma_l = 0.0001885(9)\,\mathrm{cm}^{-1}. \end{aligned}$$

By using the moment of inertia I, which is determined as follows:

$$I_e = \frac{h^2}{8 \cdot \pi^2 \cdot B_e} = 2.57436(7) \cdot 10^{-45}\,\mathrm{kg\,m}^2, \tag{4.6}$$

the equilibrium bond length r_e of the molecule is calculated by converting Equation 2.5:

$$r_e(\mathrm{AlO}) = \sqrt{\frac{I}{2 \cdot m}} = 1.694388(22)\,\text{Å}. \tag{4.7}$$

This result for $r_e(\mathrm{AlO}) = 1.694388(22)$ Å agrees well with the theoretically calculated equilibrium bond length of Koput and Gertych[26], which predict a bond length of $r_e(\mathrm{AlO}) = 1.707$ Å. This results in a deviation for r_e in the order of sup percent between the values calculated here and the values calculated by Koput and Gertych.

Additionally to the equilibrium rotational constant B_e, the equilibrium centrifugal distortion constant D_e can also be calculated analogously. The centrifugal distortion values of the vibrational levels are used, which were taken into account as in the calculation of B_e (D_{00^00}, D_{00^01}, D_{10^00} and D_{02^00}). By inserting D_{00^00} into Equation 2.14 and converting to D_e, the following result can be calculated for the equilibrium

Table 4.3: Calculated values of the rotational analysis. The equilibrium rotational constant B_e, as well as the specific interaction constants α_i and β_i and the equilibrium centrifugal distortion constant D_e are summarized. Additionally, the moment of inertia I, the equilibrium distance r_e and the l-type shift are shown.

	experiment
B_e /cm^{-1}	0.1087369(29)
α_1 /cm^{-1}	0.0003259(19)
α_2 /cm^{-1}	−0.0004107(16)
α_3 /cm^{-1}	0.0007740(13)
$D_e \cdot 10^8$ /cm^{-1}	1.94(6)
$\beta_1 \cdot 10^{10}$ /cm^{-1}	1(5)
$\beta_2 \cdot 10^{10}$ /cm^{-1}	−34(4)
$\beta_3 \cdot 10^{10}$ /cm^{-1}	−3.8(2.3)
$I \cdot 10^{45}$ /kg m^2	2.57436(7)
r_e /Å	1.694388(22)
γ_l /cm^{-1}	0.0001885(9)

centrifugal distortion constant D_e of the Al_2O molecule:

$$D_e = D_{00^00} + \frac{\beta_1}{2} + \beta_2 + \frac{\beta_3}{2} \tag{4.8}$$

$$= 1.94(6) \cdot 10^{-8}\,\mathrm{cm}^{-1}. \tag{4.9}$$

Table 4.3 summarizes the calculated results of the rotational analysis.

In the next step a vibrational analysis is performed. Ten different vibrational levels are required to calculate the ω_i and χ_i occurring in Equation 2.12. The following vibrational energy levels were used to perform the vibrational analysis: (00^01), (00^02), (01^11), (02^00), (02^01), (02^21), (12^01), (10^00), (10^01) and (20^00). Here it is to mentioned, that only the energy levels (00^01) and (00^02) are fully experimental determined. The other vibrational levels are based on theoretical values from the work of Koput and Gertych[26].

As previously the α_i are obtained by solving a system of equations in the rotational analysis, the ω_i and χ_i are obtained by solving a system of equations. The vibrational l-type shift g can also be calculated analogously to the rotational l-type shiftγ_l.

The equation system established for vibrational analysis corresponds to the following

form:

$$\begin{aligned} E_{\text{vib}}(v_1, v_2^l, v_3) = & \begin{pmatrix} \omega_1 \\ \omega_2 \\ \omega_3 \end{pmatrix} \cdot \begin{pmatrix} v_1 + \frac{1}{2} \\ v_2 + 1 \\ v_3 + \frac{1}{2} \end{pmatrix}^{\mathrm{T}} \\ & + \begin{pmatrix} \chi_{11} & \chi_{12} & \chi_{13} \\ 0 & \chi_{22} & \chi_{23} \\ 0 & 0 & \chi_{33} \end{pmatrix} \cdot \begin{pmatrix} v_1 + \frac{1}{2} \\ v_2 + 1 \\ v_3 + \frac{1}{2} \end{pmatrix} \cdot \begin{pmatrix} v_1 + \frac{1}{2} \\ v_2 + 1 \\ v_3 + \frac{1}{2} \end{pmatrix}^{\mathrm{T}} + gl^2. \end{aligned} \tag{4.10}$$

By using two different energy levels e.g. (00^00) and (00^01), which are subtracted from each other, the transition frequency results as follows:

$$\nu_{(00^01)} = E_{\text{vib}}(0, 0^0, 1) - E_{\text{vib}}(0, 0^0, 0) = \omega_3 + \frac{\chi_{13}}{2} + \chi_{23} + 2\chi_{33}. \tag{4.11}$$

If this step is repeated with a further energy level, e.g. (00^02) a further transition frequency results:

$$\nu_{(00^02)} = E_{\text{vib}}(0, 0^0, 2) - E_{\text{vib}}(0, 0^0, 0) = 2\omega_3 + \chi_{13} + 2\chi_{23} + 6\chi_{33}. \tag{4.12}$$

If the two obtained transition frequencies $\nu_{(00^02)}$ and $\nu_{(00^01)}$ are subtracted from each other, χ_{33} is determined:

$$\begin{aligned} \nu_{(00^02)} - 2 \cdot \nu_{(00^01)} &= 2\chi_{33} \\ \chi_{33} &= -5.00757(9)\,\mathrm{cm}^{-1}. \end{aligned} \tag{4.13}$$

The calculation of ω_i and χ_i is done analogously.

In order to calculate the l-type shift in the vibration, two different transition frequencies from the ν_2^l mode are required, as in rotational case. If these are subtracted from each other and divided by l^2, the result is $g = 0.48(14)\,\mathrm{cm}^{-1}$.

The zero-point energy is also calculated by inserting the calculated ω_i and χ_{is} in Equation 4.10:

Table 4.4: Calculated values of the vibrational analysis in comparison to the theoretically calculated values of Koput and Gertych[26] and the deviation between theoretical and experimental values. The harmonic frequencies ω_i, the anharmonic corrections χ_{is}, as well as the l-type shift g and the zero point energy ZPE were determined.

	experiment [cm^{-1}]	theory[26] [cm^{-1}]	deviation [%]
ω_1	519.1(3)	519.4	0.06
ω_2	96(2)	96.8	0.83
ω_3	1016.4(3)	1016.1	0.03
χ_{11}	−1.20(8)	−1.0	17
χ_{22}	0.5(4)	0.4	20
χ_{33}	−5.00757(9)	−4.90	2.14
χ_{12}	7.2(3)	6.4	11
χ_{13}	−6.4(4)	−6.2	3
χ_{23}	−4.7(2)	−4.8	2
g	0.48(14)	0.5	4
ZPE	862.9(1.3)	863	0.01

$$
\begin{aligned}
E_{\mathrm{vib}}(0,0^0,0)/\mathrm{cm}^{-1} = &\begin{pmatrix} 519.1(3) \\ 96(2) \\ 1016.4(3) \end{pmatrix} \cdot \begin{pmatrix} 0+\frac{1}{2} \\ 0+1 \\ 0+\frac{1}{2} \end{pmatrix}^{\mathrm{T}} \\
&+ \begin{pmatrix} -1.20(8) & 7.2(3) & -6.4(4) \\ 0 & 0.5(4) & -4.7(2) \\ 0 & 0 & -5.00757(9) \end{pmatrix} \\
&\cdot \begin{pmatrix} 0+\frac{1}{2} \\ 0+1 \\ 0+\frac{1}{2} \end{pmatrix} \cdot \begin{pmatrix} 0+\frac{1}{2} \\ 0+1 \\ 0+\frac{1}{2} \end{pmatrix}^{\mathrm{T}} = 862.9(1.3).
\end{aligned} \tag{4.14}
$$

Table 4.4 summarizes all the results obtained by the vibrational analysis and compares them with the theoretically calculated values of Koput and Gertych[26]. It is clearly seen that there is also a good agreement between the experimentally obtained values and the theoretically calculated values.

The rotational analysis and vibrational analysis enables to show that the assignment of the vibrational band $(12^01) \leftarrow (12^00)$ is reasonable. By comparing the rotational

Table 4.5: Calculated rotational constants of $B(12^00)$ and $B(12^01)$ in comparison to the rotational constants of the 'Pgopher' fit and the deviation between these rotational constants.

	calculated [cm^{-1}]	fit [cm^{-1}]	deviation [%]
$B(12^00)$	0.109093(6)	0.1095618(32)	0.43
$B(12^01)$	0.108319(7)	0.1088775(31)	0.51

constants $B(12^00)$ and $B(12^01)$ from the rotational analysis with the results of the 'Pgopher' fit, it is seen that the values differs less than 0.55 % (see Table 4.5).

The vibrational energy of 984.5176(1) cm^{-1} resulting from the 'Pgopher' fit is also calculated confirmed by using Equation 2.12 with the same error of less than 0.55 %.

4.3 l-type Doubling of the Excited Bending Vibrations

A closer look at the measured spectrum reveals that some rotational transitions are splitted. This is shown in Figure 4.10 by a frequency range of 0.04 cm^{-1}. A line splitting is shown here, which belongs to the vibrational bands $(01^11) \leftarrow (01^10)$ and $(02^21) \leftarrow (02^20)$.

The transitions $(01^11) \leftarrow (01^10)$ are split due to the l-type doubling within degenerated bending vibrational modes (ν_2^l), which posses a vibrational angular momentum. Here, only levels of equal parity (e, f) and equal J influence one another. The energy difference of the splitting is scaled by q_l (see Equation 2.16). To calculate q_l Equation 2.17 is used:

$$q_l = 2\frac{B_e^2}{\omega_2}\left(1 + \frac{4\omega_2^2}{\omega_3^2 - \omega_2^2}\right) = 0.0002529(10)\,cm^{-1}. \tag{4.15}$$

By fitting the vibrational band with 'Pgopher', within the measured spectrum, the values for the l-type doubling constants of $q_l(01^10) = 2.417(7) \cdot 10^{-4}\,cm^{-1}$ and $q_l(01^11) = 2.479(7) \cdot 10^{-4}\,cm^{-1}$ are obtained (see Table 4.6). The two values for q_l that are determined by the fit differ by 2.5% from the calculated value of Equation 4.15. The calculated q_l, with the equilibrium rotational constant B_e and the harmonic frequencies

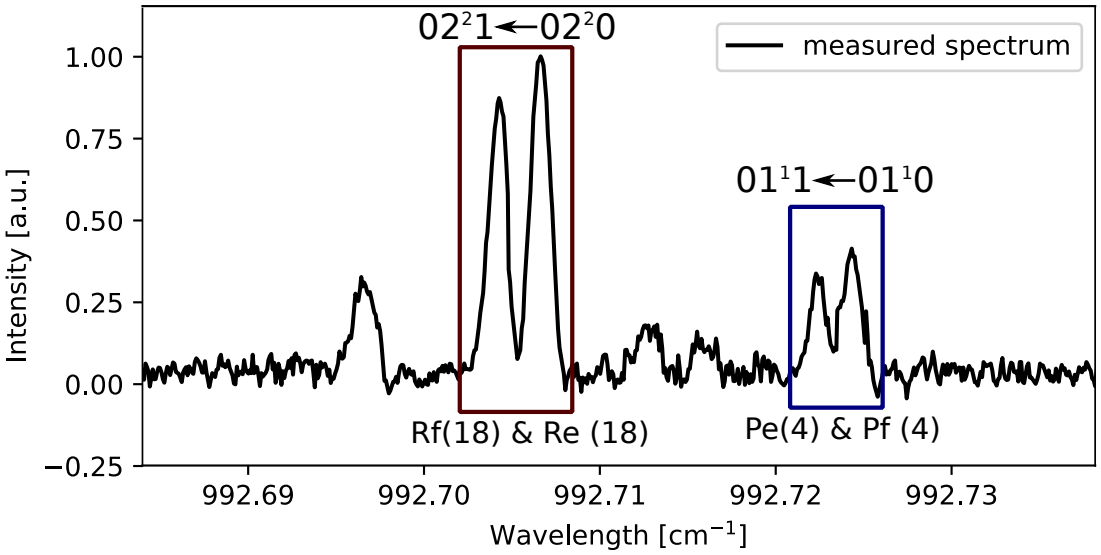

Figure 4.10: Section of the measured Al_2O spectrum where transitions from the degenerated bending vibration mode ν_2^l are shown. The line splitting caused by the vibrational angular momentum is clearly visible. Splittings of the vibrational band $(02^21) \leftarrow (02^20)$ (red) and the vibrational band $(01^11) \leftarrow (01^10)$ (blue) are shown.

ω_2 and ω_3, deviates only 5% from the values of the fit. For the vibrational levels of the second vibrational band $(02^21) \leftarrow (02^20)$ no values for q_l are determined. This is due to the fact that an additional effect is involved here.

The l-type doubling constant q_l of Al_2O can now be compared with l-type doubling constants of molecules that are isovalent to Al_2O. The selected isovalent molecules are CO_2 and C_3. In 1954, France and Dickey[48] were able to determine a value of $q_l = 3.5 \cdot 10^{-4}\,\mathrm{cm}^{-1}$ for the l-type doubling constant from their CO_2 spectrum by means of high resolution prism-grating vacuum spectroscopy. It indicates that it is at least the same order as in case of Al_2O.

The l-type doubling constant of C_3 was determined experimentally by Gausset *et al.*[49] to a value of $q_l = 5.5 \cdot 10^{-3}\,\mathrm{cm}^{-1}$. In 1989 Rohlfing and Goldsmith[50] could confirm this value by measurements of jet-cooled C_3. The q_l of C_3 is thus larger than the q_l of Al_2O by an order of magnitude. This large l-type doubling constant, indicates that C_3 is subject to a strong rotational-vibrational coupling, which is caused by the floppiness of C_3[50].

This comparison shows that Al_2O is significantly more stiff compared to C_3. This also means that the rotational-vibrational coupling is weaker compared to C_3.

Table 4.6: Obtained parameters from 'Pgopher' for the l-type doubling constant of the vibrational levels (01^10) and (01^11) and the perturbation parameters q_t and q_{tJ} of the perturbation between the vibrational levels $(02^2\nu_3)$ for $\nu_3 = 0, 1$. All values are given in cm^{-1}.

l-type doubling:	q_l	perturbation:	q_t	q_{tJ}
(01^10)	$2.417(7) \cdot 10^{-4}$	(02^20) and (02^00)	$4.26(8) \cdot 10^{-4}$	$3.6(4) \cdot 10^{-8}$
(01^11)	$2.479(7) \cdot 10^{-4}$	(02^21) and (02^01)	$-4.34(8) \cdot 10^{-4}$	$-3.4(4) \cdot 10^{-8}$

Table 4.7: Comparison of the derived perturbation parameters q_t and q_{tJ} of Al_2O with the perturbation parameters q_t and q_{tJ} of C_3 and CO_2. All values are given in cm^{-1}.

perturbation:		C_3 [51]	Al_2O	CO_2 [52]
(02^00) and(02^20)	q_t	$8.143(25) \cdot 10^{-3}$	$4.26(8) \cdot 10^{-4}$	$-1.52882(20) \cdot 10^{-4}$
	$q_{t,J}$	$-7.85(19) \cdot 10^{-7}$	$3.6(4) \cdot 10^{-8}$	$1.838(9) \cdot 10^{-10}$
(02^01) and(02^21)	q_t	$9.512(30) \cdot 10^{-3}$	$-4.34(8) \cdot 10^{-4}$	-
	$q_{t,J}$	$-12.00(29) \cdot 10^{-7}$	$-3.4(4) \cdot 10^{-8}$	-

In case of the states $(02^0\nu_3)$ and $(02^2\nu_3)$ for $\nu_3 = 0, 1$ the energy levels are located tight together, so that a perturbation forms between them (see Figure 4.4). This perturbation is described by Equation 2.19. The corresponding fit values for q_t and q_{tJ} are shown in Table 4.6. Since the l-type doubling constants q_l of the vibrational levels (02^20) and (02^21) strongly correlates with q_{tJ}, it is not possible to determine the value for q_l.

In addition to the l-type doubling constant, the perturbation parameters q_t and $q_{t,J}$ between the vibrational levels (02^2v_3) for $v_1 = 0, 1$, are also comparable between C_3, Al_2O and CO_2 (see Table 4.7). It is shown clearly that the perturbation parameter of C_3 ($q_t = 8.143(25) \cdot 10^{-3}\,\mathrm{cm}^{-1}$) is one order of magnitude larger than that of Al_2O and CO_2. In the comparison between Al_2O and CO_2, it is seen that the perturbation parameter of Al_2O ($q_t = 4.26(8) \cdot 10^{-4}\,\mathrm{cm}^{-1}$) is larger than for CO_2 ($q_t = -1.52882(20) \cdot 10^{-4}\,\mathrm{cm}^{-1}$).

This difference in the perturbation parameters can be caused due to nearby energy levels. By comparing the energy levels (02^00) and (02^20) of C_3, Al_2O and CO_2 with and without considering the perturbation between the adjacent energy levels, it is seen that there is a dependency between the energy shift of the energy levels and the perturbation parameter q_t. The larger the energy shift between the energy levels, the

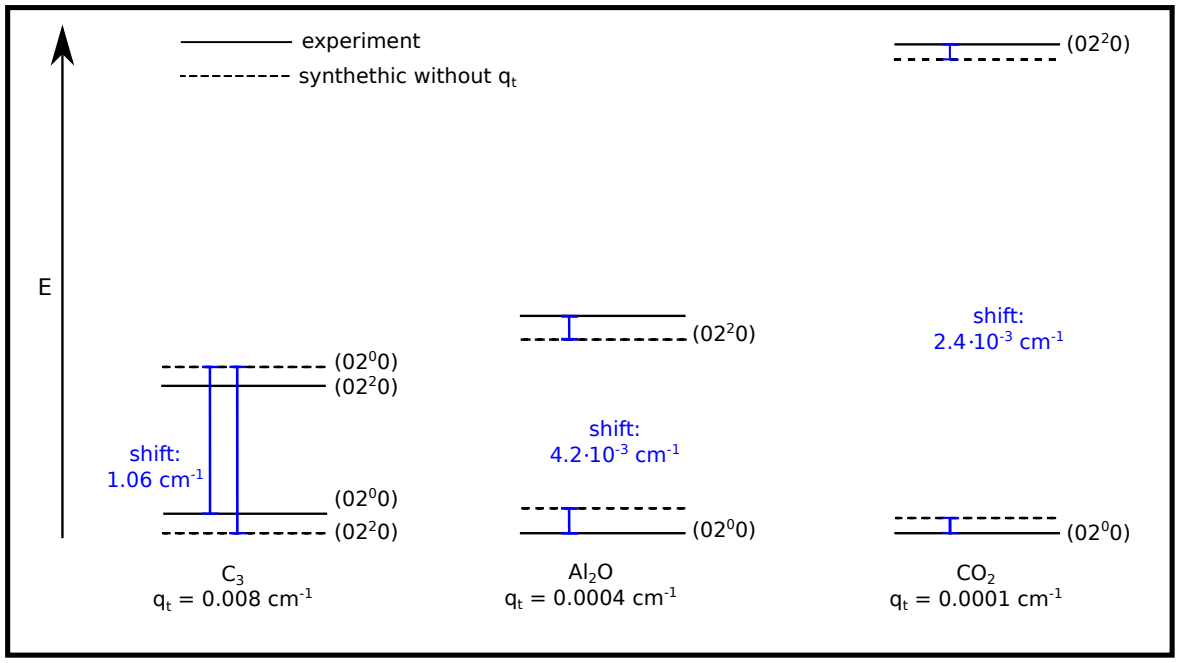

Figure 4.11: Comparison of the vibrational levels (02^20) and (02^00) for $J = 16$ in the molecules C_3, Al_2O and CO_2. The corresponding perturbation parameters q_t are given.

larger is the perturbation parameter q_t, as shown in Figure 4.11.

Comparing simple 1D-potential models by only considering ω_2 and χ_{22}, the perturbation occurring in the ν_2 mode can be qualitatively understood. Therefore, the harmonic potential and the Morse potential of C_3, Al_2O and CO_2 are investigated. The model of the Morse potentials of the three molecules in Figure 4.12 shows that the harmonic part of the potential of C_3 deviates stronger from the Morse potential than in the case of Al_2O and CO_2. A comparison between Al_2O and CO_2 shows that the harmonic part in CO_2 contributes stronger to the potential curve than in Al_2O. This observation is supported by the ratio of χ_{22} and ω_2, where $\frac{\chi_{22}}{\omega_2}|_{Al_2O} > \frac{\chi_{22}}{\omega_2}|_{CO_2}$, see Table 4.8.

These comparisons suggest that in case of a molecule which behaves in a more anharmonic way, leads to closer energy levels in the double degenerated ν_2 mode. Thus, a stronger perturbation between the energy levels occurs. It is also noticeable that the larger the energy shift of the energy levels, the larger the perturbation parameter of the resonance strength. Accordingly, if a molecular potential follows a more harmonic description, the energy levels of the double degenerated ν_2 mode are more separated. This leads to a weaker perturbation between the energy levels and therefore the perturbation parameter is smaller.

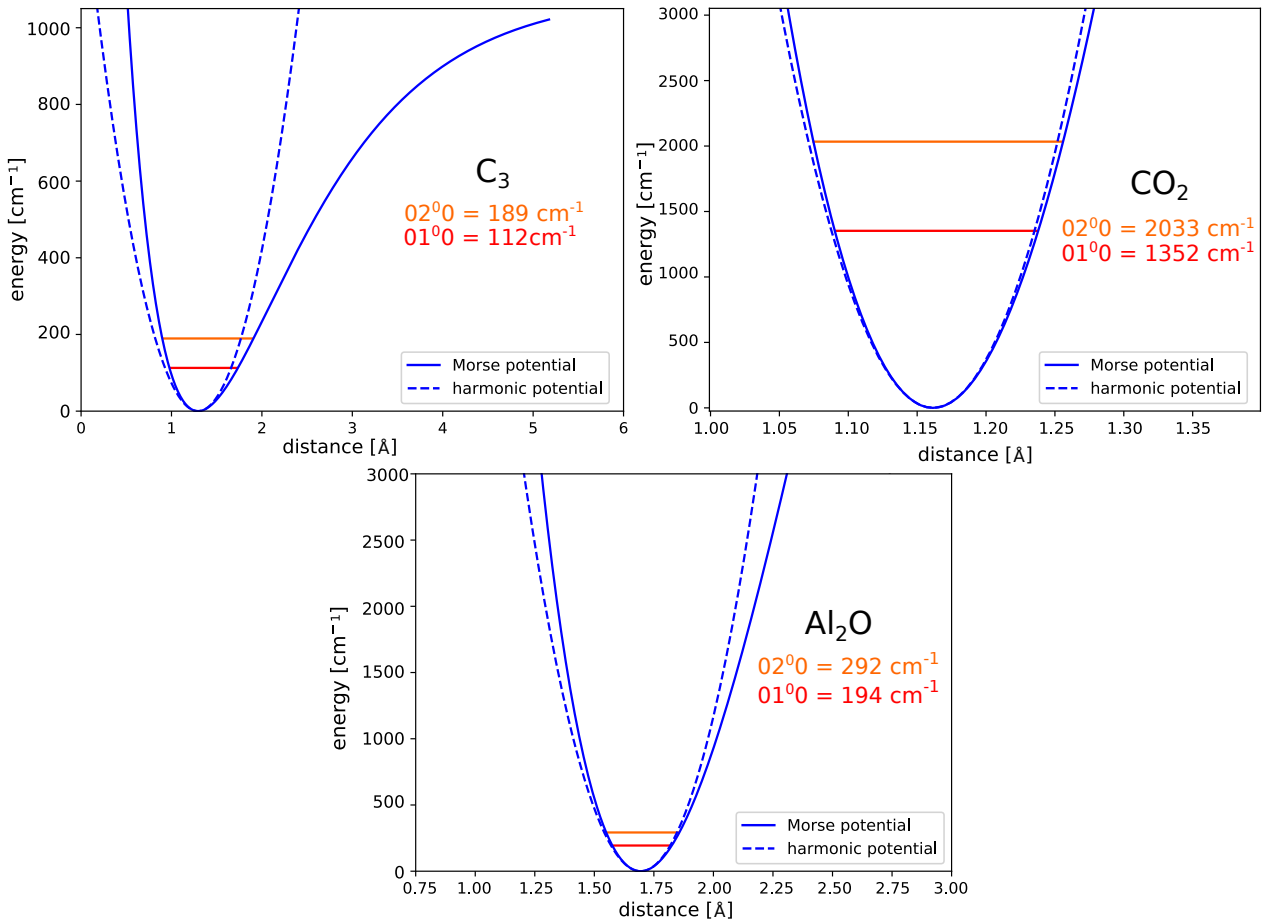

Figure 4.12: Comparative illustration between the Morse potential of C_3, Al_2O and CO_2. In addition, the harmonic potential of the molecules is shown as a dotted line. Energy scale shifted by the corresponding dissociation energy.

Table 4.8: Comparison of molecular parameters of C_3, Al_2O and CO_2. This values are used for Figure 4.12.

	C_3 [a]	Al_2O	CO_2 [b]	unit
B_e	0.418756(2)	0.1087369(29)	0.3916404(2)	[cm^{-1}]
r_e	1.29397	1.694388(22)	1.1597904(3)	[Å]
E_D	1092.2	21188.7(6)	288977.3	[cm^{-1}]
a	0.768234	0.768234(6)	0.927876	
$\lvert q_t \rvert \cdot 10^4$	81.43(25)	4.26(8)	1.52882(20)	[cm^{-1}]
ω_2	42.773	96(2)	672.8304(4)	[cm^{-1}]
χ_{22}	6.8[c]	0.5(4)	1.6803(1)	[cm^{-1}]
χ_{22}/ω_2	15.90	0.52	0.25	[%]

[a] B_e and q_t [51]; theoretical values: r_e and ω_2 [53]

[b] Values taken from : [52]

[c] A simple approach for χ_{22} is done, by using the value of ω_2 [53] with the following approximated equation: $\chi_{22} = (\nu_2 - \omega_2)\frac{1}{3}$, neglecting χ_{12} and χ_{23}.

5 Conclusion

Within the scope of this master thesis, for the first time a rotationally resolved infrared spectrum of linear dialuminum monoxide (Al_2O) was measured and analyzed. To be able to measure Al_2O molecules, these molecules had to be produced by laser ablation of a solid aluminum rod seeded in a N_2O/He carrier gas. After passing through a short reaction channel the molecules left the ablation source and entered a vacuum region where they underwent an adiabatic expansion. A supersonic jet was formed in the vacuum and the molecules cooled down to a rotational temperature of 119 K. Within the molecular jet a collision free zone, the so called zone of silence has formed, which was the optimal region to detect the molecules spectroscopically.

For the detection of the molecules a mode-hop-free external cavity quantum cascade laser (ec-QCL) which covers a frequency range from 970 cm^{-1} to 1074 cm^{-1} with an output power of 100 mW was used. A new InfraRed Frequency Alternating Sweep Technique (IR-FAST)[43] was used to record the molecular spectrum. During the time of flight of the molecules through the laser beam region, the frequency of the ec-QCL was tuned by a sinusoidal modulation of 200 kHz, resulting in a frequency sweep of 0.025 cm^{-1}. Each frequency sweep was measured several times for 30 seconds, resulting in 600 individual spectra, before stepping forward by 0.01 cm^{-1}. By applying this measuring technique, the frequency range of one wavenumber was scanned within 50 minutes. In order to analyze the recorded molecular spectrum, a number of data reduction steps were required. First, a baseline correction was performed which then allowed to average 600 recorded spectra per frequency interval. Thereafter, all intervals were combined together to result in a full spectrum. In a last step, a calibration of the frequency axis was done, resulting in a calibrated spectrum with an accuracy of $4 \cdot 10^{-4}$ cm^{-1}.

This master thesis, has shown that the IR-FAST is a well-functioning and reliable measuring method for obtaining rotationally resolved infrared spectra. In addition, IR-FAST offers the possibility to measure a wider frequency range than with the previously

used step-scan technique within the same amount of time.

The measured spectrum has been analyzed with the program 'Pgopher'[45]. First the 'LoomisWood Plot' function of 'Pgopher' was used to assign vibrational bands and associated rotational transitions. In total seven different vibrational bands, containing 874 rotational lines, could be assigned to the Al_2O molecule (see Table 4.1). All measured ro-vibrational transitions are associated with the antisymmetric stretching vibration of ν_3. Only transitions with a transition dipole moment unequal to zero are infrared active. Thus, the symmetric ν_1 transition could not be observed.

Table 4.2 summarizes the molecular parameters of Al_2O, like the band origin ν, the rotational constant B and the centrifugal distortion constant D, which were obtained by fitting the rotational transitions of the respective vibrational bands. The vibrational band between state (12^00) and (12^01) is only tentatively assigned because other energetically lower vibrational bands like $(11^11) \leftarrow (11^10)$ could not been assigned yet, but should be populated, too. Nevertheless, many lines remain unassigned. However, further line assignments are difficult and transitions may be disturbed by energetically closely lying states. The observed spectrum clearly showed alternating intensity fluctuations of the rotational transitions, due to spin statistical effects. It is the first time, that alternating intensity fluctuations were seen in a spectrum, due the spin-statistical weights of two identical aluminum atoms ($I = \frac{5}{2}$) within a molecule. In this experiment an average line width (FWHM) of $0.0016(2)\,\mathrm{cm}^{-1}$ and an average rotational temperature of $119(12)\,\mathrm{K}$ were determined.

In this work both, a rotational and a vibrational analysis were performed. A summary of the calculated molecular parameters is given in Table 5.1. Additionally, the calculated values of Koput and Gertych[26] are shown, too. As can be seen the deviation between the experimental and theoretical parameters are minor, i.e. the respective results are in very good agreement. The rotational and vibrational analysis showed that the tentative assignment of the vibrational band $(12^01) \leftarrow (12^00)$ is reasonable.

The transitions of the vibrational band $(01^11) \leftarrow (01^10)$ showed a line splitting due to l-type doubling within the degenerated bending vibrational modes (ν_2^l). The energy difference of these splittings scales with by the l-type doubling constant q_l. The calculated values are listed in Table 5.1. The transitions of the vibrational bands $(02^21) \leftarrow (02^20)$ and $(02^01) \leftarrow (02^00)$ showed a line splitting, too. Here, a perturbation occurred between the close lying energy levels of the states $(02^0\nu_3)$ and $(02^2\nu_3)$,

Table 5.1: Obtained molecular parameters of the Al_2O molecule.

	experiment	theory[26]	deviation [%]
B_e /cm^{-1}	0.1087369(29)		
α_1 /cm^{-1}	0.0003259(19)		
α_2 /cm^{-1}	−0.0004107(16)		
α_3 /cm^{-1}	0.0007740(13)		
$D_e \cdot 10^8$ /cm^{-1}	1.94(6)		
$\beta_1 \cdot 10^{10}$ /cm^{-1}	1(5)		
$\beta_2 \cdot 10^{10}$ /cm^{-1}	−34(4)		
$\beta_3 \cdot 10^{10}$ /cm^{-1}	−3.8(2.3)		
$I \cdot 10^{45}$ /kg m^2	2.57436(7)		
γ_l /cm^{-1}	0.0001885(9)		
r_e /Å	1.694388(22)	1.707	0.73
ω_1 /cm^{-1}	519.1(3)	519.4	0.06
ω_2 /cm^{-1}	96(2)	96.8	0.83
ω_3 /cm^{-1}	1016.4(3)	1016.1	0.03
χ_{11} /cm^{-1}	−1.20(8)	−1.0	17
χ_{22} /cm^{-1}	0.5(4)	0.4	20
χ_{33} /cm^{-1}	−5.00757(9)	−4.90	2.14
χ_{12} /cm^{-1}	7.2(3)	6.4	11
χ_{13} /cm^{-1}	−6.4(4)	−6.2	3
χ_{23} /cm^{-1}	−4.7(2)	−4.8	2
g /cm^{-1}	0.48(14)	0.5	4
ZPE /cm^{-1}	862.9(1.3)	863	0.01

l-type doubling:	q_l /cm^{-1}	perturbation:	q_t /cm^{-1}	q_{tJ} /cm^{-1}
(01^10)	$2.417(7) \cdot 10^{-4}$	(02^20) and (02^00)	$4.26(8) \cdot 10^{-4}$	$3.6(4) \cdot 10^{-8}$
(01^11)	$2.479(7) \cdot 10^{-4}$	(02^21) and (02^01)	$-4.34(8) \cdot 10^{-4}$	$-3.4(4) \cdot 10^{-8}$

corresponding to molecular parameters for q_t and q_{tJ} (see Table 5.1).

A comparison between the l-type doubling constant of Al_2O with those of C_3 and CO_2 showed that $q_l = 5.5{\cdot}10^{-3}\,\mathrm{cm}^{-1}$ of C_3 is lager than q_l of Al_2O by an order of magnitude, while the $q_l = 3.5{\cdot}10^{-4}\,\mathrm{cm}^{-1}$ of CO_2 is of the same order than that of Al_2O. This means that Al_2O appears to be stiffer compared to C_3. When comparing the perturbation parameters q_t and $q_{t,J}$ between C_3, Al_2O and CO_2 a similar behavior was seen. Again, the perturbation parameter of the resonance strength of C_3 ($q_t = 8.143(25){\cdot}10^{-3}\,\mathrm{cm}^{-1}$) is one order of magnitude larger than that of Al_2O and CO_2 and the perturbation parameter of the resonance strength of Al_2O ($q_t = 4.26(8) \cdot 10^{-4}\,\mathrm{cm}^{-1}$) is slightly larger than the one for CO_2 ($q_t = 1.52882(20) \cdot 10^{-4}\ \mathrm{cm}^{-1}$).

Since Al_2O has a relative low bending vibrational frequency, the molecule would be expected to be floppy, similar to C_3. However, a comparison of the Morse potential between C_3, Al_2O and CO_2 showed that the harmonic part of the potential of C_3 deviates stronger from the Morse potential than those of Al_2O and CO_2. A comparison between Al_2O and CO_2 showed that the harmonic part in CO_2 contributes stronger to the potential curve than in Al_2O. This, and the ratio of the anharmonic component χ_{22} and the harmonic component ω_2 of the potential, indicates that Al_2O is not so much floppy.

Al_2O is thought to be a relevant molecule in circumstellar envelopes of oxygen rich late-type stars. However, since this molecule cannot be observed at radio and submm wavelength it could not be identified in these stellar environments yet. The results of this master thesis provide a good basis to enable observation in the infrared region. Instruments like TEXES at the IRTF[1] or EXES on board the SOFIA[2] which have a resolution power of $R = 10^5$ $\left(R = \frac{\lambda}{\Delta\lambda}\right)$ are able to resolve the ro-vibrational spectra of Al_2O. A good candidate to detect Al_2O would be the oxygen rich M-type star VY Canis Majoris. In 2009, Tenenbaum and Ziury[11] detected AlO in the circumstellar shell of this star, indicating that there is a sufficient amount of aluminum to form molecules in this environment. The here investigated molecular Al_2O may act as a seed nuclei for dust grains thus, the detection of Al_2O is an important step towards a better understanding of cosmic dust formation.

[1] InfraRed Telescope Facility
[2] Stratospheric Observatory For Infrared Astronomy

6 Appendix

6.1 Linelist

Table 6.1: Observed Transitions for Al_2O, $(01^11) \leftarrow (01^10)$. Experimental errors for line positions are better then $1 \cdot 10^{-3}\,cm^{-1}$. e and f indicates the parity for each state.

J'	J''	Frequency $[cm^{-1}]$	Obs-Calc $[10^{-4}\,cm^{-1}]$	E_{lower} [K]	J'	J''	Frequency $[cm^{-1}]$	Obs-Calc $[10^{-4}\,cm^{-1}]$	E_{lower} [K]
62e	61e	977.25	-1.12	757.696	62f	61f	977.2566	1.84	756.3383
61e	60e	977.5586	-1.36	738.1991	61f	60f	977.5654	0.3	736.8845
60f	59f	977.8731	3.62	717.7432	59e	58e	978.1712	-3.66	700.1451
59f	58f	978.1782	-4.66	698.9146	58e	57e	978.4753	-4.35	681.5882
58f	57f	978.4829	-1.71	680.3988	55e	54e	979.3797	1.52	627.7986
55f	54f	979.3875	0.15	626.728	54e	53e	979.6781	3.19	610.4959
54f	53f	979.686	-0.13	609.4635	53e	52e	979.9748	1.36	593.5068
53f	52f	979.9828	-2.33	592.512	52e	51e	980.27	-0.17	576.8315
52f	51f	980.2787	1.23	575.8735	51e	50e	980.5642	2.11	560.4699
51f	50f	980.5729	2.87	559.5481	50e	49e	980.8567	2.68	544.4222
50f	49f	980.8649	-3.1	543.5359	48e	47e	981.4368	-1.15	513.2684
48f	47f	981.4459	-1.1	512.4509	47e	46e	981.7245	-3.62	498.1625
47f	46f	981.7339	-1.57	497.3783	46e	45e	982.0116	0.94	483.3705
46f	45f	982.0206	-2.08	482.619	45e	44e	982.2971	5.49	468.8926
45f	44f	982.3063	3.36	468.1731	44e	43e	982.5806	3.9	454.7288
44f	43f	982.5899	2.08	454.0406	43e	42e	982.8629	5.41	440.8791
43f	42f	982.8723	4.54	440.2215	42e	41e	983.1433	1.76	427.3436
42f	41f	983.1521	-4.76	426.7159	41e	40e	983.423	6.48	414.1223
41f	40f	983.4321	2.27	413.5238	40e	39e	983.7013	12.38	401.2153
40f	39f	983.7104	7.76	400.6453	39e	38e	983.9766	2.5	388.6226

Table 6.1: *continued...*

J'	J''	Frequency [cm^{-1}]	Obs-Calc [$10^{-4}\,cm^{-1}$]	E_{lower} [K]	J'	J''	Frequency [cm^{-1}]	Obs-Calc [$10^{-4}\,cm^{-1}$]	E_{lower} [K]
39f	38f	983.9862	2.16	388.0804	38e	37e	984.251	-2.56	376.3442
38f	37f	984.26	-7.77	375.8291	37e	36e	984.5246	-0.08	364.3802
37f	36f	984.5338	-3.39	363.8915	36e	35e	984.7966	0.45	352.7306
36f	35f	984.8059	-1.58	352.2676	35e	34e	985.0668	-2.03	341.3955
35f	34f	985.0762	-2.39	340.9575	34e	33e	985.3352	-7.53	330.3748
34f	33f	985.3451	-2.66	329.9612	33e	32e	985.6035	0.69	319.6686
33f	32f	985.6123	-4.51	319.2786	32e	31e	985.8691	-3.65	309.277
32f	31f	985.8779	-8.54	308.9099	31e	30e	986.1341	0.57	299.1999
31f	30f	986.1433	0.35	298.8551	30e	29e	986.3974	2.61	289.4375
30f	29f	986.4062	-0.17	289.1142	29e	28e	986.6581	-7.1	279.9897
29f	28f	986.667	-7.76	279.6873	28e	27e	986.9197	6.49	270.8565
28f	27f	986.9281	2.57	270.5742	27e	26e	987.1782	5.1	262.038
27f	26f	987.1867	2.64	261.7752	26e	25e	987.435	-0.36	253.5343
26f	25f	987.4435	-0.28	253.2902	25e	24e	987.6907	-0.56	245.3452
25f	24f	987.699	-1.17	245.1193	24e	23e	987.9448	-2.52	237.471
24f	23f	987.9528	-4.05	237.2624	23e	22e	988.1979	-0.21	229.9115
23f	22f	988.2058	-0.8	229.7196	22e	21e	988.4496	2.55	222.6668
22f	21f	988.4571	0.28	222.4909	21e	20e	988.6988	-4.51	215.737
21f	20f	988.7065	-3.03	215.5764	20e	19e	988.9474	-3.39	209.122
20f	19f	988.9547	-2.81	208.976	19e	18e	989.1942	-5.01	202.8219
19f	18f	989.2015	-2.56	202.6898	18e	17e	989.4402	-0.4	196.8367
18f	17f	989.447	-0.3	196.7178	17e	16e	989.684	-3.02	191.1663
17f	16f	989.6908	0.48	191.06	16e	15e	989.9269	0.61	185.8109
16f	15f	989.933	-0.89	185.7164	15e	14e	990.1674	-6.1	180.7705
15f	14f	990.1738	-1.48	180.6871	14e	13e	990.4071	-5.5	176.045
14f	13f	990.4129	-3.66	175.972	13e	12e	990.6457	-1.09	171.6345
13f	12f	990.6509	-2.11	171.5712	12e	11e	990.882	-4.78	167.5389
12f	11f	990.8873	-1.7	167.4847	11e	10e	991.1191	13.17	163.7584
11f	10f	991.1236	12.58	163.7125	10e	9e	991.3523	7.44	160.2928
10f	9f	991.3563	5.39	160.2546	9e	8e	991.584	2.09	157.1423
9f	8f	991.5882	4.85	157.111	8e	7e	991.8145	-1.07	154.3068
8f	7f	991.8182	-0.07	154.2818	7e	6e	992.0443	2.85	151.7863
7f	6f	992.0472	1.2	151.7669	6e	5e	992.2719	-0.23	149.5809
6f	5f	992.2746	0.14	149.5663	5e	4e	992.4981	-2.25	147.6905
5f	4f	992.501	3.91	147.6801	4e	3e	992.7224	-8.35	146.1152
4f	3f	992.7243	-7.58	146.1083	3f	2f	992.9475	-6.04	144.8508
3e	2e	992.9475	8.09	144.855	2f	1f	993.1695	-1.61	143.9077
2e	1e	993.1695	7.93	143.9098	5e	5f	993.5785	-1.49	147.6905
3e	3f	993.5972	7.49	144.855	4f	4e	993.5988	4.37	146.1083
2f	2e	993.6059	6.59	143.9077	1e	1f	993.6069	6.09	143.2796
1f	1e	993.6074	1.31	143.2789	1e	2e	994.0415	-4.19	143.2796
1f	2f	994.0415	5.85	143.2789	2f	3f	994.2551	1.2	143.9077

Table 6.1: *continued...*

J'	J''	Frequency [cm^{-1}]	Obs-Calc [$10^{-4}\,cm^{-1}$]	E_{lower} [K]	J'	J''	Frequency [cm^{-1}]	Obs-Calc [$10^{-4}\,cm^{-1}$]	E_{lower} [K]
2e	3e	994.2567	2.23	143.9098	3f	4f	994.4672	-3.61	144.8508
3e	4e	994.47	3.22	144.855	4f	5f	994.6785	-1.48	146.1083
4e	5e	994.6814	1.44	146.1152	5f	6f	994.8883	-0.35	147.6801
5e	6e	994.8913	-1.32	147.6905	6f	7f	995.0959	-4.67	149.5663
6e	7e	995.1002	0.05	149.5809	7f	8f	995.3032	1.78	151.7669
7e	8e	995.3076	2.17	151.7863	8f	9f	995.508	-1.34	154.2818
8e	9e	995.5132	0.83	154.3068	9f	10f	995.7118	0.01	157.111
9e	10e	995.7174	0.52	157.1423	10f	11f	995.914	0.16	160.2546
10e	11e	995.9203	1.98	160.2928	11f	12f	996.1147	1.29	163.7125
11e	12e	996.1216	2.57	163.7584	12f	13f	996.3138	0.78	167.4847
12e	13e	996.3215	3.3	167.5389	13f	14f	996.511	-3.97	171.5712
13e	14e	996.5194	-0.2	171.6345	14f	15f	996.7072	-2.87	175.972
14e	15e	996.7163	-0.08	176.045	15f	16f	996.9019	-2.91	180.6871
15e	16e	996.9117	1.29	180.7705	16f	17f	997.0953	-0.44	185.7164
16e	17e	997.1058	3.49	185.8109	17f	18f	997.2869	-0.17	191.06
17e	18e	997.2979	1.14	191.1663	18f	19f	997.4768	-2.9	196.7178
18e	19e	997.4888	1.99	196.8367	19f	20f	997.6657	0.41	202.6898
19e	20e	997.6784	3.81	202.8219	20f	21f	997.8526	-1.82	208.976
20e	21e	997.8661	2.92	209.122	21f	22f	998.0385	0.87	215.5764
21e	22e	998.0525	3.15	215.737	22f	23f	998.2225	-0.68	222.4909
22e	23e	998.237	-0.62	222.6668	23f	24f	998.4047	-4.41	229.7196
23e	24e	998.4203	-1.44	229.9115	24f	25f	998.5863	0.91	237.2624
24e	25e	998.6028	4.44	237.471	25f	26f	998.7656	-1.71	245.1193
25e	26e	998.7832	4.37	245.3452	26f	27f	998.9438	-0.16	253.2902
26e	27e	998.962	3.27	253.5343	27f	28f	999.1202	-2.55	261.7752
27e	28e	999.1391	0.96	262.038	28f	29f	999.2952	-2.85	270.5742
28e	29e	999.315	1.48	270.8565	29f	30f	999.4688	-1.33	279.6873
29e	30e	999.4897	4.3	279.9897	30f	31f	999.641	0.15	289.1142
30e	31e	999.6626	5.05	289.4375	31f	32f	999.8114	0.0	298.8551
31e	32e	999.834	4.87	299.1999	32f	33f	999.9803	-1.29	308.9099
32e	33e	1000.0037	3.21	309.277	33f	34f	1000.1476	-2.63	319.2786
33e	34e	1000.172	2.62	319.6686	34f	35f	1000.3135	-2.8	329.9612
34e	35e	1000.3389	3.52	330.3748	35f	36f	1000.4782	0.23	340.9575
35e	36e	1000.504	1.69	341.3955	36f	37f	1000.6412	2.21	352.2676
36e	37e	1000.668	3.59	352.7306	37f	38f	1000.8022	-1.12	363.8915
37e	38e	1000.8304	3.74	364.3802	38f	39f	1000.9622	0.44	375.8291
38e	39e	1000.9912	4.4	376.3442	39f	40f	1001.1206	1.59	388.0804

Table 6.1: *continued...*

J'	J''	Frequency [cm^{-1}]	Obs-Calc [$10^{-4}\,cm^{-1}$]	E_{lower} [K]	J'	J''	Frequency [cm^{-1}]	Obs-Calc [$10^{-4}\,cm^{-1}$]	E_{lower} [K]
39e	40e	1001.1502	1.76	388.6226	40f	41f	1001.2767	-5.0	400.6453
40e	41e	1001.3083	5.13	401.2153	41f	42f	1001.4326	1.81	413.5238
41e	42e	1001.4638	-1.7	414.1223	42f	43f	1001.5863	1.95	426.7159
42e	43e	1001.6188	1.11	427.3436	43f	44f	1001.7384	1.27	440.2215
43e	44e	1001.7723	4.12	440.8791	44f	45f	1001.8891	2.86	454.0406
44e	45e	1001.9238	2.39	454.7288	45f	46f	1002.0381	1.81	468.1731
45e	46e	1002.0738	1.6	468.8926	46f	47f	1002.1856	1.72	482.619
46e	47e	1002.2222	-0.93	483.3705	47f	48f	1002.331	-3.92	497.3783
48f	49f	1002.4763	4.28	512.4509	48e	49e	1002.5149	0.44	513.2684
49f	50f	1002.6194	6.11	527.8368	49e	50e	1002.6586	-2.61	528.6884
50f	51f	1002.7601	0.26	543.5359	50e	51e	1002.8006	-7.63	544.4222
51f	52f	1002.9003	3.84	559.5481	51e	52e	1002.9419	-3.85	560.4699
52f	53f	1003.0384	2.23	575.8735	52e	53e	1003.082	2.85	576.8315
53f	54f	1003.1759	10.33	592.512	53e	54e	1003.2199	3.8	593.5068
54f	55f	1003.3108	8.09	609.4635	54e	55e	1003.3559	0.68	610.4959
55f	56f	1003.4441	5.01	626.728	55e	56e	1003.4907	0.81	627.7986
56f	57f	1003.5758	1.54	644.3054	57f	58f	1003.7057	-4.32	662.1957
57e	58e	1003.755	-5.26	663.3448	58f	59f	1003.8366	15.67	680.3988
58e	59e	1003.8849	-7.84	681.5882	59f	60f	1003.9631	7.1	698.9146
59e	60e	1004.014	-2.27	700.1451	60f	61f	1004.088	-1.28	717.7432
60e	61e	1004.1411	-2.01	719.0154	61f	62f	1004.2126	2.18	736.8845
61e	62e	1004.2663	-5.08	738.1991	62f	63f	1004.335	-0.73	756.3383
62e	63e	1004.3901	-5.56	757.696					

Table 6.2: Observed Transitions for Al_2O, $(02^01) \leftarrow (02^00)$. Experimental errors for line positions are better then $1 \cdot 10^{-3}\,cm^{-1}$.

J'	J''	Frequency [cm^{-1}]	Obs-Calc [$10^{-4}\,cm^{-1}$]	E_{lower} [K]	J'	J''	Frequency [cm^{-1}]	Obs-Calc [$10^{-4}\,cm^{-1}$]	E_{lower} [K]
52	51	975.8898	-13.79	718.7538	51	50	976.1821	-11.42	702.4329
47	46	977.337	-2.3	640.273	46	45	977.6222	0.29	625.5143
45	44	977.9055	-2.46	611.0684	44	43	978.1881	2.94	596.9353
42	41	978.7481	4.34	569.6076	41	40	979.0275	20.83	556.4133
39	38	979.5778	10.51	530.964	38	37	979.851	8.29	518.7091
37	36	980.1229	7.14	506.7675	36	35	980.3937	8.89	495.1393
35	34	980.6628	8.23	483.8245	34	33	980.9304	7.27	472.8232
33	32	981.1964	4.32	462.1355	32	31	981.4616	8.54	451.7613
31	30	981.7245	4.01	441.7009	30	29	981.9864	3.54	431.9541
29	28	982.2473	7.48	422.5212	28	27	982.5059	2.9	413.4021
27	26	982.7639	7.24	404.5968	26	25	983.0196	2.74	396.1055
25	24	983.2735	-5.23	387.9283	24	23	983.5271	-1.73	380.065
23	22	983.7789	-0.75	372.5159	22	21	984.029	-3.51	365.2809
21	20	984.2773	-9.94	358.3601	20	19	984.5246	-11.08	351.7535
19	18	984.7709	-7.57	345.4613	18	17	985.0155	-7.12	339.4833
17	16	985.2588	-6.06	333.8197	16	15	985.5001	-9.49	328.4705
15	14	985.7403	-10.03	323.4358	14	13	985.9791	-9.55	318.7156
13	12	986.2172	-2.3	314.3098	12	11	986.4527	-6.51	310.2186
11	10	986.6868	-11.45	306.442	10	9	986.9206	-4.13	302.98
9	8	987.1528	1.59	299.8327	8	7	987.3828	-0.46	297.0
7	6	987.6108	-8.31	294.4819	6	5	987.8388	-1.89	292.2786
5	4	988.0648	-1.66	290.3901	4	3	988.2898	2.88	288.8162
3	2	988.5122	-4.04	287.5571	2	1	988.7334	-9.43	286.6128
1	0	988.9547	1.32	285.9832	0	1	989.3908	-0.57	285.6685
1	2	989.6068	0.1	285.9832	2	3	989.8214	0.67	286.6128
3	4	990.035	4.79	287.5571	4	5	990.2464	2.63	288.8162
5	6	990.4563	-0.67	290.3901	6	7	990.6651	-0.54	292.2786
7	8	990.8723	-2.39	294.4819	8	9	991.0795	11.37	297.0
9	10	991.2831	3.05	299.8327	10	11	991.4863	5.55	302.98
11	12	991.6876	3.34	306.442	12	13	991.8875	2.07	310.2186
13	14	992.0862	4.33	314.3098	14	15	992.283	2.04	318.7156
15	16	992.4784	-0.04	323.4358	16	17	992.6729	4.14	328.4705
17	18	992.8653	3.19	333.8197	18	19	993.0573	12.47	339.4833

Table 6.2: *continued...*

J'	J''	Frequency [cm^{-1}]	Obs-Calc [$10^{-4}\,cm^{-1}$]	E_{lower} [K]	J'	J''	Frequency [cm^{-1}]	Obs-Calc [$10^{-4}\,cm^{-1}$]	E_{lower} [K]
19	20	993.2457	0.29	345.4613	20	21	993.4339	1.77	351.7535
21	22	993.6205	2.58	358.3601	22	23	993.806	7.09	365.2809
23	24	993.9894	5.65	372.5159	24	25	994.171	1.43	380.065
25	26	994.3519	5.6	387.9283	26	27	994.5307	4.13	396.1055
27	28	994.7082	4.18	404.5968	28	29	994.8838	0.74	413.4021
29	30	995.0588	6.79	422.5212	30	31	995.2313	3.61	431.9541
31	32	995.4021	-2.05	441.7009	32	33	995.5725	3.72	451.7613
33	34	995.7401	-3.81	462.1355	34	35	995.9077	4.9	472.8232
35	36	996.0717	-7.3	483.8245	36	37	996.2356	-5.19	495.1393
37	38	996.3978	-5.72	506.7675	38	39	996.5593	2.73	518.7091
39	40	996.7172	-9.47	530.964	40	41	996.8747	-9.41	543.5321
41	42	997.031	-7.83	556.4133	42	43	997.1858	-4.94	569.6076
43	44	997.3386	-6.01	583.115	44	45	997.49	-7.3	596.9353
45	46	997.6395	-11.41	611.0684	46	47	997.7878	-11.8	625.5143
47	48	997.9351	-7.06	640.273	48	49	998.08	-10.74	655.3442
49	50	998.2246	-2.48	670.728	50	51	998.3662	-9.1	686.4243
51	52	998.5081	3.5	702.4329	52	53	998.6467	-1.54	718.7538
53	54	998.7848	2.83	735.387	54	55	998.9204	-1.0	752.3322
55	56	999.0557	6.61	769.5894	56	57	999.1887	7.2	787.1585
57	58	999.3196	1.98	805.0395	58	59	999.4506	14.06	823.2322
59	60	999.5783	7.78	841.7364	60	61	999.7046	3.2	860.5522

Table 6.3: Observed Transitions for Al_2O, $(02^21) \leftarrow (02^20)$. Experimental errors for line positions are better then $1 \cdot 10^{-3}\,cm^{-1}$. e and f indicates the parity for each state.

J'	J''	Frequency [cm^{-1}]	Obs-Calc [$10^{-4}\,cm^{-1}$]	E_{lower} [K]	J'	J''	Frequency [cm^{-1}]	Obs-Calc [$10^{-4}\,cm^{-1}$]	E_{lower} [K]
46f	45f	977.1859	-7.6	630.7666	44f	43f	977.7529	-3.05	601.9562
44e	43e	977.7601	14.26	602.156	41f	40f	978.5923	-2.64	561.1104
41e	40e	978.5978	2.46	561.2658	39f	38f	979.1453	2.98	535.4601
39e	38e	979.1495	-0.53	535.5901	38f	37f	979.4193	1.89	523.1092
38e	37e	979.4232	-2.01	523.2276	37f	36f	979.6918	-0.45	511.0744
37e	36e	979.6961	2.28	511.1821	36f	35f	979.9635	3.91	499.3559
36e	35e	979.9666	-3.31	499.4535	35f	34f	980.2332	1.4	487.9536
35e	34e	980.2359	-6.43	488.0418	34f	33f	980.5018	3.02	476.8677
34e	33e	980.5042	-5.63	476.9471	33f	32f	980.769	3.8	466.0981
33e	32e	980.7707	-8.86	466.1694	32f	31f	981.0349	6.33	455.6449
32e	31e	981.0363	-7.29	455.7086	31f	30f	981.2992	6.64	445.5081
31e	30e	981.3004	-6.04	445.5649	29f	28f	981.8238	9.25	426.1838
29e	28e	981.8238	-9.88	426.2283	28e	27e	982.0836	-9.86	417.0356
27e	26e	982.3425	-4.32	408.1598	26e	25e	982.5996	-3.59	399.6011
26f	25f	982.5996	8.63	399.5713	25f	24f	982.8552	7.13	391.3336
25e	24e	982.8552	-3.08	391.3594	24e	23e	983.1095	-1.97	383.4347
24f	23f	983.1095	6.4	383.4125	23e	22e	983.3619	-6.24	375.827
23f	22f	983.3619	0.46	375.8081	22f	21f	983.6146	12.16	368.5203
22e	21e	983.6146	6.93	368.5363	21f	20f	983.8644	8.49	361.5492
21e	20e	983.8644	4.57	361.5627	20f	19f	984.1126	2.93	354.8948
20e	19e	984.1126	0.14	354.9061	19e	18e	984.3592	-5.37	348.5665
19f	18f	984.3592	-3.54	348.5572	18f	17f	984.6054	-1.0	342.5363
18e	17e	984.6054	-2.05	342.5439	17f	16f	984.8497	-2.63	336.8322
17e	16e	984.8497	-3.05	336.8383	16f	15f	985.093	-0.63	331.4449
16e	15e	985.093	-0.56	331.4498	15f	14f	985.3352	4.9	326.3744
15e	14e	985.3352	5.31	326.3782	14e	13e	985.5748	-0.47	321.6237
14f	13f	985.5748	-1.12	321.6207	13e	12e	985.8136	-0.57	317.1861
13f	12f	985.8136	-1.35	317.1839	12f	11f	986.0507	-4.24	313.0639
12e	11e	986.0507	-3.41	313.0656	11e	10e	986.2874	3.82	309.262
11f	10f	986.2874	3.01	309.2608	10f	9f	986.5213	-4.37	305.7746
10e	9e	986.5213	-3.62	305.7754	9f	8f	986.7546	-2.65	302.6053
9e	8e	986.7546	-2.01	302.6058	8f	7f	986.9869	3.34	299.7529
8e	7e	986.9869	3.86	299.7532	7e	6e	987.2168	-0.39	297.2176

Table 6.3: *continued...*

J'	J''	Frequency [cm^{-1}]	Obs-Calc [$10^{-4}\,cm^{-1}$]	E_{lower} [K]	J'	J''	Frequency [cm^{-1}]	Obs-Calc [$10^{-4}\,cm^{-1}$]	E_{lower} [K]
7f	6f	987.2168	-0.79	297.2174	6e	5e	987.4461	3.63	294.9989
6f	5f	987.4461	3.35	294.9988	5e	4e	987.6727	-5.02	293.0972
5f	4f	987.6727	-5.19	293.0971	4e	3e	987.8992	-0.67	291.5124
4f	3f	987.8992	-0.77	291.5124	3f	2f	988.1238	-0.86	290.2446
3e	2e	988.1238	-0.82	290.2446	10e	10f	988.7108	5.89	305.7754
10f	10e	988.7108	-7.02	305.7746	9e	9f	988.725	2.83	302.6058
9f	9e	988.725	-5.83	302.6053	8f	8e	988.7379	-3.39	299.7529
8e	8f	988.7379	2.15	299.7532	7e	7f	988.7493	1.24	297.2176
7f	7e	988.7493	-2.1	297.2174	6e	6f	988.7591	-0.74	294.9989
6f	6e	988.7591	-2.6	294.9988	5e	5f	988.7675	-3.09	293.0972
5f	5e	988.7675	-4.03	293.0971	4e	4f	988.7747	-2.15	291.5124
4f	4e	988.7747	-2.55	291.5124	2f	2e	988.7846	-2.87	289.2938
2e	2f	988.7846	-2.84	289.2938	3f	4f	989.6564	1.1	290.2446
3e	4e	989.6564	0.93	290.2446	4f	5f	989.8696	0.28	291.5124
4e	5e	989.8696	-0.07	291.5124	5f	6f	990.0813	-0.11	293.0971
5e	6e	990.0813	-0.76	293.0972	6f	7f	990.292	3.44	294.9988
6e	7e	990.292	2.36	294.9989	7e	8e	990.5003	-4.48	297.2176
7f	8f	990.5003	-2.8	297.2174	8f	9f	990.7079	-1.69	299.7529
8e	9e	990.7079	-4.17	299.7532	9e	10e	990.9142	-2.51	302.6058
9f	10f	990.9142	1.0	302.6053	10e	11e	991.1191	-1.29	305.7754
10f	11f	991.1191	3.52	305.7746	11f	12f	991.3228	8.72	309.2608
11e	12e	991.3228	2.31	309.262	12e	13e	991.5242	-3.69	313.0656
12f	13f	991.5242	4.64	313.0639	13f	14f	991.725	9.81	317.1839
13e	14e	991.725	-0.81	317.1861	14f	15f	991.9235	6.22	321.6207
14e	15e	991.9235	-7.06	321.6237	15e	16e	992.1228	8.19	326.3782
16f	17f	992.3172	8.04	331.4449	16e	17e	992.3188	4.2	331.4498
17f	18f	992.5115	5.32	336.8322	17e	18e	992.5131	-2.32	336.8383
18f	19f	992.7043	2.28	342.5363	18e	19e	992.7066	-2.45	342.5439
19f	20f	992.8962	4.3	348.5572	19e	20e	992.8989	-1.64	348.5665
20f	21f	993.087	10.14	354.8948	20e	21e	993.09	1.6	354.9061
21f	22f	993.2751	2.95	361.5492	21e	22e	993.2784	-8.26	361.5627
22f	23f	993.4624	2.66	368.5203	22e	23e	993.4666	-5.93	368.5363
23f	24f	993.6488	8.33	375.8081	23e	24e	993.6535	-3.0	375.827

Table 6.3: *continued...*

J'	J''	Frequency [cm^{-1}]	Obs-Calc [$10^{-4}\,cm^{-1}$]	E_{lower} [K]	J'	J''	Frequency [cm^{-1}]	Obs-Calc [$10^{-4}\,cm^{-1}$]	E_{lower} [K]
24f	25f	993.833	5.33	383.4125	24e	25e	993.8387	-3.4	383.4347
25f	26f	994.016	5.15	391.3336	25e	26e	994.022	-7.61	391.3594
26f	27f	994.1972	1.47	399.5713	26e	27e	994.2045	-6.63	399.6011
27f	28f	994.3772	0.87	408.1256	27e	28e	994.3856	-5.7	408.1598
28f	29f	994.5561	2.84	416.9964	28e	29e	994.5649	-8.51	417.0356
29f	30f	994.7337	7.32	426.1838	29e	30e	994.743	-9.84	426.2283
30f	31f	994.9087	-0.32	435.6877	30e	31e	994.9196	-11.56	435.7381
31f	32f	995.0836	5.43	445.5081	31e	32e	995.0951	-9.98	445.5649
32f	33f	995.2563	4.08	455.6449	32e	33e	995.2695	-4.97	455.7086
33f	34f	995.4271	-1.37	466.0981	33e	34e	995.4417	-8.14	466.1694
34f	35f	995.5975	3.37	476.8677	34e	35e	995.613	-6.41	476.9471
35f	36f	995.7659	1.87	487.9536	36f	37f	995.9329	2.73	499.3559
36e	37e	995.9511	-4.54	499.4535	37f	38f	996.0987	4.73	511.0744
37e	38e	996.1187	3.61	511.1821	38f	39f	996.2627	4.13	523.1092
38e	39e	996.2842	5.65	523.2276	39f	40f	996.4243	-5.66	535.4601
39e	40e	996.4483	7.18	535.5901	40f	41f	996.5853	-7.72	548.1272
40e	41e	996.6106	6.26	548.2695	41f	42f	996.7451	-6.25	561.1104
41e	42e	996.7719	9.48	561.2658	43f	44f	997.0601	-6.33	588.025

Table 6.4: Observed Transitions for Al_2O, $(10^0 1) \leftarrow (10^0 0)$. Experimental errors for line positions are better then $1 \cdot 10^{-3}\,cm^{-1}$.

J'	J''	Frequency [cm^{-1}]	Obs-Calc [$10^{-4}\,cm^{-1}$]	E_{lower} [K]	J'	J''	Frequency [cm^{-1}]	Obs-Calc [$10^{-4}\,cm^{-1}$]	E_{lower} [K]
56	55	977.6787	1.64	1245.7677	55	54	977.9801	-0.94	1228.3478
54	53	978.2819	16.66	1211.2383	53	52	978.5781	-6.18	1194.439
49	48	979.7579	3.87	1130.3459	48	47	980.0482	-1.42	1115.0989
47	46	980.3377	0.37	1100.1623	46	45	980.626	6.13	1085.5364
45	44	980.9106	-10.46	1071.2211	44	43	981.1964	1.02	1057.2165
43	42	981.4788	-5.64	1043.5226	42	41	981.7611	1.56	1030.1394
41	40	982.0415	4.73	1017.067	40	39	982.3199	3.35	1004.3053
39	38	982.5971	5.65	991.8546	38	37	982.8722	3.2	979.7146
37	36	983.1463	5.17	967.8856	36	35	983.4183	1.35	956.3675
35	34	983.689	0.83	945.1604	34	33	983.9577	-4.3	934.2642
33	32	984.2257	-1.62	923.6791	32	31	984.4914	-6.06	913.405
31	30	984.7564	-2.84	903.442	30	29	985.0192	-4.74	893.79
29	28	985.2816	3.37	884.4492	28	27	985.5409	-3.11	875.4195
27	26	985.7996	-0.21	866.701	26	25	986.0561	-4.03	858.2936
25	24	986.3123	4.11	850.1975	24	23	986.5648	-8.82	842.4125
23	22	986.8177	-1.74	834.9389	22	21	987.0694	8.33	827.7764
21	20	987.3181	3.06	820.9253	20	19	987.565	-3.61	814.3855
19	18	987.8111	-2.69	808.1569	18	17	988.0558	-1.25	802.2397
17	16	988.2992	3.47	796.6339	16	15	988.5404	0.98	791.3394
15	14	988.7799	-2.65	786.3563	14	13	989.0182	-1.87	781.6845
13	12	989.2553	1.55	777.3242	12	11	989.4906	2.25	773.2752
11	10	989.724	-0.56	769.5377	10	9	989.956	-1.33	766.1116
9	8	990.1866	-0.33	762.997	8	7	990.4154	-2.02	760.1938
7	6	990.643	-0.63	757.702	6	5	990.8684	-5.22	755.5217
5	4	991.0942	9.02	753.6528	4	3	991.3164	3.59	752.0955
3	2	991.5378	5.3	750.8496	2	1	991.7571	1.52	749.9151
1	0	991.9752	2.05	749.2922	1	2	992.62	0.35	749.2922
2	3	992.8316	-2.39	749.9151	3	4	993.0424	1.88	750.8496
4	5	993.2506	-3.42	752.0955	5	6	993.4578	-3.45	753.6528
6	7	993.6651	13.29	755.5217	7	8	993.8681	2.79	757.702
8	9	994.0703	0.07	760.1938	9	10	994.2712	-0.14	762.997
10	11	994.4701	-4.76	766.1116	11	12	994.6685	1.34	769.5377
12	13	994.8644	-2.2	773.2752	13	14	995.0588	-5.54	777.3242

Table 6.4: *continued...*

J'	J''	Frequency [cm^{-1}]	Obs-Calc [$10^{-4}\,cm^{-1}$]	E_{lower} [K]	J'	J''	Frequency [cm^{-1}]	Obs-Calc [$10^{-4}\,cm^{-1}$]	E_{lower} [K]
14	15	995.2527	2.24	781.6845	15	16	995.444	0.34	786.3563
16	17	995.634	0.96	791.3394	17	18	995.8225	1.0	796.6339
18	19	996.0095	3.25	802.2397	19	20	996.1946	1.0	808.1569
20	21	996.3782	0.18	814.3855	21	22	996.5597	-5.98	820.9253
22	23	996.7407	-1.01	827.7764	23	24	996.9199	1.1	834.9389
24	25	997.0977	4.32	842.4125	25	26	997.2732	1.81	850.1975
26	27	997.4473	-0.27	858.2936	27	28	997.6204	4.12	866.701
28	29	997.791	-0.91	875.4195	29	30	997.9608	1.43	884.4492
30	31	998.1287	1.26	893.79	31	32	998.2947	-2.51	903.442
32	33	998.4595	-1.96	913.405	33	34	998.6228	-1.06	923.6791
34	35	998.7846	-0.33	934.2642	35	36	998.9446	-0.3	945.1604
36	37	999.1028	-3.13	956.3675	37	38	999.2599	-0.72	967.8856
38	39	999.4151	-1.57	979.7146	39	40	999.5691	1.59	991.8546
40	41	999.7214	2.87	1004.3053	41	42	999.8715	-1.41	1017.067
42	43	1000.0204	-1.77	1030.1394	43	44	1000.1677	-2.43	1043.5226
44	45	1000.3138	0.57	1057.2165	45	46	1000.4586	6.58	1071.2211
46	47	1000.6003	-1.67	1085.5364	47	48	1000.7417	2.2	1100.1623
48	49	1000.881	1.39	1115.0989	49	50	1001.0189	2.49	1130.3459
50	51	1001.1543	-6.04	1145.9035	51	52	1001.2893	-1.9	1161.7716
52	53	1001.4228	2.57	1177.9501	53	54	1001.5539	-0.97	1194.439
54	55	1001.6842	3.89	1211.2383					

Table 6.5: Observed Transitions for Al_2O, $(12^01) \leftarrow (12^00)$. Experimental errors for line positions are better then $1{\cdot}10^{-3}\,cm^{-1}$. This band is tentatively assigned.

J'	J''	Frequency [cm^{-1}]	Obs-Calc [$10^{-4}\,cm^{-1}$]	E_{lower} [K]	J'	J''	Frequency [cm^{-1}]	Obs-Calc [$10^{-4}\,cm^{-1}$]	E_{lower} [K]
36	35	975.7693	2.99	1262.7844	35	34	976.0359	0.21	1251.4428
34	33	976.3027	12.06	1240.4158	32	31	976.8253	-31.49	1219.3064
30	29	977.3502	2.76	1199.4564	29	28	977.6087	0.63	1190.0036
28	27	977.8658	-2.27	1180.8658	27	26	978.1218	-1.38	1172.0429
26	25	978.3766	0.8	1163.535	25	24	978.6296	-1.94	1155.342
24	23	978.8811	-5.97	1147.464	23	22	979.1317	-4.83	1139.9009
21	20	979.6295	2.87	1125.7199	20	19	979.8757	1.3	1119.102
19	18	980.1201	-5.45	1112.799	18	17	980.3644	0.31	1106.8112
14	13	981.3258	2.8	1086.0107	13	12	981.5623	-1.21	1081.5983
12	11	981.7982	2.52	1077.5011	11	10	982.0321	0.44	1073.719
10	9	982.265	1.48	1070.2521	9	8	982.4964	0.91	1067.1003
8	7	982.7268	4.66	1064.2637	7	6	982.955	0.2	1061.7422
6	5	983.1826	2.73	1059.5359	3	2	983.8556	-5.1	1054.8081
2	1	984.0787	6.95	1053.8625	1	2	984.951	-7.49	1053.2322
2	3	985.1666	-1.87	1053.8625	3	4	985.3809	4.82	1054.8081
4	5	985.5932	5.42	1056.0689	5	6	985.8031	-5.27	1057.6448
6	7	986.0128	-3.55	1059.5359	7	8	986.2215	2.37	1061.7422
8	9	986.4282	0.99	1064.2637	9	10	986.6331	-3.97	1067.1003
10	11	986.8375	-0.1	1070.2521	11	12	987.0406	3.73	1073.719
12	13	987.2416	0.9	1077.5011	13	14	987.4413	-0.51	1081.5983
14	15	987.6395	-4.45	1086.0107	15	16	987.8372	0.93	1090.7382
16	17	988.0324	-4.54	1095.7807	17	18	988.2273	0.52	1101.1384
18	19	988.4201	-1.84	1106.8112	19	20	988.6117	-2.56	1112.799
20	21	988.8017	-4.22	1119.102	21	22	988.991	-0.74	1125.7199
22	23	989.1781	-4.17	1132.6529	23	24	989.3644	-2.07	1139.9009
24	25	989.5491	-2.2	1147.464	25	26	989.7327	0.74	1155.342
26	27	989.9146	-0.02	1163.535	27	28	990.0956	5.08	1172.0429
28	29	990.2746	2.68	1180.8658	29	30	990.4522	2.01	1190.0036
30	31	990.6288	4.28	1199.4564	31	32	990.8045	10.99	1209.224
32	33	990.977	0.55	1219.3064	33	34	991.1502	10.53	1229.7037
34	35	991.3219	19.35	1240.4158	35	36	991.4901	8.03	1251.4428
36	37	991.6572	-1.21	1262.7844	37	38	991.8237	-1.44	1274.4409
38	39	991.9889	-1.96	1286.412	41	42	992.4753	-8.25	1324.2136
42	43	992.6355	-2.13	1337.4434	43	44	992.7943	4.8	1350.9878
45	46	993.1063	4.55	1379.0203	46	47	993.2592	-5.78	1393.5083

Table 6.6: Observed Transitions for Al_2O, $(00^01) \leftarrow (00^00)$. Experimental errors for line positions are better then $1 \cdot 10^{-3}\,cm^{-1}$.

J'	J''	Frequency [cm^{-1}]	Obs-Calc [$10^{-4}\,cm^{-1}$]	E_{lower} [K]	J'	J''	Frequency [cm^{-1}]	Obs-Calc [$10^{-4}\,cm^{-1}$]	E_{lower} [K]
67	66	980.5931	4.01	711.0018	66	65	980.9106	-6.99	690.1094
65	64	981.2282	-0.75	669.5278	64	63	981.5444	6.04	649.2569
63	62	981.8578	-0.58	629.2967	62	61	982.17	-2.58	609.6474
60	59	982.7913	6.89	571.2814	59	58	983.0985	0.49	552.5648
58	57	983.4052	3.72	534.1592	57	56	983.7098	1.61	516.0648
56	55	984.0129	0.36	498.2814	55	54	984.314	-6.71	480.8092
54	53	984.6147	-1.74	463.6482	53	52	984.9133	-1.9	446.7984
52	51	985.2104	-2.24	430.2599	51	50	985.5062	-1.11	414.0328
49	48	986.0926	-2.88	382.5126	48	47	986.3841	1.83	367.2197
47	46	986.6727	-7.82	352.2383	45	44	987.2479	0.97	323.21
44	43	987.5324	-3.08	309.1633	43	42	987.8153	-7.23	295.4281
42	41	988.0976	-3.19	282.0047	41	40	988.3785	2.64	268.893
40	39	988.657	0.05	256.093	39	38	988.934	-1.44	243.6047
38	37	989.2096	-2.97	231.4283	37	36	989.4841	0.45	219.5637
36	35	989.7566	-0.45	208.0109	35	34	990.0276	-1.18	196.7701
34	33	990.2974	0.55	185.8412	33	32	990.5651	-2.57	175.2242
31	30	991.0974	5.72	154.9261	30	29	991.3608	5.48	145.2452
29	28	991.6222	0.64	135.8762	28	27	991.8823	-1.55	126.8194
27	26	992.142	7.2	118.0746	26	25	992.3988	2.14	109.6419
25	24	992.6543	0.38	101.5214	24	23	992.9088	2.88	93.7131
23	22	993.1616	3.9	86.2169	22	21	993.412	-3.39	79.0329
21	20	993.6621	2.46	72.1612	20	19	993.9103	3.25	65.6016
19	18	994.1562	-2.11	59.3544	18	17	994.4012	-2.31	53.4194
17	16	994.6449	0.37	47.7966	16	15	994.8864	-3.14	42.4862
15	14	995.1267	-4.0	37.4881	14	13	995.3659	0.18	32.8023
13	12	995.6032	-0.41	28.4288	12	11	995.8389	-0.31	24.3677
11	10	996.073	-0.72	20.6189	10	9	996.3058	0.87	17.1825
9	8	996.5366	-2.4	14.0585	8	7	996.7661	-3.37	11.2468
7	6	996.9945	0.21	8.7476	6	5	997.221	1.31	6.5607
5	4	997.4459	0.19	4.6862	4	3	997.6693	0.74	3.1242
3	2	997.8908	-2.74	1.8745	2	1	998.1113	-0.4	0.9372
1	0	998.3299	-1.93	0.3124	0	1	998.7625	-4.21	0.0
1	2	998.977	-0.73	0.3124	2	3	999.1891	-4.74	0.9372

Table 6.6: *continued...*

J'	J''	Frequency [cm^{-1}]	Obs-Calc [$10^{-4}\,cm^{-1}$]	E_{lower} [K]	J'	J''	Frequency [cm^{-1}]	Obs-Calc [$10^{-4}\,cm^{-1}$]	E_{lower} [K]
3	4	999.4007	0.74	1.8745	4	5	999.6101	0.8	3.1242
5	6	999.8182	3.13	4.6862	6	7	1000.0242	-0.8	6.5607
7	8	1000.229	-0.71	8.7476	8	9	1000.4327	4.01	11.2468
9	10	1000.6341	1.19	14.0585	10	11	1000.8344	2.39	17.1825
11	12	1001.0328	0.83	20.6189	12	13	1001.2294	-3.34	24.3677
13	14	1001.4249	-3.51	28.4288	14	15	1001.6191	0.06	32.8023
15	16	1001.8115	0.43	37.4881	16	17	1002.0023	0.58	42.4862
17	18	1002.1914	-0.94	47.7966	19	20	1002.5652	-1.53	59.3544
20	21	1002.7497	-1.82	65.6016	21	22	1002.9325	-3.28	72.1612
22	23	1003.1143	0.4	79.0329	23	24	1003.2946	4.03	86.2169
24	25	1003.4728	3.38	93.7131	25	26	1003.6494	1.62	101.5214
27	28	1003.9982	2.05	118.0746	28	29	1004.17	-0.42	126.8194
29	30	1004.3408	2.75	135.8762	30	31	1004.5095	1.0	145.2452
31	32	1004.6765	-2.44	154.9261	32	33	1004.8426	0.93	164.9192
33	34	1005.007	2.77	175.2242	34	35	1005.1696	2.48	185.8412
35	36	1005.3306	2.35	196.7701	36	37	1005.4899	0.27	208.0109
37	38	1005.648	1.65	219.5637	38	39	1005.8041	0.32	231.4283
39	40	1005.959	1.39	243.6047	40	41	1006.1126	5.8	256.093
41	42	1006.2636	-0.3	268.893	42	43	1006.4137	0.18	282.0047
43	44	1006.5623	2.3	295.4281	44	45	1006.709	0.81	309.1633
45	46	1006.8541	-0.93	323.21	46	47	1006.9978	-0.8	337.5683
47	48	1007.1401	0.56	352.2383	48	49	1007.2806	0.64	367.2197
49	50	1007.4195	0.85	382.5126	50	51	1007.5568	-0.38	398.117
51	52	1007.6926	-0.07	414.0328	52	53	1007.8264	-3.21	430.2599
53	54	1007.9592	-1.18	446.7984	54	55	1008.0905	2.1	463.6482
55	56	1008.22	3.34	480.8092	56	57	1008.3477	1.8	498.2814
57	58	1008.4731	-6.49	516.0648	58	59	1008.5985	1.87	534.1592
59	60	1008.7213	-0.28	552.5648	60	61	1008.8426	-1.66	571.2814
61	62	1008.9624	-2.22	590.3089	62	63	1009.0809	1.05	609.6474
63	64	1009.1974	-0.43	629.2967	64	65	1009.3126	1.53	649.2569
65	66	1009.4257	-1.36	669.5278	66	67	1009.538	3.45	690.1094
67	68	1009.6475	-3.7	711.0018	68	69	1009.7568	3.1	732.2047
69	70	1009.8635	0.79	753.7182					

Table 6.7: Observed Transitions for Al_2O, $(00^02) \leftarrow (00^01)$. Experimental errors for line positions are better then $1 \cdot 10^{-3}\,cm^{-1}$.

J'	J''	Frequency [cm^{-1}]	Obs-Calc [$10^{-4}\,cm^{-1}$]	E_{lower} [K]	J'	J''	Frequency [cm^{-1}]	Obs-Calc [$10^{-4}\,cm^{-1}$]	E_{lower} [K]
50	49	975.8873	3.3	1831.596	49	48	976.1768	-2.75	1816.1033
46	45	977.0383	-0.97	1771.4803	45	44	977.3228	4.01	1757.2246
44	43	977.6053	3.78	1743.2783	43	42	977.8854	-5.24	1729.6413
42	41	978.1655	1.36	1716.3138	41	40	978.4441	7.01	1703.2957
40	39	978.7201	2.76	1690.5872	39	38	978.9947	-0.04	1678.1882
38	37	979.2677	-4.0	1666.0987	37	36	979.5404	3.75	1654.3188
36	35	979.8106	2.67	1642.8486	35	34	980.0797	4.42	1631.688
34	33	980.3466	0.27	1620.8371	33	32	980.6126	2.7	1610.2959
32	31	980.8767	0.06	1600.0644	31	30	981.1413	18.51	1590.1428
30	29	981.4009	1.6	1580.5309	29	28	981.6607	2.44	1571.2288
28	27	981.9186	-0.82	1562.2365	27	26	982.1753	-0.75	1553.5542
26	25	982.4303	-2.45	1545.1817	25	24	982.6846	3.87	1537.1191
24	23	982.9367	2.91	1529.3664	23	22	983.1868	-2.73	1521.9237
22	21	983.4367	5.0	1514.791	21	20	983.6849	11.2	1507.9683
20	19	983.9303	4.23	1501.4555	19	18	984.1744	-0.05	1495.2528
18	17	984.4169	-5.05	1489.3601	17	16	984.6587	-2.94	1483.7775
16	15	984.8986	-4.23	1478.5049	15	14	985.1374	-0.22	1473.5424
14	13	985.3745	0.34	1468.89	13	12	985.6097	-1.52	1464.5477
12	11	985.843	-7.71	1460.5156	11	10	986.0758	-4.18	1456.7935
10	9	986.3072	1.4	1453.3816	9	8	986.5359	-5.71	1450.2798
8	7	986.7636	-6.36	1447.4882	7	6	986.9911	4.79	1445.0068
6	5	987.2151	-3.21	1442.8355	5	4	987.4386	-0.41	1440.9744
4	3	987.6605	0.78	1439.4235	3	2	987.8804	-1.96	1438.1827
2	1	988.099	-3.01	1437.2521	1	2	988.9595	6.39	1436.6318
2	3	989.1697	-2.79	1437.2521	3	4	989.3797	2.27	1438.1827
4	5	989.5875	0.1	1439.4235	5	6	989.7939	-0.48	1440.9744
6	7	989.999	1.22	1442.8355	7	8	990.202	-3.5	1445.0068
8	9	990.4045	2.52	1447.4882	9	10	990.6047	1.16	1450.2798
10	11	990.803	-4.47	1453.3816	11	12	991.0014	7.45	1456.7935
12	13	991.1973	8.15	1460.5156	13	14	991.3911	4.16	1464.5477
14	15	991.584	6.7	1468.89	15	16	991.7748	2.91	1473.5424
16	17	991.9643	1.62	1478.5049	17	18	992.1527	5.42	1483.7775
18	19	992.3387	-0.48	1489.3601	19	20	992.5238	0.61	1495.2528

Table 6.7: *continued...*

J'	J''	Frequency [cm^{-1}]	Obs-Calc [$10^{-4}\,cm^{-1}$]	E_{lower} [K]	J'	J''	Frequency [cm^{-1}]	Obs-Calc [$10^{-4}\,cm^{-1}$]	E_{lower} [K]
20	21	992.7066	-5.24	1501.4555	21	22	992.8893	2.27	1507.9683
22	23	993.07	5.59	1514.791	23	24	993.2479	-3.77	1521.9237
24	25	993.425	-5.17	1529.3664	25	26	993.6014	1.58	1537.1191
26	27	993.7756	1.7	1545.1817	27	28	993.948	-0.84	1553.5542
28	29	994.1187	-4.09	1562.2365	29	30	994.288	-6.29	1571.2288
30	31	994.4563	-3.33	1580.5309	31	32	994.6228	-2.55	1590.1428
32	33	994.7878	-1.44	1600.0644	33	34	994.9509	-3.67	1610.2959
34	35	995.1123	-7.32	1620.8371	35	36	995.2732	0.07	1631.688
36	37	995.4319	0.46	1642.8486	37	38	995.5891	0.96	1654.3188
38	39	995.7441	-4.13	1666.0987	39	40	995.8985	0.3	1678.1882
40	41	996.0507	-1.29	1690.5872	41	42	996.2018	1.76	1703.2957
42	43	996.3511	2.05	1716.3138	43	44	996.4983	-3.14	1729.6413
46	47	996.932	-3.32	1771.4803					

References

[1] Sedlmayr, E.; Dominik, C. Dust driven winds. *Space Science Reviews* **1995**, *73*, 211–272.

[2] Gail, H.-P.; Sedlmayr, E. Inorganic dust formation in astrophysical environments. *Faraday Discuss.* **1998**, *109*, 303–319.

[3] Sharp, C. M.; Huebner, W. F. Molecular equilibrium with condensation. *Astrophysical Journal Supplement Series* **1990**, *72*, 417–431.

[4] Lattimer, J. M.; Schramm, D. N.; Grossman, L. Condensation in supernova ejecta and isotopic anomalies in meteorites. *Astrophysical Journal* **1978**, *219*, 230.

[5] Kamiński, T.,; Müller, H. S. P.,; Schmidt, M. R.,; Cherchneff, I.,; Wong, K. T.,; Brünken, S.,; Menten, K. M.,; Winters, J. M.,; Gottlieb, C. A.,; Patel, N. A., An observational study of dust nucleation in Mira (oi) - II. Titanium oxides are negligible for nucleation at high temperatures. *A&A* **2017**, *599*, A59.

[6] Decin, L.,; Richards, A. M. S.,; Danilovich, T.,; Homan, W.,; Nuth, J. A., ALMA spectral line and imaging survey of a low and a high mass-loss rate AGB star between 335 and 362 GHz. *A&A* **2018**, *615*, A28.

[7] Kamiński, T.,; Gottlieb, C. A.,; Menten, K. M.,; Patel, N. A.,; Young, K. H.,; Brünken, S.,; Müller, H. S. P.,; McCarthy, M. C.,; Winters, J. M.,; Decin, L., Pure rotational spectra of TiO and TiO_2 in VY Canis Majoris. *A&A* **2013**, *551*, A113.

[8] Gail, H.-P.; Sedmayr, E. The primary condensation process for dust around late M-type stars. *A&A* **1986**, *166*, 225–236.

[9] Lodders, K. Solar System Abundances and Condensation Temperatures of the Elements. *The Astrophysical Journal* **2003**, *591*, 1220–1247.

[10] Grossman, L. Condensation in the primitive solar nebula. *Geochimica et Cosmochimica Acta* **1972**, *36*, 597 – 619.

[11] Tenenbaum, E. D.; Ziurys, L. M. Millimeter detection of AlO ($X^2\Sigma^+$): Metal oxide chemistry in the envelope of VY Canis Majoris. *ApJ* **2009**, *694*, L59.

[12] Tsuji, T. Molecular abundances in stellar atmospheres. II. *A&A* **1973**, *23*, 411–431.

[13] Richter, M. J.; DeWitt, C. N.; McKelvey, M.; Montiel, E.; McMurray, R.; Case, M. E. EXES: The Echelon-cross-echelle Spectrograph for SOFIA. *Journal of Astronomical Instrumentation* **2018**, *07*, 1840013.

[14] Lacy, J. H.; Richter, M. J.; Greathouse, T. K.; Jaffe, D. T.; Zhu, Q. TEXES: A Sensitive High-Resolution Grating Spectrograph for the Mid-Infrared. *Publications of the Astronomical Society of the Pacific* **2002**, *114*, 153–168.

[15] Büchler, A.; Stauffer, J. L.; Klemperer, W.; Wharton, L. Determination of the Geometry of Lithium Oxide, $Li_2O(g)$, by Electric Deflection. *The Journal of Chemical Physics* **1963**, *39*, 2299–2303.

[16] Linevsky, M. J.; White, D.; Mann, D. E. Infrared Spectrum and Structure of Gaseous Al_2O. *The Journal of Chemical Physics* **1964**, *41*, 542–545.

[17] Makowiecki, D. M.; Lynch, D. A.; Carlson, K. D. Infrared spectra of the aluminum family suboxides. *The Journal of Physical Chemistry* **1971**, *75*, 1963–1969.

[18] Douglas, M. A.; Hauge, R. H.; Margrave, J. L. Electronic absorption and emission studies of the Group IIIA metal suboxides isolated in cryogenic rare gas matrices. *High Temperature Science* **1983**, *16*, 35–54.

[19] Marino, C. P.; White, D. Infrared spectra of the aluminum family suboxides. Comments. *The Journal of Physical Chemistry* **1973**, *77*, 2929.

[20] Masip, J.; Clotet, A.; Ricart, J. M.; Illas, F.; Rubio, J. Molecular structure and vibrational frequencies of Al_xO_y ($x = 1, 2; y \leq 3$) derived from ab initio calculations. *Chemical Physics Letters* **1988**, *144*, 373 – 377.

[21] Leszczynski, J.; Kwiatkowski, J. S. Molecular structures of metal suboxides M_2O (M = boron, aluminum, gallium): bent or linear? *The Journal of Physical Chemistry* **1992**, *96*, 4148–4151.

[22] Bencivenni, L.; Pelino, M.; Ramondo, F. Ab initio study on the Al_2O, Al_2O_2, Si_2O_2 and $AlSiO_2$ oxides and on the $LiAlO_2$ and $NaAlO_2$ molecules. *Journal of Molecular Structure: THEOCHEM* **1992**, *253*, 109 – 120.

[23] Cai, M.; Carter, C. C.; Miller, T. A.; Bondybey, V. E. Fluorescence excitation and resolved emission spectra of supersonically cooled Al_2O. *The Journal of Chemical Physics* **1991**, *95*, 73–79.

[24] Andrews, L.; Burkholder, T. R.; Yustein, J. T. Reactions of Pulsed-Laser Evaporated Aluminum Atoms with Oxygen. Infrared Spectra of the Reaction Products in Solid Argon. *The Journal of Physical Chemistry* **1992**, *96*, 10182–10189.

[25] Deutsch, H.; Hilpert, K.; Becker, K.; Probst, M.; Märk, T. D. Calculated absolute electron-impact ionization cross sections for AlO, Al_2O, and WO_x (x=1–3). *Journal of Applied Physics* **2001**, *89*, 1915–1921.

[26] Koput, J.; Gertych, A. Ab initio prediction of the potential energy surface and vibrational-rotational energy levels of dialuminum monoxide, Al_2O. *The Journal of Chemical Physics* **2004**, *121*, 130–135.

[27] Turney, J. M.; Sari, L.; Yamaguchi, Y.; Schaefer, H. F. The singlet electronic ground state isomers of dialuminum monoxide: AlOAl, AlAlO, and the transition state connecting them. *The Journal of Chemical Physics* **2005**, *122*, 094304.

[28] Bernath, P. F. *Spectra of Atoms and Molecules*, 2nd ed.; Oxford University Press, 2005.

[29] Haken, H.; Wolf, H. C. *Molekülphysik und Quantenchemie*, 5th ed.; Springer, 2006.

[30] Demtröder, W. *Experimentalphysik 3*, 4th ed.; Springer, 2010.

[31] Demtröder, W. *Molekülphysik*, 2nd ed.; Oldenbourg Verlag München, 2013.

[32] Grody, W.; Cook, R. L. *Microwave Molecular Spectra*; John Wiley & Sons, 1984.

[33] Yamada, K. M. T.; Birss, F. W.; Aliev, M. R. Effective Hamiltonian for polyatomic linear molecules. *Journal of Molecular Spectroscopy* **1985**, *112*, 347 – 356.

[34] Niedenhoff, M.; Yamada, K. M. T. Systematic Calculation of Vibration-Rotation Energy Levels of a Linear Molecule with Two Bending Modes. *Journal of Molecular Spectroscopy* **1993**, *157*, 182 – 197.

[35] Giesen, T. F.; Mookerjea, B.; Fuchs, G. W.; Breier, A. A.; Witsch, D.; Simon, R.; Stutzki, J. First detection of the carbon chain molecules ^{13}CCC and C^{13}CC towards SgrB_2(M). 2019.

[36] Luther, V. Infrarot-Laserspektroskopie an Silizium- und Germanium-Kohlenstoffverbindungen. Ph.D. thesis, 2015.

[37] Amoruso, S. Modeling of UV pulsed-laser ablation of metallic targets. *Applied Physics A* **1999**, *69*, 323–332.

[38] Lu, Y.; Zhou, Y.-z.; Chen, X.-m.; Li, Z.-y.; Yu, Q.-c.; Liu, D.-c.; Yang, B.; Xu, B.-q. Thermodynamic analysis and dynamics simulation on reaction of Al_2O and $AlCl_2$ with carbon under vacuum. *Journal of Central South University* **2016**, *23*, 286–292.

[39] Scoles, G. *Atomic and Molecular Beam Methods*; Oxford University Press, 1988.

[40] Witsch, D.; Lutter, V.; Breier, A. A.; Yamada, K. M. T.; Fuchs, G. W.; Gauss, J.; Giesen, T. F. Infrared Spectroscopy of Disilicon-Carbide, Si_2C: The $\nu 3$ Fundamental Band. *The Journal of Physical Chemistry A* **2019**, *123*, 4168–4177.

[41] Sirtori, C.; Capasso, F.; Faist, J.; Hutchinson, A. L.; Sivco, D. L.; Cho, A. Y. Resonant tunneling in quantum cascade lasers. *IEEE Journal of Quantum Electronics* **1998**, *34*, 1722–1729.

[42] Faist, J. *Quantum Cascade Laser*; Oxford University Press, 2013.

[43] Witsch, D.; Breier, A. A.; Fuchs, G. W.; Giesen, T. F. Infrared Frequency Alternating Sweep Technique (IR-FAST) for Spectroscopic Investigations of Laser-Ablated Transient Molecules. *In Preparation* **2019**,

[44] Oller-Moreno, S.; Pardo, A.; Jiménez-Soto, J. M.; Samitier, J.; Marco, S. Adaptive Asymmetric Least Squares baseline estimation for analytical instruments. 2014 IEEE 11th International Multi-Conference on Systems, Signals Devices (SSD14). 2014; pp 1–5.

[45] Western, C. M. PGOPHER: A program for simulating rotational, vibrational and electronic spectra. *Journal of Quantitative Spectroscopy and Radiative Transfer* **2017**, *186*, 221 – 242, Satellite Remote Sensing and Spectroscopy: Joint ACE-Odin Meeting, October 2015.

[46] Krieg, J.; Lutter, V.; Endres, C. P.; Keppeler, I. H.; Jensen, P.; Harding, M. E.; Vázquez, J.; Schlemmer, S.; Giesen, T. F.; Thorwirth, S. High-Resolution Spectroscopy of C_3 around 3 μm. *The Journal of Physical Chemistry A* **2013**, *117*, 3332–3339, PMID: 23477539.

[47] Barners, M.; Fraser, M. M.; Hajigeorgiou, P. G.; Merer, A. J. Isotope and Hyperfine Structure in the 'Orange' System of FeO: Evidence for Two 5Δi Excited States. *Journal of Molecular Spectroscopy* **1995**, *170*, 449 – 465.

[48] France, W. L.; Dickey, F. P. Fine Structure of the 2.7 Micron Carbon Dioxide Rotation-Vibration Band. *The Journal of Chemical Physics* **1955**, *23*, 471–474.

[49] Gausset, L.; Herzberg, G.; Lagerqvist, A.; Rosen, B. Analysis of the 4050-Å Group of the C_3 Molecule. *Astrophysical Journal* **1965**, *142*, 45.

[50] Rohlfing, E. A.; Goldsmith, J. E. M. Stimulated emission pumping spectroscopy of jet-cooled C_3. *The Journal of Chemical Physics* **1989**, *90*, 6804–6805.

[51] Breier, A. A.; Büchling, T.; Schnierer, R.; Lutter, V.; Fuchs, G. W.; Yamada, K. M. T.; Mookerjea, B.; Stutzki, J.; Giesen, T. F. Lowest bending mode of ^{13}C-substituted C_3 and an experimentally derived structure. *The Journal of Chemical Physics* **2016**, *145*, 234302.

[52] Tashkun, S. A.; Perevalov, V. I.; Teffo, J. L.; Rothman, L. S.; Tyuterev, V. G. Global Fitting of $^{12}C^{16}O_2$ vibrational-rotational line positions using the effective Hamiltonian approach. *Journal of Quantitative Spectroscopy and Radiative Transfer* **1998**, *60*, 785 – 801.

[53] Schröder, B.; Doney, K. D.; Sebald, P.; Zhao, D.; Linnartz, H. Stretching our understanding of C_3: Experimental and theoretical spectroscopy of highly excited $n\nu_1 + m\nu_3$ states (n $\leq$7 and m $\leq$ 3). *The Journal of Chemical Physics* **2018**, *149*, 014302.

Acknowledgment

At this point I would like to thank those without whose help and support this work would not have been possible.

First I would like to thank Prof. Dr. Thomas Giesen for the opportunity to write my master thesis in the Laboratory Astrophysics Group of the University of Kassel and for his expert advice. Also, I would like to thank Prof. Dr. Arno Ehresmann, who has made himself available as second referee of this master thesis.

Furthermore I would like to thank Daniel Witsch for introducing me to the topic and explaining the experiment to me. In addition to Daniel Witsch, I would also like to thank Thomas Büchling, Dr. Guido Fuchs and Dr. Alexander Breier who stood by my side with advice and support when I had questions.

Of course I would also like to thank all other group members of the Laboratory Astrophysics Group for the nice conversations and the great working atmosphere.

Finally, I would like to thank my loved ones, who have supported me throughout the entire process.

Declaration of Own Work

I hereby confirm that I have written this master thesis independently and have not used any tools other than those indicated. The parts of the work taken from the wording or the meaning of other works have been marked with the source.

_____ _____

Date, Place Signature